Fjóla Ösp Snævarsdóttir

CMOS Image Sensor Design Methodology

Applied to Optical Tomography and Neural Networks

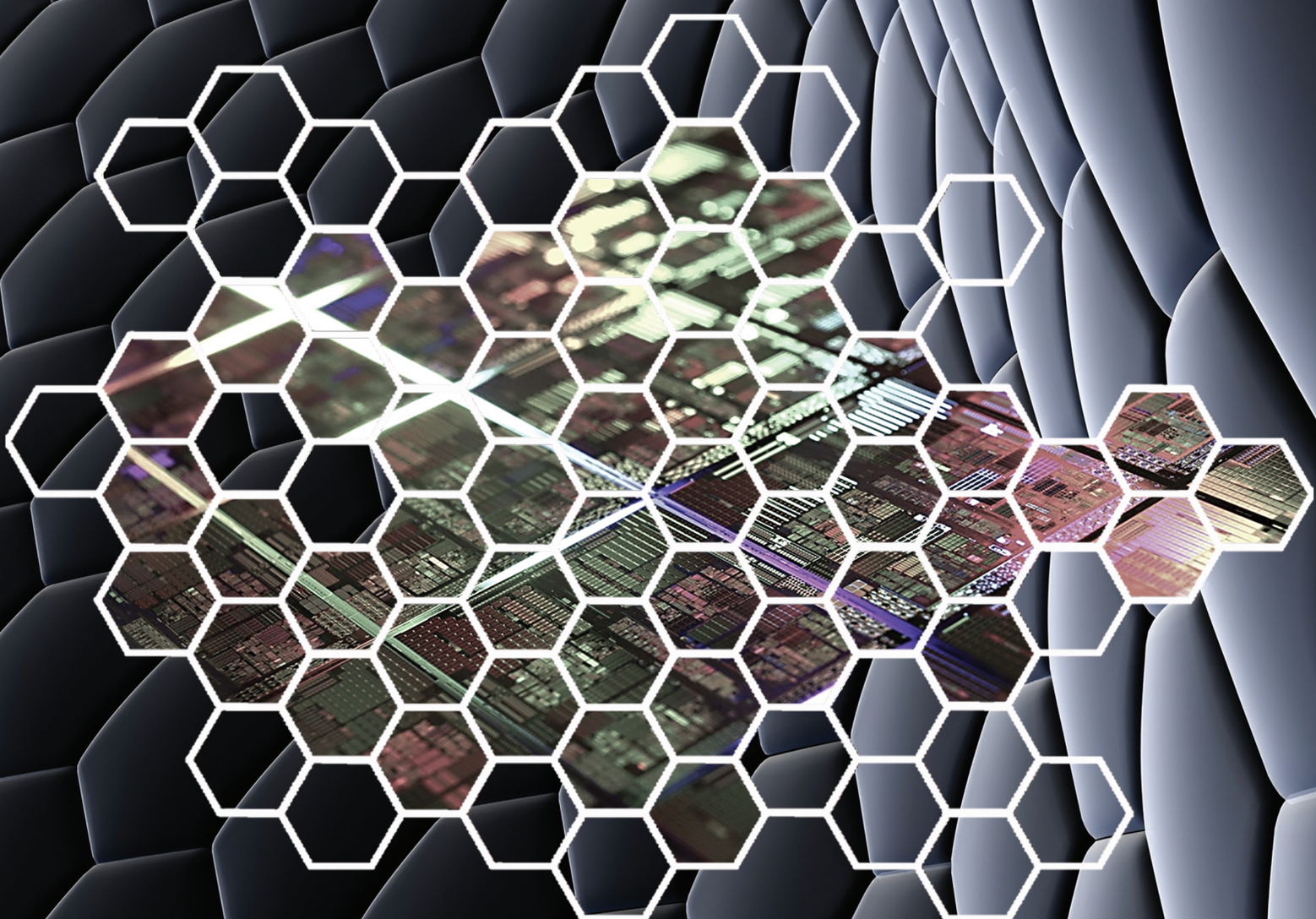

TU Delft

CMOS Image Sensor Design Methodology Applied to Optical Tomography and Neural Networks

Delft University of Technology
Faculty of Electrical Engineering, Mathematics and Computer Science
Fjóla Ösp Snævarsdóttir

CMOS Image Sensor Design Methodology Applied to Optical Tomography and Neural Networks

by

Fjóla Ösp Snævarsdóttir

in partial fulfillment of the requirements for the degree of

MASTER OF SCIENCE

in

ELECTRICAL ENGINEERING

at the Delft University of Technology
to be defended publicly on January 29th, 2018.

Supervisors:	Prof. dr. A.J.P. Theuwissen	
	Dr. B. Luyssaert	
Thesis committee:	Prof. dr. A.J.P. Theuwissen	TU Delft
	Prof. dr. R. Dekker	TU Delft
	Dr. B. Luyssaert	Caeleste

TU Delft Delft University of Technology

Electronic Instrumentation Laboratory

DELFT UNIVERSITY OF TECHNOLOGY
DEPARTMENT OF MICROELECTRONICS & COMPUTER ENGINEERING

The undersigned hereby certify that they have read and recommend to the Faculty of Electrical Engineering, Mathematics and Computer Science for acceptance a thesis entitled **"CMOS Image Sensor Design Methodology Applied to Optical Tomography and Neural Networks"** by **Fjóla Ösp Snævarsdóttir** in partial fulfillment of the requirements for the degree of **Master of Science**.

Approved:

Prof. dr. Albert Theuwissen
Full Professor

Dr. Bert Luyssaert
Committee Member

Prof. dr. Ronald Dekker
Committee Member

TU Delft Delft University of Technology

Electronic Instrumentation Laboratory

This project was performed in co-operation with Caeleste CVBA, Belgium. Their support and assistance is hereby gratefully acknowledged.

To my beloved parents, myself and you

Abstract

Imaging sensors are remarkable devices which are able to capture moments and present them in a form available to us for years to come. With the use of material properties and photon particles, charges can be produced which, in combination with electric circuitry, transform into information understandable to the human eye and eventually the brain. When a photon particle hits a silicon photodiode, an electron-hole pair forms. By using readout techniques optimized for noise, area and power, images of different quality can be read out. Imaging concepts such as Signal-to-Noise Ratio (SNR), Dynamic Range (DR), Resolution, Contrast and more can be used to describe the quality of the sensor. These concepts of quality are of interest when designing an imaging sensor. Throughout this thesis, design methodologies are applied to both the field of Optical Tomography and Neural Networks.

Optical Tomography is an imaging technique capable of detecting the internal structure of a subject with the use of image sensors. Various Optical Tomography techniques exist such as Diffusion Optical Tomography, Optical Projection Tomography and Optical Coherence Tomography (OCT). Optical Coherence Tomography is of special interest due to published papers which show the potential of the use with CMOS image sensors. The technique is based on the Michelson interferometer which is used in order to retrieve data of micrometer resolution. A feasibility study was conducted on OCT which shows potential for future research due to its recent development using CMOS image sensors. A review of state-of-the-art solutions is presented. With the most recent publication on a CMOS image sensor in OCT, with a dynamic range of 66 dB and a frame rate of 730 frames per second (fps), showed the possibility of retrieving OCT images of higher quality compared to conventional sensors.

Artificial Neural Networks are inspired by the complex structure of our brain. By using its unique way of parallel computation, algorithms are capable of teaching our electronic devices human capabilities such as speech and face recognition. Artificial Neural Networks are identified by neurons and synapses in analogy to the nervous system. In this thesis, pixel design concepts are applied to neural networks where the pixel structure is modelled as a neuron. As a part of a larger project, low power design cells are collected into a combined library and presented. The library, in the end of development, will be used for finalizing and optimizing the complete neural network. One of the project's challenges was to design a novel absolute value filter. The filter's importance is presented as a part of a learning algorithm where it takes an absolute value of the difference between two signals. The resulting filter is operational and has the low power dissipation of 87 nW. The area was minimized and includes 10 transistors and a current mirror. The signal gain is around -13.2 dB which shows attenuation of the signal. The amount of gain required for this structure, as part of the learning algorithm, is not yet determined. Future work includes improving the circuit's gain with a gain boost technique and minimizing noise levels with the use of larger transistors and new technologies.

Keywords: Imaging Sensors, Optical Tomography Principles, Optical Coherence Tomography, Neural Networks, Learning Algorithms, Absolute Value Filter

Preface

"The Analog Art shows no signs of yielding to the Dodo's fate.
The emergence and maturation of monolithic processing finesse
has perhaps lagged a bit behind the growth of the Binary Business.
But whereas digital precision is forever bounded by bits,
there is no limit excepting Universal Hiss to the ultimate
accuracy and functional variety of simple analog circuits"

-Barrie Gilbert, January, 1973

Signal accuracy is of great importance to the ultimate precision. Gilbert's contribution to the field of analog circuitry is admirable. His pioneering work with the Gilbert cell as well as the famous translinear principle has contributed highly to the field. In this thesis, design methodologies for analog circuitry are applied to applications where the accuracy of the circuit is vital for accurate operation.

I would like to express my gratitude to the MSc program in Microelectronics at the department of Electrical Engineering. After one year at TU Delft in Delft, the Netherlands and one year at Caeleste in Mechelen, Belgium, the time has been very challenging, exciting and helped me to grow as a person. I wish all the best to everyone who has participated in my journey and towards the completion of this thesis.

Fjóla Ösp Snævarsdóttir
Reykjavík, 2017

Contents

List of Figures

Glossary

ADC Analog-to-Digital Converter.

CCD Charge Coupled Devices.

CDS Correlated Double Sampling.

CMOS Complimentary Metal Oxide Semiconductor.

DOT Diffuse Optical Tomography.

DR Dynamic Range.

FF Fill Factor.

FF-OCT Full-Field OCT.

FT Fluorescence Tomography.

FWC Full Well Capacity.

IC Intergrated Circuit.

MTF Modulation Transfer Function.

NIR Near-Infrared.

OCT Optical Coherence Tomography.

OPT Optical Projection Tomography.

PPD Pinned Photodiode.

QE Quantum Efficiency.

SD-OCT Spectral-Domain OCT.

SLD Super Luminescent Diode.

SNR Signal-to-Noise Ratio.

SSD-OCT Swept Source-Domain OCT.

TD-OCT Time-Domain OCT .

System of Units

Quantity	**Symbol**	**SI Unit**	**SI Base Units**	**Constant**
Boltzmann Constant	k_B			$1.38 \cdot 10^{-23}\ J \cdot K^{-1}$
Capacitance	C	Farad, F	$A \cdot s \cdot V^{-1}$	
Electric Charge	q	Coulomb, C	$A \cdot s$	$1.6 \cdot 10^{-19}$ C
Frequency	f	Hertz, Hz	s^{-1}	
Permittivitity of Free Space	ϵ_o			$8.85 \cdot 10^{-14}\ F \cdot cm^{-1}$
Planck Constant	$\hbar$			$4.136 \cdot 10^{-15}\ eV \cdot s$
Resistance	R	Ohm, Ω	$kg \cdot m^2 \cdot s^{-3} \cdot A^{-2}$	
Si Bandgap Energy	E_g			$1.12\ eV$
Speed of Light	c			$2.99 \cdot 10^8\ m \cdot s^{-1}$
Voltage	U	Volt, V	$kg \cdot m^2 \cdot s^{-3} \cdot A^{-1}$	
Wavelength	λ	Meter, m	m	

1 Introduction

Image sensors are widely used in our modern world. Our expectations towards their development and qualities are increasing as the size of the transistor scales down to keep up with Moore's law. The famous law describes the continuous increase in the number of transistors on a dense Integrated Circuit (IC) over time. IC designers are constantly challenged by supplying sensors which are more power efficient, have less noise, are smaller and faster. In order to keep up with the evolution of circuit design there are a lot of challenges. With the constant development, new architectures with certain functions are improved and made optimal for the application of interest. Other developments, such as in the area of fabrication, include new techniques which allow for smaller or more accurate transistors. The main goal for designers is to find the perfect balance between power/area/speed which is optimized for the application of interest.

When working in the field of image sensors one can not go about without mentioning Charge Coupled Device (CCD) Image sensors. Until recently CCD sensors dominated the imaging world due to their quality of images. However, with the development in lithography in the 1990s, designers were finally able to design Complementary Metal Oxide Semiconductor (CMOS) devices in such a way that quality images could be retrieved. Today CMOS image sensors have caught up to CCD sensors and have some advantages over CCD such as higher frame rate, higher resolution, lower cost and more power efficiency [1]. With CMOS sensors, designers have the freedom of adding processing circuitry inside the pixel which vastly increases the design space.

Optical Tomography is a technique which uses light in the optical region (visible to Near-Infrared (NIR) wavelengths) to acquire an image. Optical Tomography has the possibility of enabling non-invasive imaging of internal structures. Tomographic techniques use reconstruction algorithms to build up an image from output signals. Tomographic systems consists of a light source, a subject and a detector. Reconstruction algorithms are able to determine an internal structure of a subject by calculating the change of the light source to the light that returns to the detector. From this behavior the internal structure can be estimated. When using high energy particles as a source, such as X-ray waves, the internal region can simply be reconstructed from the absorption function of the matter it travelled through. However, when it comes to using a light source in the optical region, other functional behaviors of the tissue of the subject has to be taken into account. The reconstruction algorithm has to include the light/tissue interactions such as absorption, scattering and reflection which makes Optical Tomography a challenging imaging technique. Nevertheless, high quality image sensors are capable of providing sufficient data to view the internal data with micrometer resolution.

Another topic in this thesis concerns neural networks. Neural networks are a hot topic today and have been proven useful in an increasing number of applications. The idea behind artificial neural networks is to construct a network which is able to learn in a similar manner as our brain

does. Instead of using serial calculations of computers, parallel networks are now of interest. Advancements in GPUs has enabled faster training of neural networks but at the cost of power consumption. For less power hungry solutions hardware development is applied. When hardware is able to correct itself, it becomes highly advantageous when it comes to receiving higher speed, more accuracy and more power efficiency in networks.

The overall aim of this thesis is to apply image sensor design methodologies to the two emerging fields: Optical Tomography and Neural Networks. For Optical Tomography, the goal is to show the feasibility of CMOS image sensors in tomographic applications. With an overview of the topic the thesis approaches the problem from a high level towards specific application and publications where CMOS sensors have shown potential. There the current status of CMOS image sensors in Optical Coherence Tomography is discussed. For the field of hardware neural networks, the goal is to design a novel absolute value filter, which can be used both for a learning algorithm or signal filtering. The filter developed is a part of a larger neural network. Alongside this, components which play a part in the design and network are explained and discussed. A cell library, a collection of circuits, is used to form a neural network which then will be optimized. Due to these two unrelated subjects the thesis is split up into two different parts.

1.1 Thesis Organization

The first part presents a feasibility study on Optical Tomography. It starts by explaining the field and theory. Further it goes into specialized techniques and properties. A branch called Optical Coherence Tomography is presented and prospective relevant papers showing the potential of CMOS image sensors are discussed in a literature review. The main limiting factors are put forward and feasibility is predicted. The aim is to bring forward the current status of CMOS imaging sensors in Optical Coherence Tomography from a wide field of Tomography by creating a single point of reference for further research and development.

The second part presents an absolute value filter which is a part of a learning algorithm used to train hardware neural networks. Overall it presents background knowledge to neural networks, learning algorithms and performance as well as a developed neural network which is a part of a larger project which is in continuous development. Neural networks are made up from both synapses and neurons, whereas in this thesis the focus is only on the structure of a single neuron. The components which make up the neuron, also known as the pixel, are explained and its challenges are listed. As the application requires low power and minimal area, the hardware structure is developed in the analog domain. Even though analog implementation is highly complex, it offers a higher performance concerning power consumption and area. Finally, the performance of the developed absolute value filter is evaluated.

2 Imaging Sensors

This chapter discusses the fundamentals of image sensors in general and provides the prerequisite knowledge for the topics mentioned throughout the thesis. The first section lists the main concepts of the image sensors among their important architecture parts such as the photodiode, pixel structures and readout circuitry. The second section discusses important design properties and effects of the image sensors. However, this chapter will only briefly grasp the topic of image sensing.

2.1 Image Sensor Fundamentals

Image sensor architectures are well known as either Charge Coupled Devices (CCDs) or Complimentary Metal Oxide Semiconductors (CMOS). In the 1960s, S.R. Morrison developed the first image sensor made with semiconductor technology [2]. In the early age of image sensor development, CCDs offered better performance than CMOS sensors mostly due to the fabrication technology available at the time. Scientists were still drawn into CMOS image sensor possibilities but it was not until the 1990s when lithography had further advancements such that the development of CMOS image sensors could continue. Today, CMOS sensors are considered to be more advantageous concerning flexibility, energy consumption, frame rate and cost than CCD sensors. In this thesis CMOS image sensors are of topic. A vital component of an image sensor is the photodiode, the light sensitive area of the pixel. An image sensor chip generally consists of a pixel array and readout components such as sense amplifiers, Analog-to-Digital Converters (ADCs), logic and peripherals. In Figure 2.1 an overview of a 16 pixels image sensor can be seen. Pixels make up the largest part of the sensor and the pixel area is defined by the total amount of pixels on the sensor.

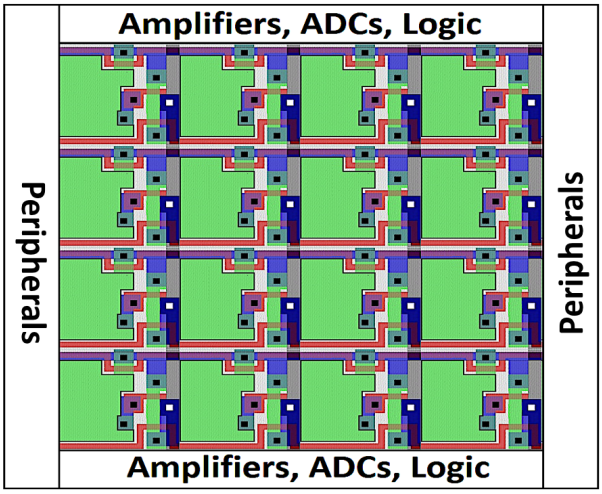

Figure 2.1: CMOS Image Sensor Layout [3]

Pixels have certain descriptive metrics such as Fill Factor (FF) and Full Well Capacity (FWC). The FF describes how much area inside a pixel is sensitive to light. In simple terms, the FF can be presented as the ratio of the area of the photodiode (A_{pd}) and the total pixel area (A_{pix}), see Equation 2.1:

$$FF = \frac{A_{pd}}{A_{pix}} \cdot 100[\%] \tag{2.1}$$

However, there are other factors which can affect the FF. For example, when photons fall next to a photodiode they can still be detected due to the electron diffusion from a non-depleted area. Present day image sensors are equipped with microlenses which play a big role in improving the FF inside pixels by condensing the light onto the photodiode [4]. The FWC defines the number of charges (N_{sat}) the pixel is able to contain before the pixel is saturated. The maximum number of charges is given by Equation 2.2:

$$N_{sat} = \frac{1}{q} \int_{V_{max}}^{V_{reset}} C_{PD}(V) \cdot dV \tag{2.2}$$

where C_{PD} is the photodiode capacitance in Farad (F) and q is the charge of an electron, $1.16 \cdot 10^{-19}$, in Coulomb (C). The limits of the integral, the initial voltage (V_{reset}) and the maximum voltage (V_{max}), depend on the depletion voltage [4].

2.1.1 Photodiode

The photodiode is the light sensitive area inside the pixel which converts photons into electrical signals. A photodiode reacts upon photon particles when the photon energy is greater than the bandgap energy, E_g, which for silicon is 1.12 eV at room temperature. The bandgap energy is the energy difference a particle needs to move from the valence band to the conduction band. This means that photons with energy greater than 1.12 eV, or wavelengths under 1100 nm, are able to force electrons into the conduction band [5]. The photon energy can be presented as, see Equation 2.3:

$$E = \hbar v = \frac{\hbar c}{\lambda} \geq E_g \tag{2.3}$$

where $\hbar$ is the Planck constant, which is approximately $4.136 \cdot 10^{-15}$ $eV \cdot s$, v is the photon frequency in Hertz ($1/s$), c is the speed of light of $2.99 \cdot 10^8$ m/s and λ is the wavelength in m. The silicon photodiode structure can be described as a junction of p-type and n-type doped semiconductor materials (p-n junction). The remarkable discovery of the p-n junction can be traced back to the 1940s to the work of J.N. Shive at Bell Telephone Laboratories. His work on the developments of phototransistors opened the doors for future generations. In continuation of this development Weckler introduced the p-n junction in the 1960s. He showed that when the junction was reversed biased, the photocurrent I_{ph}, flowing into the floating node, caused the voltage of the photodiode to discharge in relation to its capacitance [6]. This behavior can be noted in Equation 2.4:

$$\frac{dV}{dt} = \frac{I_{ph}}{C(V)} \tag{2.4}$$

where C(V) is the capacitance as a function of voltage. Inside the p-n junction, a silicon semiconductor doped with n-type impurities contributes to an excessive number of electrons (valence electrons) which increases its conductivity. On the other hand, p-type impurities

create deficiencies of valence electrons, which are called holes. Common doping impurities are Phosphorous for the n-type and Boron for the p-type. A *depletion region* forms along both sides of the metallurgical junction (the interface between the n-doped and p-doped regions in the junction) when all the charge carriers, locally, have combined with each others valence carriers and an electric field is established. The size of the depletion region depends on the doping level of the p-n junction and the reverse bias, which sets the operating region of the photodiode. Figure 2.2 shows a reversed biased photodiode (p-n junction) where p-type impurities ($p+$) have been diffused into an n-type silicon bulk (*n-type substrate*) as the active area and n-type impurities ($n+$) in the back to establish an ohmic connection [5].

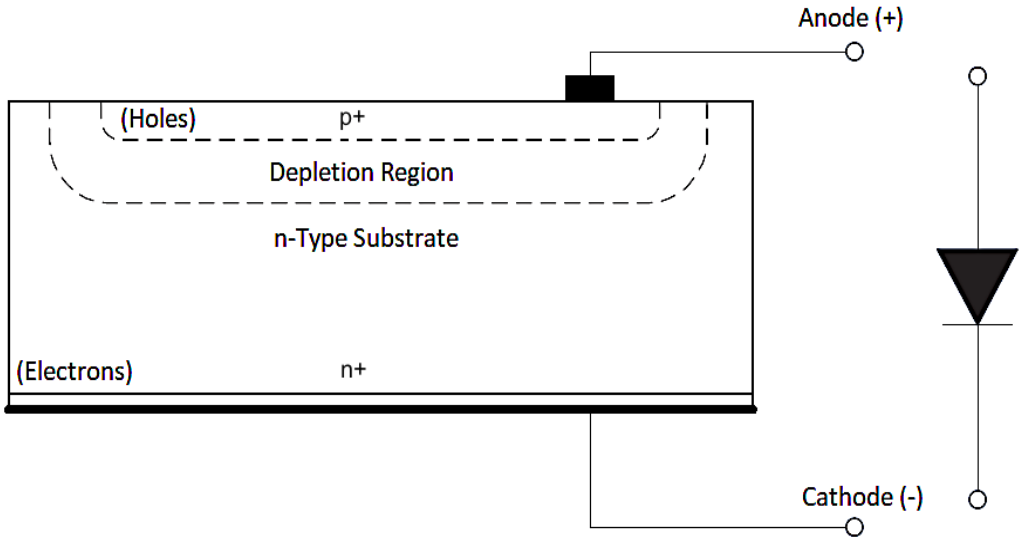

Figure 2.2: Cross-Sectional View of the Reversed Biased p-n Junction [5]

When photons fall onto the silicon, they have enough energy to break bonds in the silicon crystal. This causes a electron as well as a hole to move freely. This can be referred to as generation of an electron-hole pair. The pairs generated are swept away by drift in the depletion region and collected by diffusion from the undepleted region. The free movement of the pair generates the current [5]. The current which forms is proportional to the incident light and is called the photocurrent.

Quantum Efficiency (QE) is a descriptive factor of the performance of a photodiode. QE describes the amount of photons that can be changed into electron-hole pairs and can be collected to contribute to the output signal [7]. The depth of the formation of the electron-hole pair depends on the energy of the photon, the lesser energy the deeper the pair forms in the depletion layer. In order to estimate the overall QE, Equation 2.5 can be used:

$$QE(\lambda) = \frac{N_{sig}(\lambda)}{N_{photon}(\lambda)} \tag{2.5}$$

where N_{sig} is the signal charge produced per pixel, see Equation 2.6:

$$N_{sig} = \frac{I_{ph} \cdot A_{pix} \cdot t_{int}}{q} \tag{2.6}$$

where A_{pix} is the pixel size and t_{int} is the integration time. Therefore, in order to maximize a

signal one or more of these factors can be optimized. The number of photons per pixel, N_{photon}, can be represented as, see Equation 2.7:

$$N_{photon} = \frac{P \cdot A_{pix} \cdot t_{int}}{\hbar v} \tag{2.7}$$

where P is the input optical power and $\hbar v$ is the photon energy. In relation to Equation 2.5, the transmittance of light ($T(\lambda)$), the fill factor (FF) and the charge collection efficiency ($\eta(\lambda)$) all affect the quantum efficiency and can also be represented with Equation 2.8 [4]:

$$QE(\lambda) = T(\lambda) \cdot FF \cdot \eta(\lambda) \tag{2.8}$$

In order to retrieve desired behavior from a photodiode, a voltage bias has to be applied to the metal contacts at the ends of both the p and n layer. In order for the diode to start conducting, the voltage drop across the diode has to be larger than the threshold voltage and this is possible when an additional energy source is added to overcome the potential barrier. A photodiode has a non-linear behavior and can be described by non-linear current-voltage (I-V) characteristics, see Figure 2.3, where P_0 - P_2 represents different light levels.

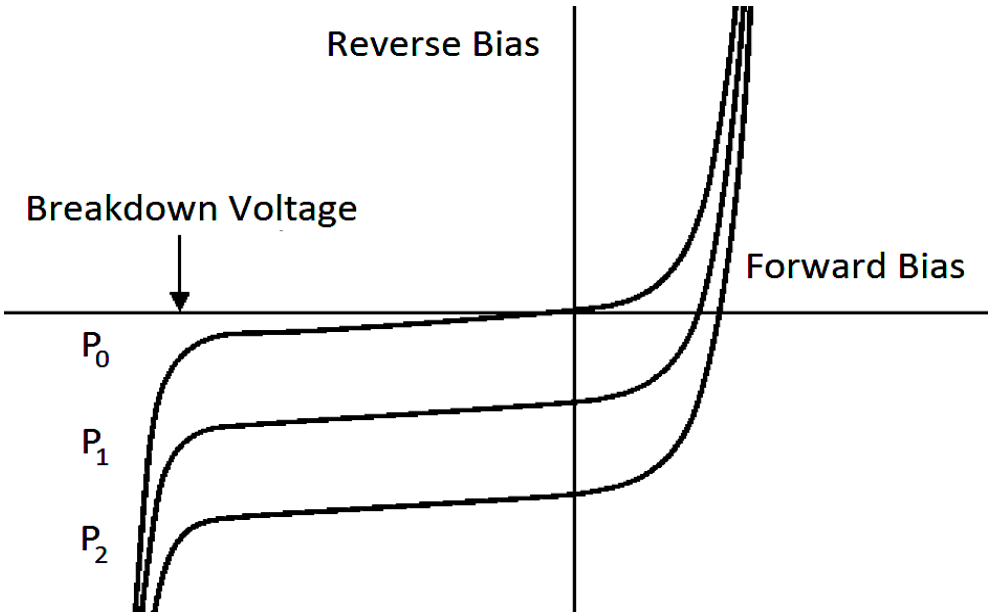

Figure 2.3: Photodiode I-V Characteristics [5]

When the photodiode is forward biased, the current has an exponential increase but if the diode is in reverse bias only dark current is present. Therefore the photoelectric effect can be detected in this region. This is the reason why reverse bias or photoconductive mode is the operating mode of photodiodes in image sensors [5]. This makes sure that only the light intensity affects the generated current. The current can be represented as, see Equation 2.9:

$$I_D = I_{SAT}(e^{\frac{qV_A}{k_B T}} - 1) \tag{2.9}$$

where I_D is the photodiode dark current, I_{SAT} is the reverse saturation current caused by the motion of charge carriers, V_A is the applied bias voltage, k_B is $1.38 \cdot 10^{-23}$ J/K which is the Boltzmann constant and T is the absolute temperature in Kelvin [5].

Noise is the biggest non-ideality affecting the photodiode. Photodiodes are mostly affected by two types of noise, shot noise and thermal noise, also called Johnson noise, see further in Section 2.4.3.

2.2 Pixel Architectures

Pixel architectures are classified into either active or passive pixels. The difference depends on whether the pixel contains signal amplification circuitry or not. With Weckler's publication on the p-n junction in the 1960s, the first passive pixel was presented, see Figure 2.4 [a]. This passive pixel consisted only of one photodiode and a switch, denoted by hv and S_s. If the switch was turned on, the reverse bias was applied. When the photodiode was exposed to illumination, the charges built up depended linearly on the incident illumination density. This photodetector showed advantages towards the former devices known at the time [8]. While CCDs consists only of passive pixels, CMOS has the possibility of being implemented with either passive or active pixels.

From passive pixels in CCDs, the photogenerated charge is transferred without amplifications serially to an output amplifier and an ADC. The image quality can be strongly affected by noise injection during the transfer which causes smear artifacts in the image [4]. Advantages of passive pixel structures include high fill factor, simplicity and a small pixel pitch which is the length from one edge of the pixel to the edge of the next one.

In Figure 2.4 [b] the common architecture of a passive pixel in a CMOS sensor is shown. The pixel consists of a photodiode and a select switch. The charge generated is read out from the pixel and amplified by a charge detection amplifier located outside the pixel array [4]. This photogenerated charge is susceptible to noise between the pixel output and the amplifier. This becomes a significant issue when dealing with a large pixel array.

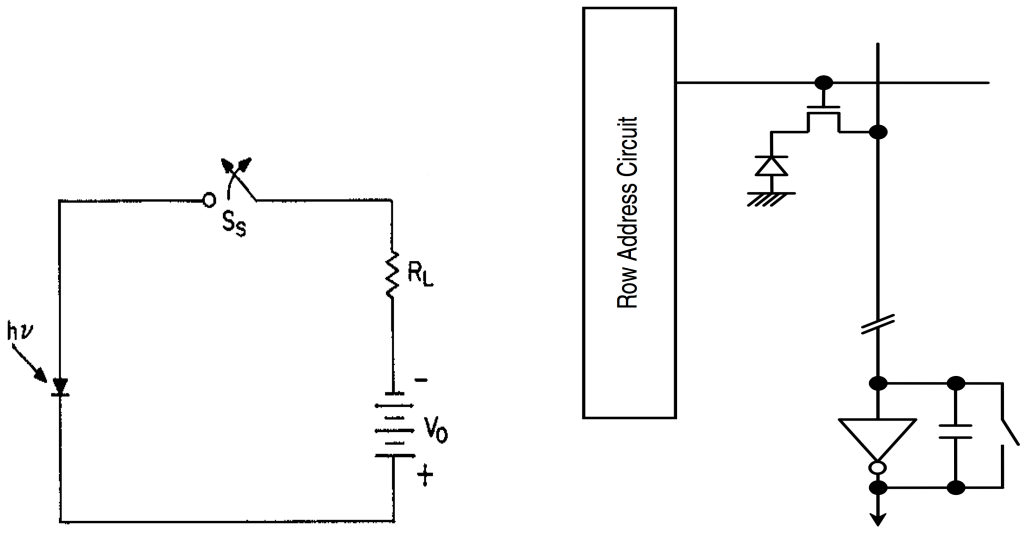

(a) Weckler's Passive Pixel Architecture (b) Common Passive Pixel Architecture

Figure 2.4: Passive Pixel Architectures [4], [8]

The most common charge detection principle used in pixels is with the use of floating diffusion (FD). When the generated signal charge is collected in a potential well, change of the potential occurs, ΔV_{FD}. This can be described with the following relationship, see Equation 2.10:

$$\Delta V_{FD} = \frac{Q_{SIG}}{C_{FD}} \tag{2.10}$$

where Q_{sig} is the signal charge and C_{FD} is the capacitance of the well which acts as a charge-to-voltage conversion. The conversion gain expresses how much voltage change is caused by a single electron. By monitoring this change with a voltage buffer, the output voltage can be expressed as, see Equation 2.11:

$$\Delta V_{OUT} = A_v \cdot \Delta V_{FD} \tag{2.11}$$

where A_v is the voltage gain of the buffer [4].

The second possible implementation on CMOS pixel architecture are active pixels. Active pixel sensors are more complex than the previously mentioned passive pixel sensors. The difference between the two is the active circuitry added into the pixel cell for active pixels. Active pixels have advantages such as low power consumption, high readout speed, high sensitivity and low cost. Multiple active sensors have been developed such as the 3T and 4T active pixels.

Hereon after the focus will be on active pixel sensors due to the fact that they offer more freedom in design and advantages concerning suppression of noise by an option for additional circuitry inside their pixel. With additional circuitry, the noise can be minimized as early as possible which means that big part of the noise is not amplified with the signal to the output of the sensor. This leads to a high performance in active CMOS sensors.

2.2.1 3T Active Pixel

The three transistor (3T) pixel published by Noble in 1968 is among the first presented active pixel, even though years later the name active was decided for this type of pixels [9]. Today the 3T pixel has been improved upon but still has the same working principle. A generated signal charge is collected at a charge accumulation area (depletion region) in the p-n photodiode inside the pixel. Figure 2.5 shows the modern 3T pixel.

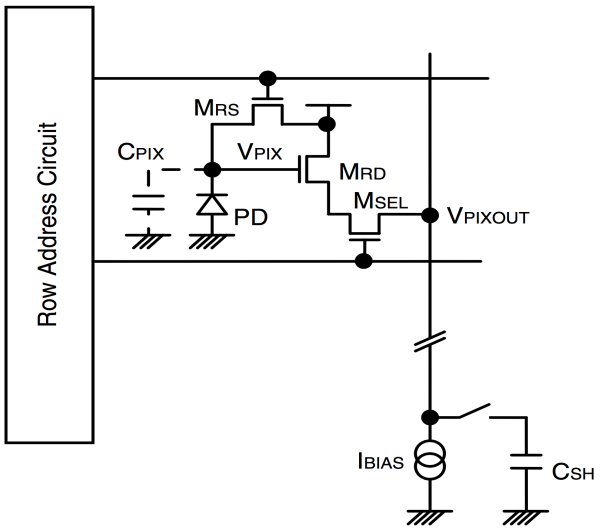

Figure 2.5: 3T Architecture [4], [9]

There, the M_{RS} is the photodiode reset transistor, M_{RD} the amplifier transistor or the source follower and M_{SEL} the select transistor. The reset and the select transistors are connected to

the row address circuit which controls which row is selected to be read out. When the select transistor is chosen, the amplifier transistor and the bias current load source (I_{BIAS}), form a source follower circuit. That means that the photodiode voltage, V_{pix}, is amplified and the buffered output, V_{PIXOUT}, is sampled on the capacitor C_{SH}. This source follower structure amplifies the current [4]. The photogenerated charge gain, A_Q, is given by Equation 2.12:

$$A_Q = A_v \cdot \frac{C_{SH}}{C_{PIX}} \tag{2.12}$$

where A_v is the voltage gain and C_{PIX} is the capacitance of the storage node. Photodiodes have an advantage of offering larger full well capacity than pinned photodiodes. The reason is because the pinned photodiode has a pinned potential which limits the capacity [4].

2.2.2 4T Active Pixel and Pinned Photodiode

A Pinned Photodiode (PPD) has similarities with the p-n photodiode. However, it is superior when it comes to noise reduction due to an added p+ layer on top of the p-n junction. Thus, the photon collection area is kept away from the surface to reduce the noise. The surface of the photodiode is shielded with a p+ layer where the dark current is reduced by keeping the interface non-depleted. Without it, generation and recombination of carriers which occur at the interface would contribute to the noise [10]. Also, due to its complete charge transfer behavior, reset noise is not generated during the transfer. This structure has proven to be highly beneficial in both CCD and CMOS image sensors.

A Pinned Photodiode is the sensing element in the four transistor (4T) pixel which works as follows. The charge is integrated under the PPD and transferred via the Transfer Gate (TG) into a charge storage node called Floating Diffusion (FD). Figure 2.6 [a] shows the 4T pixel structure containing a PPD. In the 4T active pixel structure, TG is the transfer gate transistor which is responsible for separating the PPD and the FD and determines the integration time of a pixel. The reset transistor (RST) or $T1$, is responsible for resetting the potential inside the FD. The amplifier transistor or a source follower, $T2$, enables a low impedance readout. The readout is then controlled by the select transistor, SEL or $T3$. This is then read out as V_{pix} [11].

The function of the PPD can be summarized as in Figure 2.6 [b] where the potential diagram is shown. The electrons are initially located in the PPD marked from $x = 0$ to $x = L_{PPD}$ which is the interface between the PPD and the TG. The Φ_b is the potential barrier where the electrons either cross by thermionic emission or reflect back and continue their random motion in the PPD [11]. The probability of possessing enough energy to cross the barrier can be presented as shown in Equation 2.13:

$$p_{cross} = e^{-\Phi_b/u_{th}} \tag{2.13}$$

where u_{th} is the thermal voltage. When in the FD the charges are converted into voltage. The change in potential, ΔV, is determined by its capacitance and the photogenerated charge, Q_{ph}, which was transferred over the potential barrier. The ratio between the potential change and the photogenerated charges times the electron charge defines the conversion gain [6], see Equation 2.14:

$$CG = q \cdot \frac{\Delta V}{Q_{ph}} \tag{2.14}$$

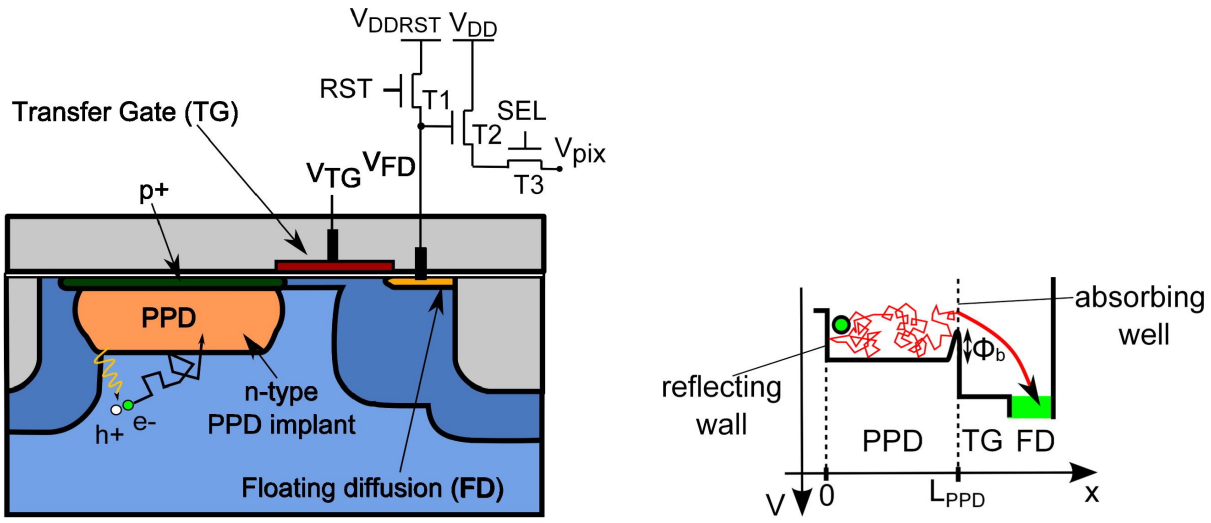

(a) 4T Pixel Structure with PPD

(b) Pixel Potential Diagram

Figure 2.6: 4T Active Pixel Characteristics [11]

The main difference between a 3T and 4T pixel is the specialized transfer gate which separates the charge storage node (FD) and the diode. This allows for a Correlated Double Sampling (CDS) which in short, is the subtraction between the real signal and the reset signal which have been sampled separately.

The operation of the 4T pixel is as follows. The signal charge collection of the pixel starts from the point the FD is reset by the reset transistor (RST) and the output (V_{PIXOUT}) is read as the *reset signal*. The reset signal is a base signal which contains offset and noise from the FD. As the transfer gate is turned on, it causes the accumulated charge at the pinned photodiode to transfer into the FD [4]. With the change in potential at the FD, the V_{PIXOUT} is read out as the *real signal*. Due to the pinning potential, the FD, the collection region, can be fully depleted as it resets. CDS is enabled and eliminates the offset and the noise components which are contained in the FD or the reset noise, 1/f noise and kTC noise [12]. Thereby the advantages of the PPD include a high quantum efficiency, lower dark current and reset noise and as the conversion gain is independent from the photodiode capacitance, it can be tailored for different applications [6]. Disadvantages are the modifications from the standard CMOS process and high reset voltage for a complete transfer.

Figure 2.7 [a] and [b] show the structure of the PPD both in p-type and n-type substrates where *p+, p-, p, n+* and *n* define the doping. The pixel can either be in a p-type or n-type substrate which both have different advantages. The p-type substrate has been more commonly used as it requires fewer modifications from the conventional CMOS process [4]. However, it is more susceptible to pixel-to-pixel crosstalk due to diffusion from carriers generated in the substrate. The n-type region allows for more isolation as the carriers are mostly drained through the n-type substrate. The p-well, for the n-substrate case, has an extended depth in order to work as a blocking region.

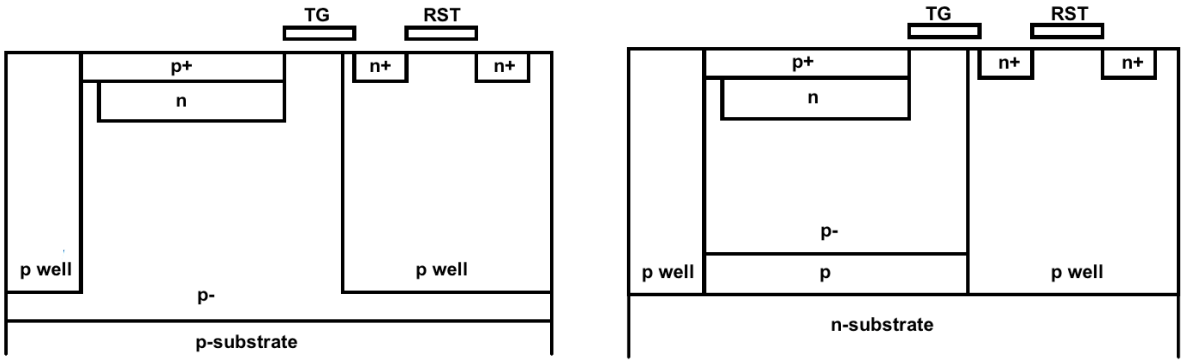

(a) PPD in p-type Substrate

(b) PPD in n-type Substrate

Figure 2.7: Cross-Section View of Pinned Photodiodes in p-type and n-type Substrates [4]

2.3 Readout Techniques

In order to capture the data from an image sensor certain readout techniques have been developed. Global shutter and rolling shutter mode are mechanisms used to read out an image but have different influences on the outcome. When global shutter is used, all pixels in the image sensor are reset at the same time. By resetting the imager any residual signal in the well is removed. After the integration period, determined by the transfer gate, starts there is charge accumulation inside the pixels. The integration period is the same for all pixels. If the integration time is short enough for a certain motion, it is not detected in the scene and does not affect the quality of the image [13].

On the other hand, with rolling shutter mode the pixels do not integrate at the same time. Instead, each row starts to integrate at a different time. Though all pixels have the same amount of integration time, the difference in the start time can affect the images with motion blur. Rolling shutter has an advantage for certain applications, such as electro-optical measurement systems [13]. There the characteristics of the rolling shutter were used to capture light from different heights. By synchronizing the illumination pattern with the rolling shutter features could be captured at specific heights [14]. Other advantages include the lower cost and less complexity in fabrication of CMOS rolling shutter readout.

Readout modes and frame rate are parameters that describe how fast the system can record the data [15]. *Frame rate* is the amount of full frames captured per second and depends on the readout speed, data transfer and the number of pixels. Some cameras have the option of running at a higher frame rate by binning pixels together. However, it has the disadvantage of reducing the resolution. Binning is a technique which enables the possibility of adding two or more output signals together, either on-chip or off-chip. In order to increase the readout rate multiple taps can be added, which means the data is read out in multiple locations instead of only one.

Concerning readout modes, common ones include *Integrate-While-Read* (IWR) or *Integrate-Then-Read* (ITR). For IWR the integration occurs simultaneously to the readout. This allows the highest possible frame rate, both integrating the signal as well as reading it out. For ITR the integration of the next frame occurs after the previous frame is read out. The advantage of ITR is the fact that the integration time is independent of the readout speed. This is highly

beneficial for images which encounter significant motion in the scene. Another advantage is that signal are less likely to be corrupted by the integration mode [16]. The disadvantage of the method is that during a readout an event that happens simultaneously can not be seen. For IWR the integration time is limited by the readout speed.

2.4 Image Sensor Properties

Image sensors have certain features which have to be considered for the optimal performance. In this section a couple of factors will be discussed, such as the Signal-to-Noise Ratio (SNR), Dynamic Range (DR), Modulation Transfer Function (MTF), Resolution, Contrast, Noise and Robustness.

2.4.1 Signal-to-Noise ratio (SNR) and Dynamic Range (DR)

Signal-To-Noise Ratio (SNR) represents the ratio between the input signal and the input referred noise, see Equation 2.15, represented in decibels (dBs):

$$SNR = 20 \cdot log_{10} \frac{N_{sig}}{n} \tag{2.15}$$

where n is the total temporal noise at the signal level N_{sig}. SNR describes the sensitivity of an image and the higher the SNR the less noise the image contains. SNR is improved by increasing the signal (N_{sig}) or decreasing the noise.

Dynamic range (DR) is the ratio between the full well capacity (N_{sat}) and the noise floor (n_{read}), see Equation 2.16, represented in dB:

$$DR = 20 \cdot log_{10} \frac{N_{sat}}{n_{read}} \tag{2.16}$$

The dynamic range shows the ability of the sensor to represent the brightest and the darkest parts in a scene [17]. Increasing the dynamic range in CMOS imagers is achieved by either increasing the largest signal or decreasing the noise floor. With high dynamic range (HDR) sensors the noise floor is decreased as much as possible [18]. The state-of-the-art noise floor is around 1e.

2.4.2 Modulation Transfer Function (MTF), Resolution and Contrast

Modulation Transfer Function (MTF) is used to measure the imaging performance of an optical system [4]. MTF can be closely related to both resolution and contrast. The resolution is a parameter which describes the capability of the sensor to capture object details and can be presented as line-pairs per millimeter (lp/mm) or frequency. The contrast describes how closely a sensor can relate different light intensities between each pixel [4]. MTF describes the filtering properties of the spatial frequency. Characteristic example can be seen in Figure 2.8 where the quality of the objective affects the modulation response as a function of spatial frequency.

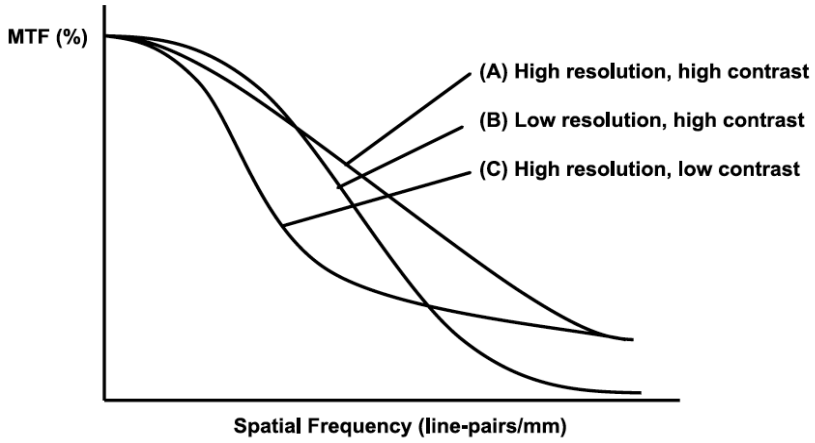

Figure 2.8: MTF Spatial Frequency Characteristics [4]

MTF is decreasing with increasing frequency, represented as line-pairs/mm. This elaborates on how much details can be captured in an image. The higher the MTF is for higher spatial frequencies the higher the resolution is. However, the higher the MTF is at mid-level frequencies the better the contrast of the image is. For a better understanding, Figure 2.9 shows how images are related to the spatial frequency characteristics presented in Figure 2.8.

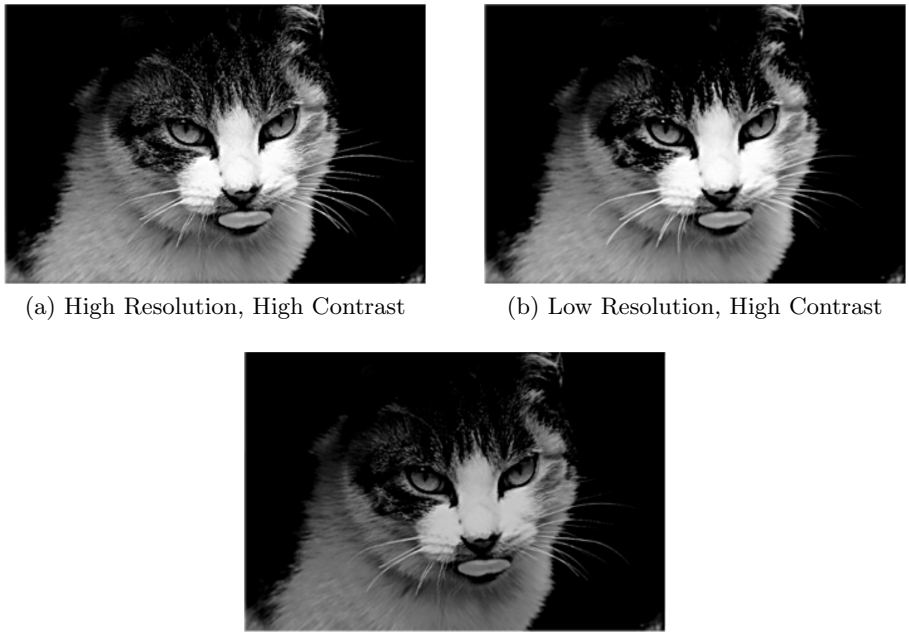

(a) High Resolution, High Contrast

(b) Low Resolution, High Contrast

(c) Low Resolution, Low Contrast

Figure 2.9: Images corresponding MTF Spatial Frequency Characteristics in Figure 2.8 [4]

MTF can be presented as image contrast over the object contrast, see Equation 2.17:

$$MTF(f) = 100\% \cdot \frac{C(f)}{C(0)} \tag{2.17}$$

where $C(0)$ is the contrast of the object measured at low frequencies in order to prevent change in contrast if the frequency is lowered. $C(f)$ is the contrast of the image. Contrast can be

represented as, see Equation 2.18:

$$C = \frac{L_{max} - L_{min}}{L_{max} + L_{min}} \tag{2.18}$$

where L_{max} is the maximum luminance and L_{min} is the minimum luminance.

2.4.3 Noise

One of the major non-idealities of image sensors is noise which leads to a limited SNR. Noise is the random energy which is produced by the material, components and environment of the sensor. In simulations this random energy is described as random fluctuations. Noise is a major limitation in the performance of image sensors and therefore has been deeply studied in order to find solutions for elimination. Noise sources and their causes are various. Different noise sources can be seen in Figure 2.10.

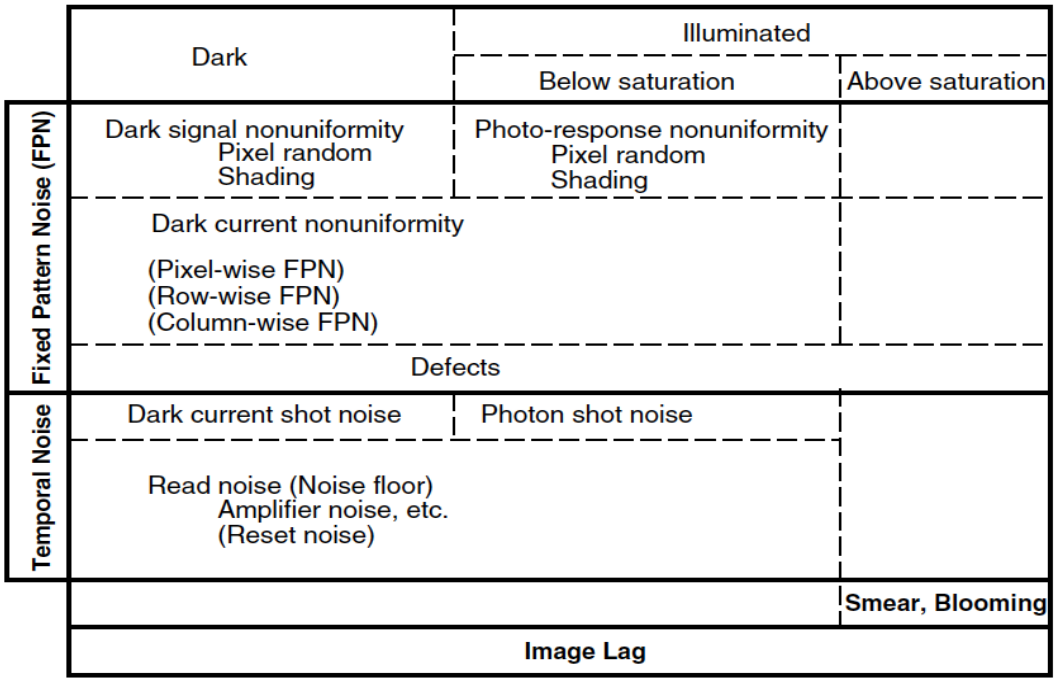

Figure 2.10: Different Noise Sources in Integrated Circuits [4]

As can be seen, the topic of noise in image sensors is extensive and will therefore not be discussed in great detail. Thereby, the description will be limited to:

- Fixed Pattern Noise (FPN)
  - Dark Signal Non-Uniformity (DSNU)
  - Photo Response Non-Uniformity (PRNU)
- Temporal Noise
  - Thermal Noise and Reset Noise
  - Photon Shot Noise and Dark Current Shot Noise
  - Flicker Noise

The noise conditions vary depending on whether the sensor is under illumination or not. When the sensor is under illumination, the noise sources measured in the dark are still present such as DSNU and dark current shot noise.

Fixed Pattern Noise (FPN)

Fixed Pattern Noise (FPN) or spatial noise applies to variations and offsets of signals from pixel to pixel. FPN may be sub-divided into *Dark Signal Non-Uniformity* (DSNU) and *Photo Response Non-Uniformity* (PRNU) depending on if they are measured in the dark or under illumination, respectively. DSNU thereby evaluates both the dark noise as well as the offset cause by variations of transistors between pixels. PRNU values the noise and offset during illumination. The PRNU is due to the photoresponse causing different gain in different pixels with exposure to uniform light. This mismatch is caused by the physical properties of the sensor itself.

The non-uniformity of the dark current is hard to eliminate as the CDS is limited to a constant noise level. Temporal noise, the dark current shot noise, is also present in the dark current. The dark current is formed when the photodiode integrates charges inside a pixel when no outside radiation affects the sensor. The charges are due to random generation of electron-hole pairs in the depletion region. Dark current reduces the full well capacity which at the same time decreases the dynamic range. The dark charge, Q_{dark}, that is integrated is proportional to the integration time, t_{int}, and is also affected by temperature, see Equation 2.19:

$$N_{dark}(T) = \frac{Q_{dark}}{q} = \frac{I_{dark}(T) \cdot t_{int}}{q} \tag{2.19}$$

where $I_{dark}(T)$ is the dark current as a function of the temperature. Dark current can be rooted to three parts inside a pixel. Charge generation in the depletion region, diffusion from the bulk and generation at the surface [4]. It is important to notice how the total dark current is reduced with decreasing temperature, see Figure 2.11, where the X-axis represents the temperature and the Y-axis the dark current (arbitrary log scale).

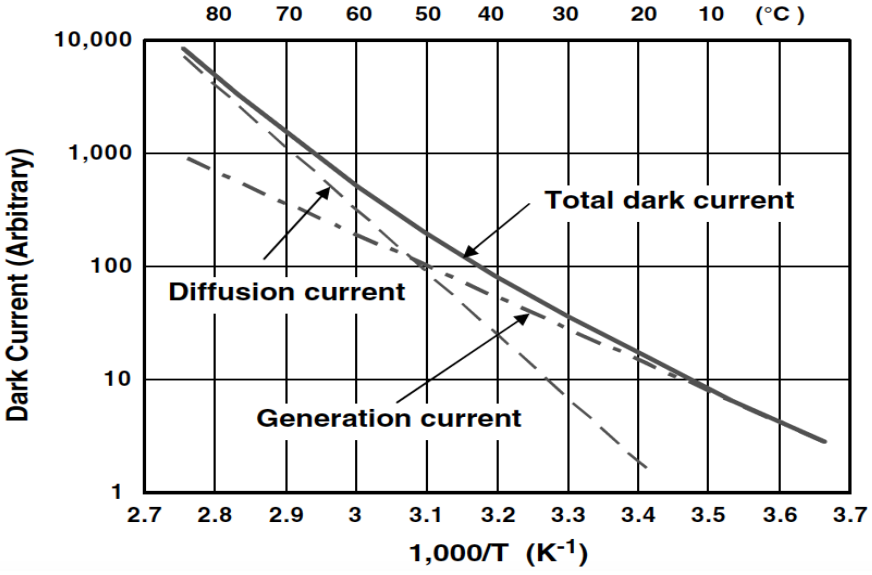

Figure 2.11: Dark Current versus Temperature Dependency [4]

Temporal Noise

Temporal noise describes the random fluctuations within a pixel that change over time. The noise mechanisms in image sensors are thermal noise, photon shot noise and flicker noise alongside dark current shot noise and reset noise.

Thermal noise, Johnson noise, was discovered in 1920s by J.B. Johnson and results from thermal energy affecting the electrons within a resistance. *Reset noise*, also known as kTC noise, has its origin from the capacitance of the floating diffusion. The noise is caused by the thermal noise from the MOSFET transistor. With some pixel structures the kTC noise can be suppressed by CDS. *Photon shot noise* is caused by the variations in the arrival of photons and the generation of electron-hole pairs. This random behavior can be described by the Poisson probability distribution. Under high illumination photon shot noise is the dominating noise source. *Dark current shot noise* is introduced by the dark current which was discussed and presented in Figure 2.11. *Flicker noise* is dependent on frequency with the power spectral density of $1/f$. In CMOS sensors the pixels suffer from flicker noise at low frequencies but if the sampling is short enough CDS can eliminate the noise [4].

Noise sources and their noise densities are summarized in Table 2.1.

Table 2.1: Temporal Noise Sources

Noise Source	**Noise Density**
Thermal Noise	$v_n^2 = 4k_BTR\Delta f$
Reset Noise	$v_n^2 = \frac{k_BT}{C_{PD}}$
Photon Shot Noise	$v_n^2 = \frac{qI_{ph}t_{int}}{C_{PD}}$
Dark Photon Shot Noise	$v_n^2 = \frac{qI_{dk}t_{int}}{C_{PD}}$
Flicker Noise	$v_n^2 = \frac{K}{fC_{ox}WL}$

Here, k_B is the Boltzmann constant, T is the absolute temperature, R is the resistance, Δf is the bandwidth in Hertz, C_{PD} is the capacitance of the photodiode, I_{ph} and I_{dk} are the current from the photons and the dark current, respectively, t_{int} is the integration time, K is a technology parameter, f is the frequency, C_{ox} the oxide capacitance of the transistor and W and L is the gate width and the gate length of the transistor, respectively [19].

2.4.4 Robustness

Robustness is highly important as when manufacturing a device, development mistakes and inaccuracy have to be accounted for. As described previously, environmental factors influence the noise level of the sensor. Environmental factors include humidity, temperature, exposure to gas and exposure to radiation. Nevertheless, robust chips are routinely built, such as CMOS circuits which have large noise margins and are minimally sensitive to variations in transistors [20]. For interested readers this section discusses some contributing factors to errors which designers need to be aware about to ensure robustness. These include developed CMOS processes, expected variability and reliability.

CMOS Processing Technology

With complex CMOS processing technology, fabrication plants and foundries, keep up with eager consumers. Foundries such as TSMC, X-FAB and UMC sell space on their fab lines where

the design has to concede to their foundry model and design rules. In order to make sure for a working design, physical processes should be kept in mind [20].

CMOS processing is broadly done in two steps, in the Front-End-of-Line phase where the transistors are formed and in the Back-End-of-Line phase where the wires are built in. The big parts of this process are wafer formation and photolithography. The wafer is formed from a single crystal silicon which can be made by a crystal growth method such as the Czochralski process. When in formation, impurities are added during the melt to contribute to required electrical properties. In order to initiate the crystal growth a seed crystal is added to the melt. When the seed is withdrawn from the melt the diameter of the wafer is determined. Photolithography is a technique that is designed to write the functions of the chip onto a wafer. By using a mask, photolithography is able to write the patterns onto the wafer. The patterning process determines the dopants, polysilicon, metal and contacts of the circuit using masks. These processes are very complex and extensive and will not be presented further in this chapter. By keeping the specific layout design rules from the foundries in mind and why they are set, faulty chips can be avoided. CMOS processes are constantly improving and new features introduced annually.

Variability

Variability describes how much deviation is expected from the device. When fabricating IC components they are never perfectly identical and imperfections have to be accounted for in the device. Variation sources can be due to Process, Voltage and Temperature (PVT) variations. The circuit should be able to operate in the extremes of these variations in order to show good performance and precautions should be taken during design. Supply voltages of the chip vary within the chip area and with time. This can affect the speed, as the speed is determined by the V_{DD} and the noise budget [20]. With the rise of temperature, the drain current decreases and ambient temperature ranges are different whether it concerns commercial, industrial or military standards. Finally, the process causes variations on the chip. Very important variations are the channel length (caused by effects in the photolithography) and the threshold voltage (caused by different doping and annealing effects). Threshold voltages change with time as the transistors wear out. Variations for the interconnects have to be accounted for in the design.

Reliability

Reliability can be referred to as time-dependent variability and describes how reliable certain devices are. This concept is of high importance when certifying a sensor in order to be sure of its behavior in real time and over a long period. Failures can be sorted into hard or soft errors. Hard errors can cause the circuits to fail permanently, for example due to oxide wearout and interconnect wearout. Oxide wearout is mostly caused by stress which changes the threshold voltage. This causes an increase in leakage which can cause failures in circuits. Mismatches are too high, transistors too slow or too much leakage. Also too high currents can cause an interconnect wearout. Soft errors are random errors which can be triggered by radiation and cause the circuit to fail or loose data [20].

Part I

Optical Tomography

3
Optical Tomography

Computed Tomography is widely used in medical imaging applications and is beneficial for diagnostic procedures. Computed Tomography is a method of producing an image of an internal structure of a subject by reconstructing cross-sectional slices. The cross-sectional slices are taken from different angles of the subject and can be processed into three dimensional images. In order to capture the internal structure, interactions between a subject's tissue and the light source energy are estimated. The data captured by the sensors can be used to reconstruct the internal structure. Energy sources can be X-ray, Neutron, Light, Sound, Electrical and more. There is a vast variety of Computed Tomography disciplines using these energy sources such as X-ray Tomography, Magnetic Resonance Imaging, Neutron Tomography, Ultrasound Tomography and Optical Tomography. These techniques all have their own advantages in applications which depend on their properties and resolution [21].

In order to form an understanding of Tomography, a well known X-ray Tomography imaging method is presented. The underlying tomographic principles between the disciplines are similar. Due to the high energy X-ray waves, broken bones can easily be imaged. When X-rays are used as a radiation source in Tomography, the rays are able to penetrate through the body and the internal structure can be calculated from the data which the sensor on the other side of the subject detected. However, the disadvantage of this method is its probability of damaging the cells of the body and risk of cancer or other diseases. X-rays are electromagnetic radiation with a small wavelength of 0.1 to 10 nm. Contrast of the image depends on the differences in the density and thickness of the structures inside the body. In X-ray Tomography the challenging task is to decrease the harmful side effects. This is done by lowering the dose exposure to patients either by reducing the projection views as in limiting the amount of images or lowering the tube current. X-rays are generated by the interaction of accelerated electrons with a metal (tungsten) within a vacuumed tube. The tube current affects the acceleration of the electrons. The process structure can be seen in Figure 3.1.

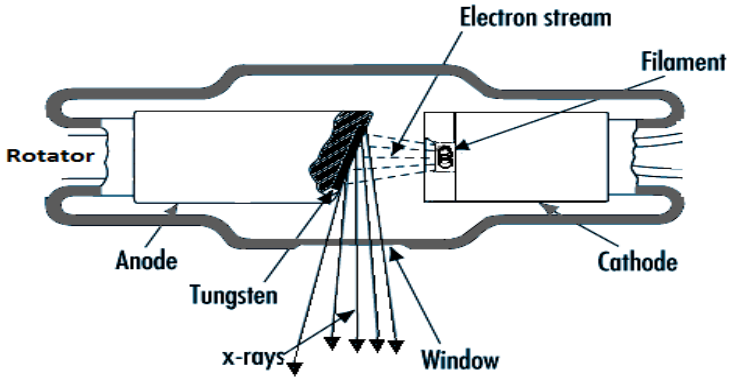

Figure 3.1: X-ray Tube Process

As the tube current is increased with a high filament voltage, it accelerates the electrons to high speed inside a vacuum towards a tungsten target. The energy released is mostly in the form of heat but alongside X-rays are generated and directed towards a subject. In order to prevent the anode from melting, the tungsten metal rotates to dissipate this heat. By using these methods to decrease the X-ray dose the image quality suffers due to added noise and artifacts. Advancements over the last years have shown improved noise and artifact suppression in low dose X-ray Tomography [22]. There is a known health issue for the subjects of the X-ray Tomography and despite efforts in developing low dose X-ray Tomography, their influence has yet to be proven harmless.

In this chapter Optical Tomography is presented, which uses visible and NIR light sources. There are multiple reasons for pursuing optical imaging which include [23], but are not limited to:

- *Radiation Safety*: Due to the non-ionizing rays, no harm is caused to us or the environment.
- *Resolution*: Capable of imaging in the micrometer or sub-micrometer scale.
- *Optical Spectra*: Capable of providing information on molecular conformation.
- *Optical Absorption*: Capable of enabling functional imaging.
- *Optical Scattering Spectra*: Capable of providing information on the size of cell nuclei.
- *Optical Polarization*: Capable of providing information on tissue components.
- *Optical Frequency Shifts*: Capable of providing information on blood flow with the Doppler effect.

On the other hand, the disadvantages of Optical Tomography is the complexity of reconstruction algorithms and imaging depth. In Section 3.1 the operating principles and components of Optical Tomography systems are explained. By comparison, the properties and possibilities of the components are discussed. In Section 3.2 optical properties of silicon and light range are presented and their complexity is discussed. Finally, in Section 3.3, the importance of reconstruction methods are mentioned briefly.

3.1 Theory

Optical Tomography is defined as a tomographic technique which uses a light source in the spectrum ranging from visible to NIR light to acquire an image. It uses the general concepts from other tomographic techniques where the image is reconstructed from the output data using a known function of the matter being imaged. It is a type of an inverse problem where the results are used to find the cause. Opposite to it, is the forward problem which describes a process were the causes define the results. Optical Tomography is a form of computed Tomography where reconstruction algorithms can be applied to reconstruct a 3D model of the subject. In most cases the set-up of Computed Tomography includes three parts, a light source, subject and a detector. Reconstruction algorithm is an important part of a Tomography system as it represents the data in an understandable form on the computer interface. The set-ups for both Optical Tomography and X-ray Tomography are closely related [24], [25]. Below a rough sketch of Computed Tomography set-up is presented, see Figure 3.2.

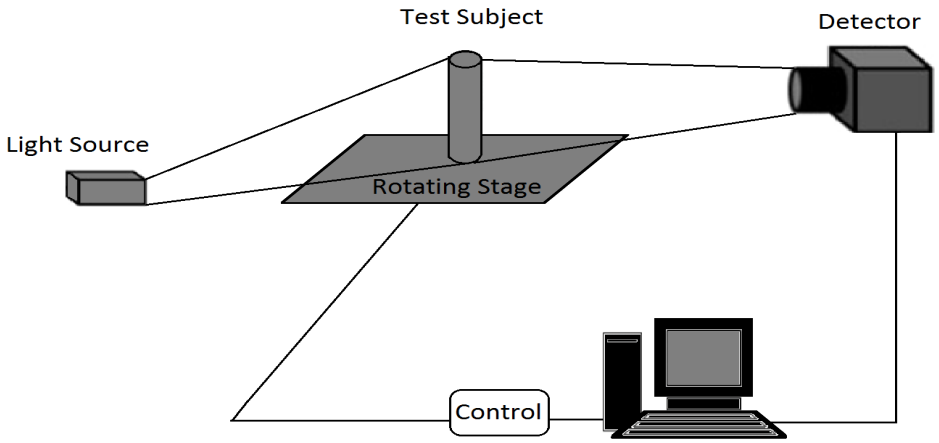

Figure 3.2: Computed Tomography Explanation Set-Up

The optical light source or X-ray emits radiation onto the test subject whereas on the other side a detector is placed. The rotating stage is then used to rotate the subject in order to retrieve slices from other angles. Finally, the image is presented after reconstruction on the computer interface. Each part of the system has its own properties and possibilities. In the following subsections 3.1.1, 3.1.2 and 3.1.3, light sources, subject tissue properties and detectors are discussed in more detail. Detectors are either in the form of an image sensor in free space or with fibre optics and a photodetector. In this thesis the focus is on image sensors although the fibre optic systems are briefly discussed in relation to the newly developed methods.

3.1.1 Light Source Properties

The choice of the optimal light source depends on the sample to be imaged and detected but the light absorption and scattering of the tissue affects the image quality [26]. Most commonly used light sources for Tomography are the Light-Emitting Diodes (LED) and Super Luminescent Diodes (SLDs). Mainly because they have a high spectral irradiance and relatively low cost. Spectral irradiance is a way to characterize a light source and describes the power density at certain wavelength [27]. With higher spectral irradiance, images with higher qualities can be retrieved [26].

In Optical Tomography light sources in the visible and NIR region, wavelengths ranging from 400 nm to 1100 nm, are used. The penetration depth by a light source into a biological tissue is dependant on its wavelength. The power intensity from a light source can be described with a Gaussian distribution. An important parameter describing the distribution is the spectral bandwidth. Spectral bandwidth is defined as the Full Width at Half Maximum (FWHM) of the Gaussian power intensity distribution [28]. With a wider spectral bandwidth a higher resolution can be achieved [26].

Light source output characteristics are wavelength, pulse duration, radiation energy, power, intensity and divergence [29]. The light source can generate various types of waves such as pulsed waves, continuous wave, amplitude modulated waves or frequency dependent waves. Continuous wave (CW) source is a simple and commonly used source. Pulsed source generates pulses which

propagate through the tissue. Depending on the source, the shape of the pulse propagates, broadens and alters inside the tissue due to different effects. From this behavior, scattering and absorbing features can be predicted [30]. As the human tissue reacts differently to wave forms, the dependence of the light wave and the tissue are important. As an example, pulse light behavior can be described by an ON and OFF wave. Pulsed light offers advantages such as when the wave is in its OFF period, the light source generate less tissue heating. This is advantageous in case of heating a target tissue and not its surroundings [31].

3.1.2 Tissue Optical Properties

The way tissues react to light is complex due to scattering properties. Opposite to the X-ray computed Tomography, the reconstruction algorithm can not easily predict the internal structure from the absorbing nature, as other properties of the tissues will have intertwined their effects into the data which have to be accounted for. Ongoing research is conducted in order to find better ways to improve the image quality. Reconstruction algorithms will be further explained in Section 3.3.

Depending on the biological nature of the tissue different reactions are caused by different energy sources. When radiation falls on a transparent tissue, refraction has the highest influence on the outcome but with opaque tissues absorption and scattering play the biggest role. This dominant effect depends on the compound and characteristics of the incident radiation [29]. When it comes to biological tissues, water molecules, proteins and pigments have high absorption coefficients. Water transmits radiation into tissue structures which is a fundamental biological function. Hemoglobin and melanin also play big parts in radiation absorption in the human tissue. Hemoglobin, a protein, inside red blood cells carries oxygen from the lungs to tissues (*oxygenated hemoglobin*) and carbon dioxide from tissues to the lungs (*deoxygenated hemoglobin*). Melanin, a pigment, is an important compound which absorbs UV light and reduces the risk of cancer.

Figure 3.3 shows how different components in the biological tissue react to different wavelengths with changes in the absorption coefficient. For example concerning scattering, the longer the wavelength, the less energy and scattering the wave has inside the tissue. Also, it demonstrates how melanin and hemoglobin have higher absorption response than water in the so called *NIR window* [30]. The importance of the NIR window is that the absorption coefficient is lower than at other wavelengths as well as the scattering is approaching its minimum. The absence of these two factors allows for an increase in the penetration depth and thereby imaging depth.

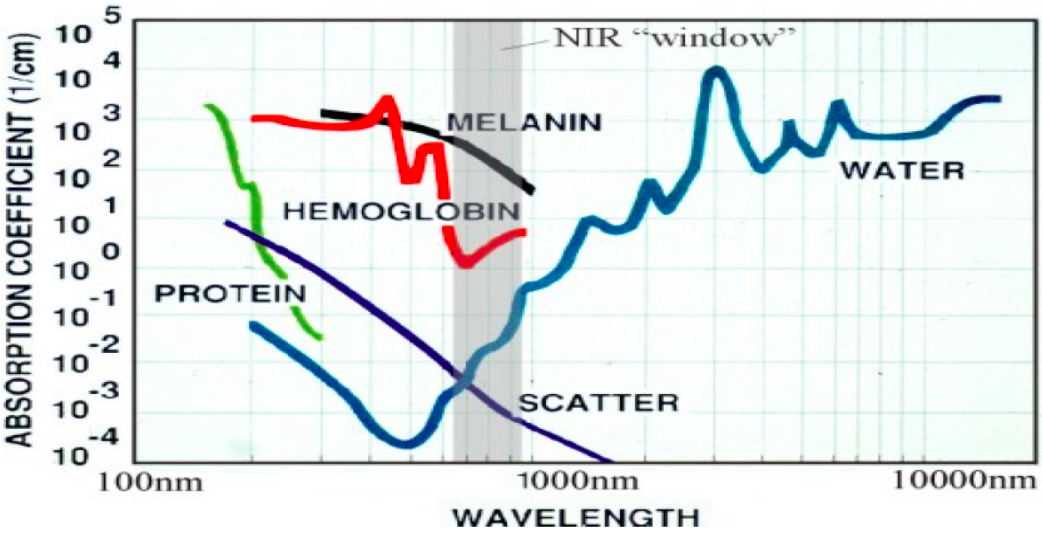

Figure 3.3: Optical Properties in Tissues [30]

It is concluded that it is preferable to measure the performance in the NIR range than the visible light range due to the lower effects from the scattering and water absorption in that region. Therefore it can provide better image quality and reliability on the data. The diagnostic possibilities of NIR were discovered by Horecker in the 1940s [32]. His research showed that the properties of absorption of oxygenated hemoglobin (HbO_2) and deoxygenated hemoglobin ($HbCO$) in the NIR region was different from the visible region. Figure 3.4 shows the absorption spectrum of HbO_2 and $HbCO$ in the visible region while Figure 3.5 is the absorption spectrum in the NIR region. The X-axis shows the wavelength in *nano meters* and Y-axis the specific absorption coefficients, [1 x 10^{-6} $cm^2/mole$].

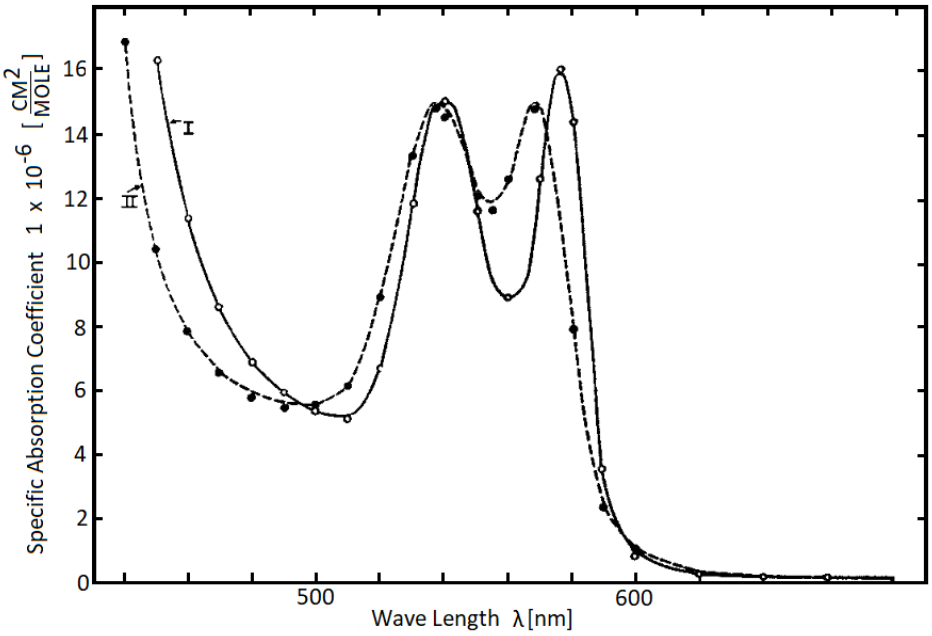

Figure 3.4: Absorption Spectrum of HbO_2 (I) and HbCO (II) in the Visible Region [32]

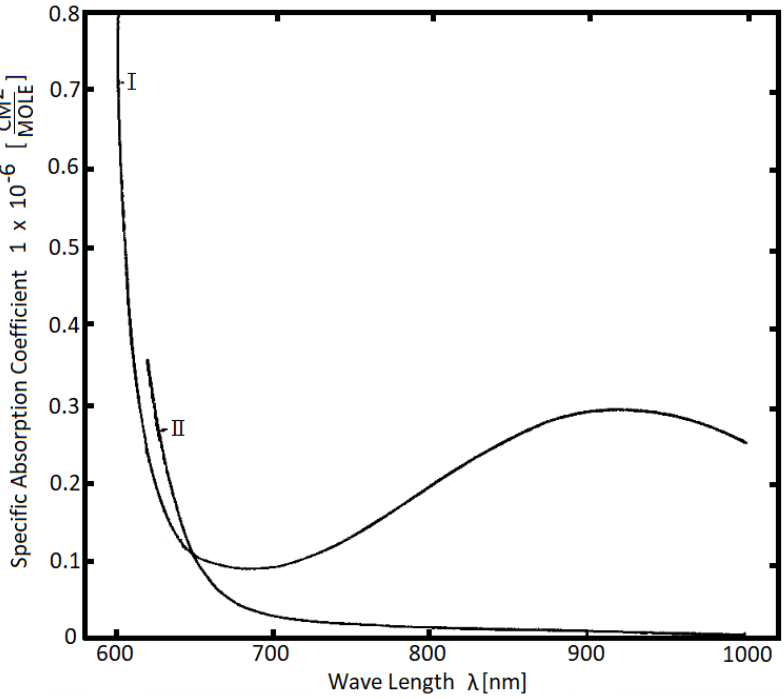

Figure 3.5: Absorption Spectrum of HbO_2 (I) and HbCO (II) in the NIR Region [32]

By comparing Figure 3.4 and 3.5 the difference between the oxygenated and deoxygenated hemoglobin in the NIR range and the visible range can be seen. Healthy function of the tissue depends on the blood supply and this allows for a way to monitor if there is sufficient oxygen transfer with the hemoglobin to certain tissues.

Optical Tomography has different applications which depend on what behavior is being measured. These behaviors are diffusion, projection, fluorescence and coherence. Diffuse Optical Tomography (DOT) is based on NIR light source and inverse computations. This type of tomography has shown potential in imaging on both macro and micro scales. There is imaging of a neonatal brain, breast and muscles as well as other functional, cellular and molecular parameters, see [30], [33]. Optical Projection Tomography (OPT) can use visible light for illumination. It collects projections by rotating the sample around, which can then be used to reconstruct a 3D image. However, in order to image a tissue with OPT, it first has to be made transparent with certain optical clearing techniques so the light can pass through. But if the object has the same refractive index as water, clearing is unnecessary. The advantage of this imaging technique is the possibility of being able to image both in transmission and fluorescent based modes, which can make use of the specific stained tissues or genes [34]. The disadvantage is the time-consuming clearing technique when necessary.

Fluorescence Tomography (FT) is often applied to molecular imaging and has great potential in preventing and treating diseases [35]. This technique is based on NIR light source and is an emerging technique due to the recent availability of fluorescent labelling proteins, dyes and probes. This enables non-invasive study of gene expression and cellular processes [36]. Optical Coherence Tomography (OCT) is based on low-coherence interferometry and its illumination source ranges from the visible to the NIR spectrum. Due to OCT possibilities using CMOS image sensors in existing publications, Chapter 4 includes a detailed explanation of this technique.

As mentioned before, the light/tissue behavior is different depending on penetration depth. Due to this variability, reconstruction algorithms are difficult to configure and program. Behavioral properties in light/tissue interactions include absorption, scattering, reflectance, transmission and fluorescence, see Figure 3.6.

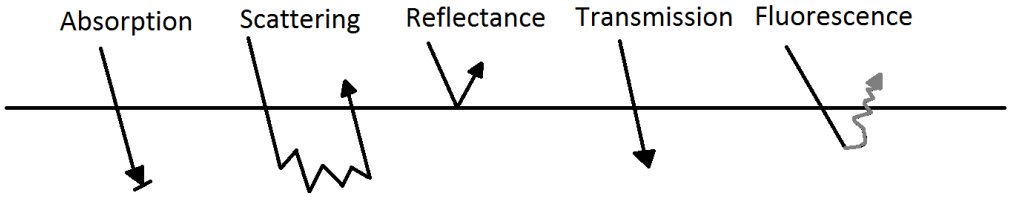

Figure 3.6: Light Tissue Interaction

All these factors are determined by the wavelength of the light and the tissue. By using these behaviors different techniques can be applied in order to retrieve as much information from an Optical Tomography system as possible.

Absorption

When light penetrates the skin the light wave is absorbed and the energy is converted into heat. The behavior of the light through a non-scattering medium or scattering medium is different. The behavior of the light intensity, I, through a non-scattering medium can be described with Beer-Lamberts law, where the amount of energy that is absorbed affects the initial intensity, I_0, exponentially, see Equation 3.1:

$$I = I_0 \cdot e^{-\mu_a(\lambda)x} \tag{3.1}$$

where $\mu_a(\lambda)$ is the absorption coefficient and x the width of the sample. The absorption coefficient represents the probability of a photon being absorbed into the tissue and can be represented as follows, see Equation 3.2:

$$\mu_a = \sigma_a \cdot N \tag{3.2}$$

where σ_a is the effective absorption cross-section per molecule and N is the amount of absorbing molecules per unit volume [37].

Scattering

In tissues, scattering properties of a medium can be described by a scattering coefficient, μ_s [30]. The scattering behavior is complex and is different depending on the characteristics of the tissue and its property [38]. Scattering in tissues can be sub-grouped into either Mie scattering or Rayleigh scattering. Mie scattering of particles occurs when the wavelength of the light is in the same order as the particles. Rayleigh scattering happens when the wavelength is much longer than the size of the particles. Mie scattering is dominating in tissues and is mostly anisotropic [37]. An anisotropic factor or Landé's factor, g, can be used in order to define a reduced scattering coefficient, μ_s'. The factor describes the degree of forward scattering which can be described by the Henyey-Greenstein phase function. Forward scattering describes the scattering of radiation with less than 90 degrees deviation from its original course. For photon

scattering in tissue, g is typically 0.8–1 [39]. The reduced scattering coefficient which describes a multiple scattering process can be presented as, see Equation 3.3:

$$\mu_s' = \mu_s \cdot (1 - g) \tag{3.3}$$

where μ_s is derived from a combination of the absorption coefficient, path length dependent on relative scattering events and intensity losses due to geometry [30].

As Optical Tomography techniques have been used from micro to macro scale it is important to mention the difference in the absorption and scattering coefficients depending on the size and the composition of the tissue [30]. In Figure 3.7 different types of tissues are compared with absorption coefficients, reduced scatter coefficient and relative Landé's factor, g. The changes in coefficients between similar tissues give an idea on how the shape and size influences the behavior. However, these measurements are difficult to retrieve *in vivo* due to technological limitations and therefore might vary [30].

Tissue	Absorption coefficient μ_a (mm^{-1})	Reduced scatter coefficient μ'_s (mm^{-1})	g
Blood (arterial) (98%, 2m mol/L)	0.398 (at 800 nm)	1 (at 800 nm)	-
Blood (venous) (75%, 2m mol/L)	0.396 (at 800 nm)	1 (at 800 nm)	-
Blood partially oxygenated (Cheong *et al*, 1990)	1.55 (at 760 nm)	0.79 (at 760 nm)	0.9972
Brain (24 wk gest neonate) (van-der-Zee, 1992)	0.0215 ± 0.02 (at 800 nm)	0.748 (at 800 nm)	0.718
Brain (28 wk gest neonate) (van-der-Zee, 1992)	0.0373 ± 0.01 (at 800 nm)	0.673 (at 800 nm)	0.919
Brain (White matter 40 wk gest neonate) (van-der-Zee, 1992)	0.0373 (at 800 nm)	0.659 (at 800 nm)	0.981
Brain (Grey matter 40 wk gest neonate) (van-der-Zee, 1992)	0.0460 (at 800 nm)	0.529 (at 800 nm)	0.983
Brain (grey adult) (Cheong *et al*, 1990)	0.27± 0.02 (at 632.8 nm)	2.06± 0.2(at 632.8 nm)	0.94±0.004
Brain (white adult) (Cheong *et al*, 1990)	0.22± 0.02 (at 632.8 nm)	9.1± 0.5(at 632.8 nm)	0.82±0.01
Bone (pig skull) (Firbank *et al*, 1993)	0.025 (at 800 nm)	1.8 (at 800 nm)	-
Cerebrospinal fluid (CSF) (from water (Hale *et al*, 1973))	0.0022 (at 800 nm)	~0	-
Skin: Dermis (inc Epithelium) (Simpson *et al*, 1998)	0.013 (at 800 nm)	2 (at 800 nm)	-
Skin: Subdermis (Simpson *et al*, 1998)	0.008 (at 800 nm)	1.2 (at 800 nm)	-
Muscle (exsanguinated abdominal) (Simpson *et al*, 1998)	0.03 (at 800 nm)	0.7 (at 800 nm)	-
Breast (glandular) (Cheong *et al*, 1990)	0.05±0.01 (at 700 nm)	1.4±0.3 (at 700 nm)	--
Breast (adipose) (Cheong *et al*, 1990)	0.07±0.01(at 700 nm)	0.9±0.1 (at 700 nm)	--

Figure 3.7: Optical Coefficients in Tissues [30]

Reflectance

Reflectance is the observed behavior of light when the light wave is reflected by a subject or a tissue. The refractive index describes the behavior of a tissue and can be used to calculate the speed of the wave inside the following tissue, see Equation 3.4:

$$c_{medium} = \frac{c}{n} \tag{3.4}$$

where c_{medium} is the speed of light in the medium, c the speed of light in vacuum, $2.99 \cdot 10^8$ m/s and n is the refractive index of the medium. However, Snell's law can be used to describe the behavior of the refractive index between two substances, see Equation 3.5:

$$n_1 \cdot sin(\theta_1) = n_2 \cdot sin(\theta_2) \tag{3.5}$$

where n_1 and n_2 represent the junction between the different substances and θ the wave angle towards and from the junction [30]. The reflectivity, R, for normal incidence can be given by Equation 3.6, derived from the Fresnel Equations [23]:

$$R = |\frac{n_1 - n_2}{n_1 + n_2}|^2 \tag{3.6}$$

Transmission and Fluorescence

Transmission can be explained as the direct behavior of light but occurs rarely in tissues. Transmission of light varies between tissue and the wavelength of the source. After penetration into the skin the transmission behavior increases with longer wavelengths [40]. Fluorescence is an emission type of behavior which can occur after a tissue has been radiated by light. The tissue emits a light of lower energy with longer wavelength than it absorbed. This effect has shown its use in Fluorescence Tomography as by measuring the emission at certain frequency isolates the data from the background. However, in order to detect a region of interest a fluorescent labelling is necessary for high sensitivity. The fluorescent labelling is called fluorophore and ideal fluorophore for ultra sensitive fluorescence detection must have a high absorption coefficient, a high fluorescence quantum yield and strong, long lasting emission for high quality images [41].

3.1.3 Detector Properties

As mentioned before Optical Tomography systems can be equipped with both image sensor (CCD or CMOS) or a single photodetector, for fibre optic systems, as their detectors. In order to retrieve a high quality image the sensors have to be optimized towards their application. Chapter 4 will be devoted to the detectors of Optical Coherence Tomography systems alongside its system explanation. This section is seen to give a brief introduction to the detectors used both for systems based with fibre optics and photodetectors and the ones who use CCD detectors.

Fibre optics and a photodetector have been widely used to detect the signals in Optical Tomography [42], [43]. The basis of fibre optics consists of a core, light travelling path, and a cladding, which is the wall around the light path. A simple line of work is as the light is sent through the optic wire, the sample response is sent back to a simple photodetector, demodulator and an ADC. However, some Optical Tomography systems have complex cameras instead of a photodetector to receive the data from the fibre optics. A fiber optic based system in OCT will be described in Chapter 4.3.1.

CCD image sensors were presented in Chapter 2, however, they have a derivation called Electron Multiplication CCDs (EMCCDs). This structure has additional multiplication register where the signal charge packet delivered to the output of the sensor undergoes a multiplication process. The advantage of this is a great increase in the SNR gain. This type of sensor has a great advantage when it comes to extremely low signals. However, in high speed imaging the noise increases to the limit where the noise difference is neglectable between EMCCD and a CMOS. Under such terms the EMCCD sensor dissipates more power than a CMOS sensor would dissipate on average [44].

However, to give a better idea of CCD (iXon3 860, ORCA-ER) and EMCCD (ImagEM-1k) image sensors in tomographic application, a summary of sensors used in different applications

can be seen in Table 3.1. As DOT is an application which has low light levels, EMCCD cameras are the optimal.

Table 3.1: Comparison of CCD and EMCCD Image Sensors in Optical Tomography

Application	**FT** [45]	**FT** [46]	**DOT** [47]
Sensor	iXon3 860	ORCA-ER	ImagEM-1k
Sensor Type	CCD	CCD	EMCCD
Pixels	128 x 128	1344 x 1024	1024 x 1024
Pixel Size (μm)	24 x 24	6.45 x 6.45	13 x 13
Pixel Well Depth (e-)	160000	18000	400000
Read Noise (e-)	<1	6	19
Frame Rate (fps)	513-14025	8.3-45	18-62

3.2 Limitations of Silicon

Another aspect concerning the development of detectors in a tomography system is the light interaction with silicon. With factors ranging from the light source, tissue interaction and different detectors influencing the image quality, the material used for detection is highly important for the image quality.

The bandgap energy of silicon, E_g, as mentioned before, determines the minimal level of energy a photon has to possess in order for a photon-to-signal charge conversion to take place, see Equation 3.7:

$$E_{photon} = \hbar v = \frac{\hbar c}{\lambda} \geq E_g \tag{3.7}$$

where E_{photon} is the photon energy. The amount of photons absorbed by the silicon with thickness is proportional to the photon flux. Photon flux represents the amount of photons per second per unit area. The bandgap energy in silicon is 1.12 eV which means that for wavelengths longer than 1100 nm, silicon is transparent, as their energy level is lower than the bandgap energy. A derivation of the relationship of photon flux presents how the flux decays exponentially with the distance from the surface. This can be described by Beer-Lambert law, see Equation 3.8 [4]:

$$\Phi(x) = \Phi_0 \cdot e^{-\alpha x} \tag{3.8}$$

where α is the absorption coefficient and x is the distance from the surface. The behavior of the light in silicon can be viewed in Figure 3.8 [a] and [b], as a function of absorption and flux, respectively.

Figure 3.8 [a] shows the absorption coefficient decreasing with the increasing wavelength, thereby loosing its quality of changing photons to signals, retrieving lower photon-to-signal charge conversion rate. Figure 3.8 [b] shows how the light decays with distance from the surface. This behavior depends on their wavelength, when the photon flux decays to 1/e, the depth for the wavelength of 600 nm is 2.44 μm. This indicates that for longer wavelengths larger depth is required.

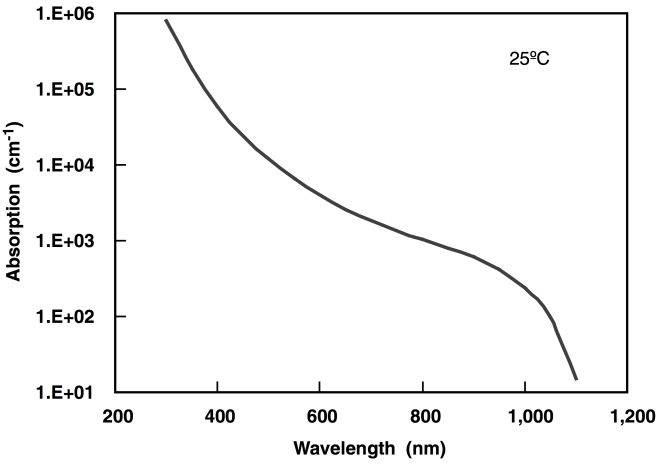

(a) Absorption Coefficient versus Wavelength

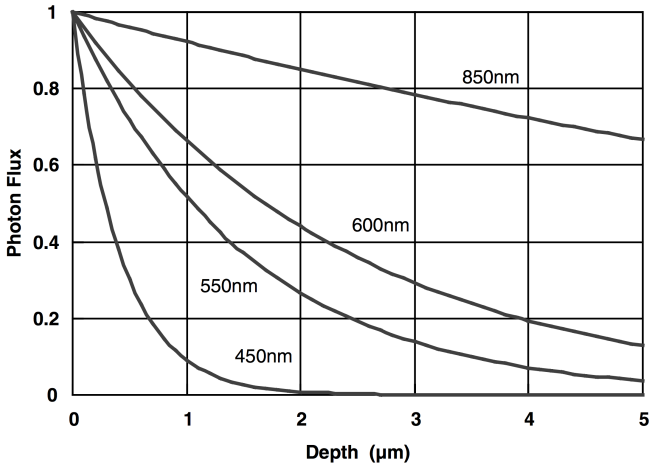

(b) Photon Flux versus Depth

Figure 3.8: Absorption in Silicon [4]

3.2.1 NIR and Visible Light Range

Quantum efficiency, like mentioned in Chapter 2, describes how many electrons contribute to the photocurrent compared to the incoming photons. Noting the optical losses, for example due to reflection. This parameter is prospective to use in order to show the efficiency of silicon in image sensors. The quantum efficiency of silicon is optimal in the visible range but has a low response around 1000 nm. Other detectors such as Indium Gallium Arsenide (InGaAs) photodiodes show a good response in the NIR range and for longer wavelengths, see Figure 3.9.

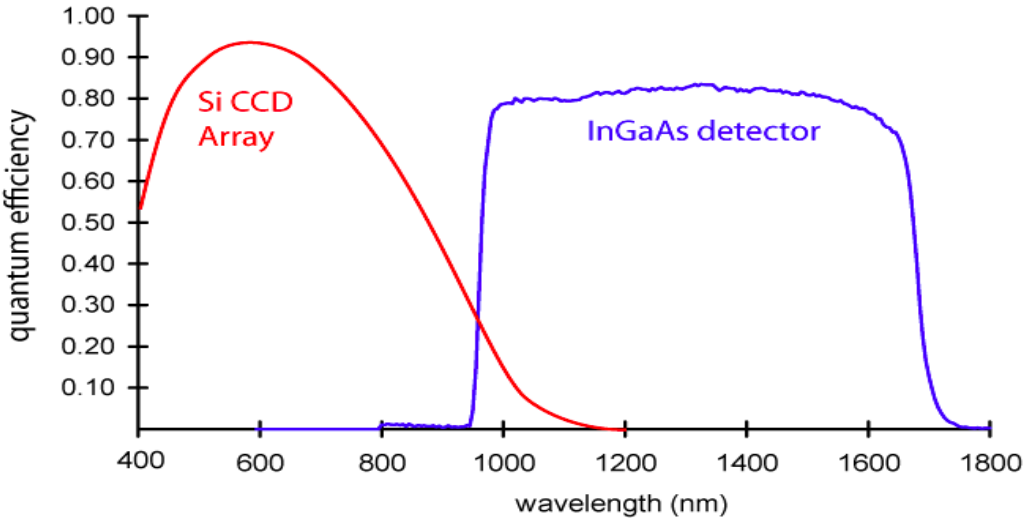

Figure 3.9: Quantum Efficiency in Silicon [48]

The other aspect to consider, is the difference between the band gaps of different semiconductors. Band gaps are either direct or indirect. For an indirect semiconductors, such as Silicon or Germanium, the electron has to pass through an intermediate state in order to transfer momentum in addition to its potential energy to move to the conduction band. However, in direct semiconductors, such as InGaAs, only potential energy is needed in order to move into the conduction band. This has the affect on the light tissue interaction in such way that indirect semiconductors absorb the light less and thereby has to be thicker in order for the light not to directly pass through. To this is though the disadvantage which is its significant cost. Despite poor response of Silicon in the NIR, it offers resolution and low cost, due to commercialization and its abundance in the earth crust [48].

All in all, the tradeoff in Optical Tomography between the visible and NIR range depends on information from the tissue or the sensor. When retrieving information from the tissue the NIR range is more advantageous due to the difference between oxy- and deoxyhemoglobin in the blood. However, for an image sensor the visible range is more beneficial due to silicon quantum efficiency which will offer the best response.

3.3 Reconstruction Methods

Last part to keep in mind when focusing on Optical Tomography are the reconstruction algorithms. In order to fully figure out the incoming data onto the sensor a reconstruction algorithm is applied to retrieve the full image of the tissue. Here the reconstruction for OCT is described but the OCT system itself and image sensors will be described in detail in Chapter 4.

OCT is a high resolution non-invasive imaging technique and common addition to the system is a digital signal processor (DSP). DSPs process digitized outputs from sensors and in order to obtain high performance, efficient algorithms must be implemented. System architectures need to offer the large processing power while having as low power consumption as possible. Apart from that, system scalability algorithm execution efficiency is important in order to provide real-time processing features. Multi-core systems can be used for such systems as they will offer flexibility and high performance. For OCT algorithm implementation the following steps are

taken in order to create an image from the recorded data of the sensors [49], see Figure 3.10.

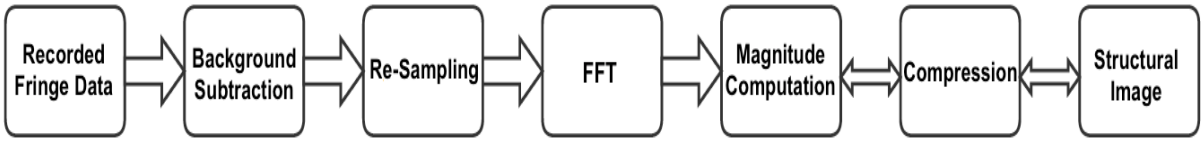

Figure 3.10: Reconstruction Signal Processing Chain in OCT systems [49]

From the sensors recorded fringe data is retrieved. The first step is the background subtraction. By subtracting the background from acquired data the DC component of the signal, caused by the reflectance of the reference arm, can be eliminated, see Chapter 4. When applying a Fast Fourier Transformation (FFT) algorithm onto the data, the spectrum has to be evenly sampled in the frequency domain (k-space). So usually a re-sampling technique is applied to the recorded discrete intensities and re-sampled to the linear frequency domain. As the data is linear in the frequency domain, FFT can be applied and the axial scan can be reconstructed as a function of depth. The output from the FFT is complex and the information from the data is contained in the magnitude of the output data. By using a four term Taylor series approximation, a square root approximation is applied. Due to the function's accuracy the dynamic range has to be compressed for human visualization. This is done by using a non-linear log function [49].

4
Optical Coherence Tomography (OCT)

Optical Coherence Tomography (OCT) is based on low-coherence interferometry which can acquire cross-sectional or 3D images of scattering tissues. Even though OCT was not introduced until the 1990s the interferometry principles and development are based on the Michelson interferometer which was applied in the 1880s in detecting the motion of the earth using light waves [21]. Advantages of OCT include:

- Sub-surface images with near-microscopic resolution
- Direct imaging of tissue morphology
- No preparation of sample or subject
- No ionizing radiation

The disadvantages of OCT imaging is the limitation of being only able to image just below the surface to couple of *millimeters*. This is caused by the scattering property of the tissue. With further depth, the light that escapes without scattering is too small to be detected.

OCT is an imaging technique which has been used both with fiber optics and a photodetector sensor and in free space with image sensors, both CCD and CMOS which offers non-contact imaging. OCT is able to non-invasively image internal structure and is used in many applications both biomedical and non-medical ones. Because of the microscale resolution, safety and low cost it has a wide use in Ophthalmology, Gastroenterology, Cardiology, Urology and Dermatology [49], [50].

In this chapter aspects of Optical Coherence Tomography will be discussed. To begin with, interferometry, which is based on the Michelson interferometer, is explained in Section 4.1. Thereafter, in Section 4.2 OCT techniques and possibilities are presented. Section 4.3 further mentions examples of OCT applications. Finally, results from published literature studies on OCT are explained, compared and discussed in Section 4.4.

4.1 Low-Coherence Interferometry

Interferometry is based on the Michelson interferometer. The basic function of an interferometer is to create and measure interference patterns from a light source. This technique is very well known and is used in a vast variety of applications such as astronomy, quantum mechanics, particle physics and molecular interaction research.

The Michelson interferometer generates an interference between two waves. The interferometer can be seen in Figure 4.1. From the light source (LS), the wave is separated to reference path and sample path by a beam splitter (S). A Compensated plate (C) can be added in order to make sure that the mirrors (M_1 and M_2) have the same optical length at the same distance. M_1 is the reference path with a variable change of placement, represented as d. After back reflection from the mirrors (M_1 and M_2), the waves are sampled together as interference which is the pattern presented through a focusing lens on the detector [51], [52].

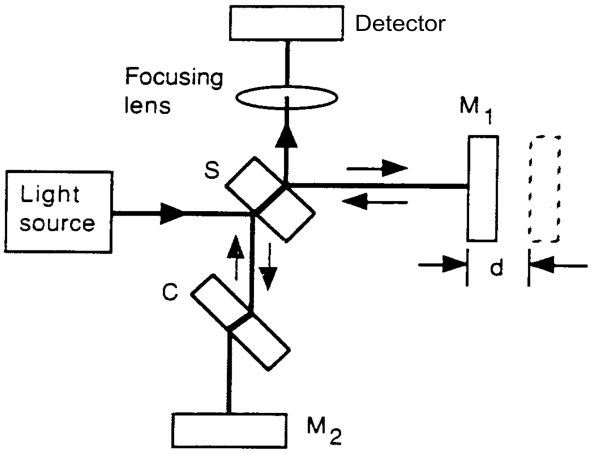

Figure 4.1: Michelsons Interferometer [51]

Interference is a pattern which can be obtained after superposition of waves. Interference waves can be both constructive and destructive. When the waves travel from the same source their total optical path is determined with the difference between the path they have travelled [51]. Lets denote the primary wave as, see Equation 4.1:

$$W_1(x,t) = A_1 \cdot cos(kx - \omega t) \tag{4.1}$$

where A_1 presents the peak amplitude, k the wave number or $2\pi/\lambda$, and ω the angular frequency of the wave or $2\pi f$. Because of their travelling path difference, the second wave function has an added ϕ which is the phase difference between the waves.

$$W_2(x,t) = A_2 \cdot cos(kx - \omega t + \phi) \tag{4.2}$$

When the waves propagate together superposition can be applied. The resulting interference between the waves becomes:

$$W_1 + W_2 = A_1 \cdot cos(kx - \omega t) + A_2 \cdot cos(kx - \omega t + \phi) \tag{4.3}$$

By deriving this equation it can be seen that in case that the phase difference is an even multiple of π it results in constructive interference and for an odd multiply the sum is destructive and

$W_1 + W_2 = 0$.

Coherence is a measure of the correlation between waves which enables interference. Waves which have a constant phase difference but the same frequency and waveform are coherent. Coherence depends on the characteristics of its source. Limiting cases of interference are either constructive or destructive interference. Coherence can be described by temporal and spatial interference. Temporal coherence describes the correlation between phases of a wave at different points in time. It presents how well the wave can interfere with itself or how monochromatic the source is [53]. Important descriptive factor on this property is the coherence length, L_c, which is the distance the wave travels when it is coherent, or from $\tau = 0$ to $\tau = \tau_c$, when the phase difference is not constant anymore. The coherence length can be presented as $L_c = c \cdot \tau_c$. This is related to changes in time with the waves causing them to go out of phase or becoming non-coherent.

Spatial Coherence describes the correlation between phases of a wave at different points in space or transverse to the propagation direction. It presents how uniform the phase of the wave front is or the ability of two points on a wave to interfere. If the correlation between the point decreases so does the interference. Spatial coherence can be calculated via Young interferometer. Figure 4.2 shows the difference between temporal and spatial coherent and incoherent waves.

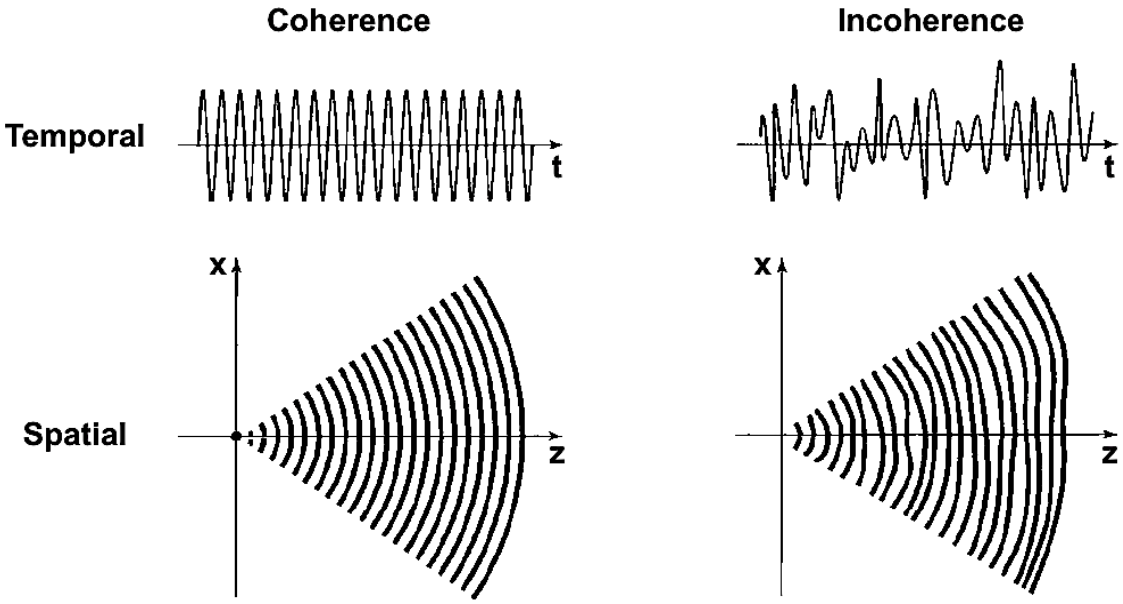

Figure 4.2: Comparison of Temporal and Spatial Coherence [54]

In low coherence tomography, which is used in OCT, the source has a short coherence time, τ_c and therefore a short coherence length. From the Michelson interferometer, the difference in the distance or the optical path difference, d between the sample and the reference mirror defines the resolution and the contrast retrieved, see Figure 4.1. This means as $L_c = c \cdot \tau_c = 2d$, the optical path difference defines the amount of details retrieved. Due to the low coherence length the signal is only retrieved over a limited depth, however by varying d, this can be controlled.

4.1.1 OCT Resolution

An important performance parameter of an OCT system is the resolution retrieved of the subject. The resolution determines how much details of the subject can be seen. Resolution can be measured spatially, temporally and spectrally. The spatial resolution is the ability to distinguish two points in space. This can be divided into axial resolution and lateral resolution. Temporal resolution is the ability to distinguish the changes of the subject in time and can be related to the frame rate. Finally, the spectral resolution is the ability to resolve features and bands in the frequency spectrum. It can be denoted as $\Delta\lambda$ which is the smallest difference in wavelength which can be detected at wavelength λ.

Axial Resolution and Lateral Resolution

Axial resolution or depth is related to both the bandwidth and the wavelength of the light source. Axial resolution depends on the temporal coherence length of the light source, as described before, and can be derived as:

$$L_c \approx \frac{0.44 \cdot \lambda_o^2}{\eta \cdot \Delta\lambda} \tag{4.4}$$

where η is the material refractive index, λ_o is the central wavelength of the source and $\Delta\lambda$ the bandwidth. However, other factors influence the accuracy of this equation, such as, matching reference arm, the source and chromatic dispersion [52]. In optics, dispersion describes how the wave phase velocity depends on the frequency. With the use of a broadband source the resolution can be improved [52].

Lateral resolution is dependent on the optics and presents how well the system can distinguish two points perpendicular to the direction of the wave. This can be derived as:

$$\Delta x = 1.22 \cdot \frac{\lambda}{2\ NA} \tag{4.5}$$

where NA is the numerical aperture of the objective and when NA is increased, the lateral resolution increases. NA describes the range of angles of which the system can gather or emit light. However, at the same time the depth of focus decreases which is the tradeoff [52].

4.2 OCT Techniques

OCT has features which are common to ultrasound whereas light is used instead of sound. At large, the imaging revolves around measuring the magnitude and echo time delay of the reflected light from a sample. OCT techniques can be divided into two groups: Time-Domain OCT (TD-OCT) and Frequency-Domain OCT (FD-OCT). The groups sample an axial scan called A-scan (one-dimensional axial or depth scan) either by measuring the interference pattern in the time domain or by measuring the cross-correlation spectrum which is converted to an A-scan by the Fourier transform in the frequency domain. The TD-OCT, the first proposed OCT scheme, uses a point detector and a scanning arm. However, another type, also proposed in the time domain, is the Linear OCT (L-OCT) which employs a parallel detection scheme. The FD-OCT is either done with a spectrometer, called Spectral-Domain OCT (SD-OCT), or by using a tunable laser, called Swept Source-Domain OCT (SSD-OCT). Figure 4.3 summarizes the four different OCT system implementations.

		Sampling of the A-Scan	
		Sequentially by Point Measurement	Spatially Multiplexed by Parallel Detection
Measured Parameter	Spectrum (Frequency Domain)	Swept Source OCT (Optical Frequency Domain Imaging)	Spectral Domain OCT (Spectral Radar)
	Coherence Function (Time Domain)	Time Domain OCT	Linear OCT

Figure 4.3: OCT System Implementations [55, p.430]

Another implementation which differs from the two grouped domains is the Full-Field OCT (FF-OCT) which is able to capture *en face* images via phase stepping, see Section 4.2.4.

Generally, the set-up of any OCT system has similarities to the one shown in Figure 4.4. The generic OCT system is based on fibre optics but can also be implemented in free space which is presented in examples throughout the thesis. The difference between the set-ups of different techniques are mostly changes concerning the low-coherence source (narrow or broadband source), the reference (fixed, scanning or oscillating) and the detector (photodetector, CCD or CMOS sensor).

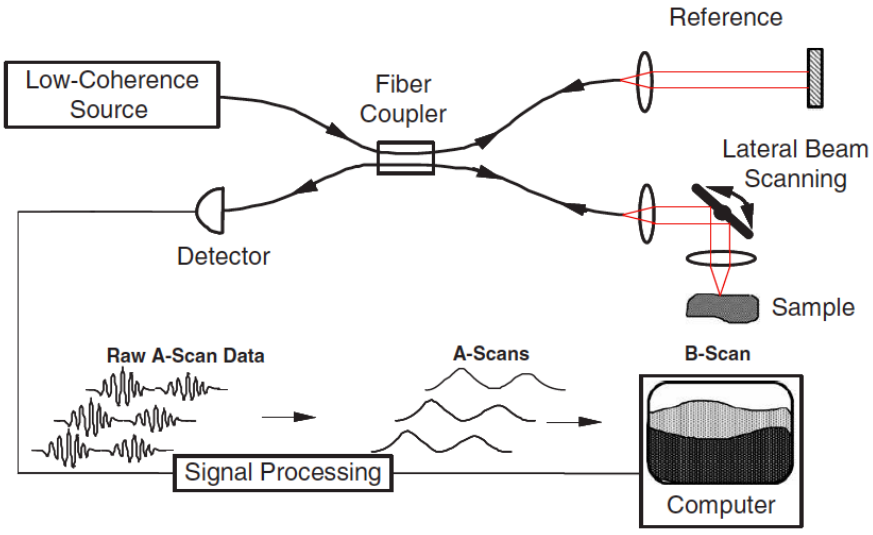

Figure 4.4: Generic Fibre Based OCT System [55, p.48]

In short, as the source is directed to the system, the fiber coupler splits the optical power between the sample and reference. The light in the reference path interferes with a reference delay. The light in the sample path is focused onto a specific sample. On return, the light from both arms are mixed upon return at the fibre coupler and this interference is detected by a detector. The detected signals are processed into an A-scan which represents the depth resolved reflectivity.

Multiple scans can then be reconstructed into a B-scan or a two-dimensional cross-sectional image.

4.2.1 Time-Domain OCT (TD-OCT)

The conventional and the first developed OCT systems used the Time-Domain OCT (TD-OCT) technique. The system depends on an interference pattern acquired by a single point scanning with the movement of the reference, a reference mirror. The system can be seen in Figure 4.4. By using a low coherence light, the pattern is acquired by moving a reference mirror linearly. The low-coherence source of the system is a broadband and continuous wave source, such as an SLD. The reference path length is changed to match the multiple optical paths which are caused by the reflections inside the subject. By controlling the movement of the reference mirror, the depth of the subject is imaged [52]. In order for the waves from different paths (reference or sample arm) to interfere, the paths have to match.

From the source, the wave is separated by a fiber coupler, reflects upon the sample and reference mirror and then re-unites at a photodetector. The signal consists of a DC term and an interference term which contains the sample information. The DC term can be mostly removed with a dual balanced approach which includes another photodetector [52]. The photodetector detects the average power intensity over a certain range of frequencies, see Equation 4.6:

$$P_{detector}(k) = P_{ref}(k) + P_{sig}(k) + 2\sqrt{P_{sig}(k)\ P_{ref}(k)}\ cos\ (2k\ (x_r - x_s)) \tag{4.6}$$

where $P_{ref}(k)$ and $P_{sig}(k)$ are the collected reference and subject signal power at a given wave number, k [56]. The $(x_r - x_s)$ is the difference in the reference arm length and the distance to the subject's back scattering. By integrating over the light source spectrum the total power detected can be derived, see Equation 4.7:

$$P_{detector}(k) = P_{ref}(k) + P_{sig}(k) + 2\sqrt{P_{sig}(k)\ P_{ref}(k)}\ sinc\ (\frac{\pi\ (x_r - x_s)}{L_c})\ cos\ (2k\ (x_r - x_s)) \tag{4.7}$$

where $L_c = \frac{\pi}{\Delta k}$ is the coherence length. This means that optimally the coherence length needs to be as small as possible and since it depends on the spectral bandwidth, the bandwidth is desired to be as broad as possible in order to detect more power. The sensitivity from the system can be derived with the use of the total scan time collecting signals, $\frac{L_c}{x_{depth}} \cdot T$. By comparing the number of signal photons to the noise photon count, within the total scan time, the SNR is derived [56], see Equation 4.8:

$$SNR_{TD-OCT} = 10\ log\ (\frac{Signal}{Noise}) = 10\ log\ (4P_{sig}\ \frac{L_c T}{x_{depth}}\ \frac{\varepsilon}{\hbar v}) \tag{4.8}$$

where ε is the quantum efficiency of the detector, x_{depth} is the depth range desired for probing, T is the total scan time and $\hbar v$ is the photon energy. Sensitivity thereby depends inversely on the source bandwidth.

Advantages and Disadvantages

One of the biggest disadvantages for the system is that for each axial scan the reference mirror has to move one cycle. This limits the speed of image acquisition. Another disadvantage is related to the time a TD-OCT system is able to collect data as it is limited by the coherence length and x_{depth}. This means that the detection is only able to detect the photons during this limited period which limits the ability to collect the whole signal and diminishes the signal

sensitivity. But both FD-OCT and FF-OCT techniques are able to make full use of the signals or the backscattered photons, as they are not limited by L_c, which results in higher SNR [56].

The advantage of a TD-OCT system is that it is capable of removing the DC component of the signal and only pass through the interference modulation. In SD-OCT with the use of a CCD, removing the DC component is complex. The DC component can affect the dynamic range.

4.2.2 Linear OCT (L-OCT)

An overview of the technique of L-OCT can be seen in Figure 4.5. The interference pattern is measured by a line or an array detector. This is done by expanding the sample and reference beam under certain phase onto the detector where they are superposed as the sample intensity and reference intensity.

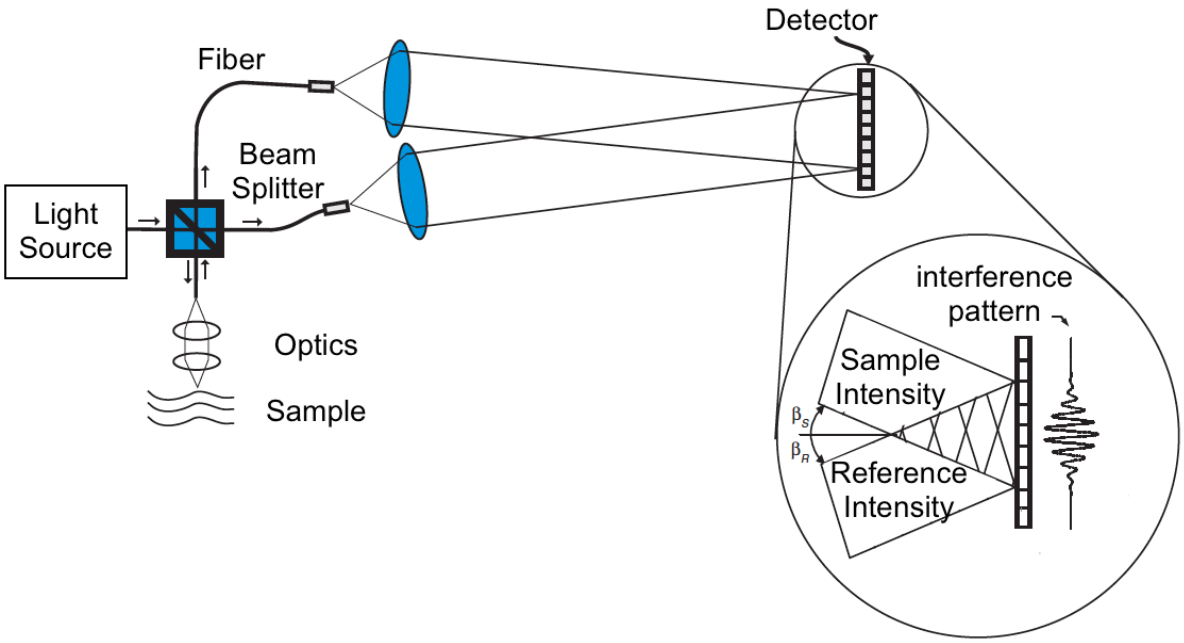

Figure 4.5: L-OCT System [55, p.432]

Advantages and Disadvantages

The largest advantage of the L-OCT is its ability to apply a parallel detection scheme and eliminate the moving part of the general TD-OCT system. Further advantages include a simple design and lower cost, fast acquisition speed and stable phase detection. Nevertheless, the system is sensitive to movements and experiences some signal losses at the edges of the detector due to the system structure, for example due to the fibers and the way the light is pointed towards the sensor. While the FD-OCT offers higher sensitivity and SNR, the L-OCT has the advantages of simpler signal evaluation without Fourier transform and set-up. Overall the L-OCT has similar image quality compared to TD-OCT and therefore the technique will not be described in detail.

4.2.3 Frequency-Domain OCT (FD-OCT)

Frequency-Domain OCT is depended on detecting an interferometric signal as a function of optical frequencies. Two types of systems are based on this technique, the Spectral-Domain

OCT and the Swept Source-Domain OCT. While the structure of these systems is built up in a similar manner with a fixed reference, the light sources are different. Advancements in frequency domain imaging enabled an increase in imaging speed. By operating at higher speeds, higher number of axial scans or transverse pixels per image can be retrieved which enables higher resolution images.

Spectral-Domain OCT (SD-OCT)

Spectral-Domain OCT (SD-OCT), also known as Fourier-Domain OCT (FD-OCT), performs detection on the interference spectrum with the use of spectrometer and a line scan camera. A spectrometer is an instrument capable of splitting light or spectrum into separate wavelengths. From an optical spectrometer the light intensity can be presented as a function of wavelengths or frequency.

A generic SD-OCT system set-up is shown in Figure 4.6. The detection works as follows. A broadband low coherent light source is split into two beams, one that travels towards a fixed reference and the other one towards the sample. The light is then reflected back from the two arms. The beam that is reflected back from the sample contains information of the internal structures of the sample whereas the light reacts differently to different structures at different depths. Then in order for interference to occur between the reference and sample beams, a certain time delay, determined by the optical paths and sample depth to be imaged, is implemented in the system as ΔL. The interference pattern is detected by the spectrometer which splits the light into spectral information. As the interference beam gets dispersed by a diffraction grating, wavelength components are detected by a detector array such as a line camera array [49]. The pattern is converted to axial information by Fourier transformation. This type of detection is a almost 100 times faster than the TD-OCT imaging speed.

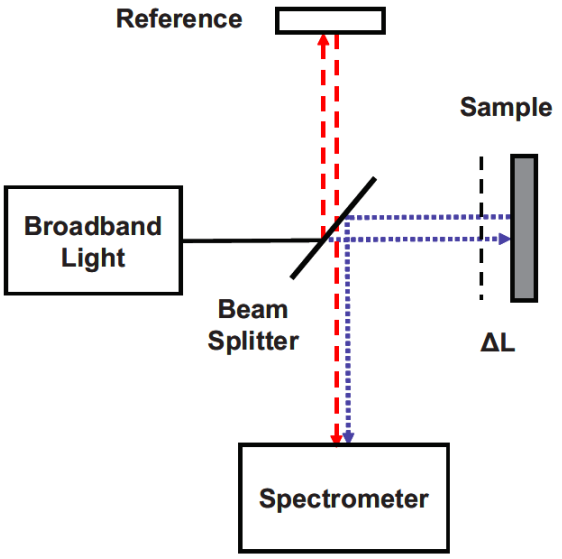

Figure 4.6: Spectral-Domain OCT System Set-Up [55, p.32]

Swept Source-Domain OCT (SSD-OCT)

SSD-OCT detection uses an interferometer with a narrow bandwidth light source where the frequency is swept in time. Developments started in the late 1990s but were limited by the

laser technology at the time. With new technology, high imaging speed can be reached at an increased resolution.

A generic SSD-OCT system set-up is shown in Figure 4.7. The detection works similarly as described for SD-OCT. A narrow bandwidth frequency swept light source splits towards the fixed reference and the sample. The reference beam has a fixed time delay, but depending on the depth of the sample and the sample beam, has a certain offset determined by the path length difference. Now, due to the sweep of the light frequency in time certain frequency offset is created. When the light beams interfere, a certain "beat" frequency is created at the frequency given by the offset. The "beat" signal is measured by a photodetector over a single frequency sweep and with Fourier transform results in an axial scan.

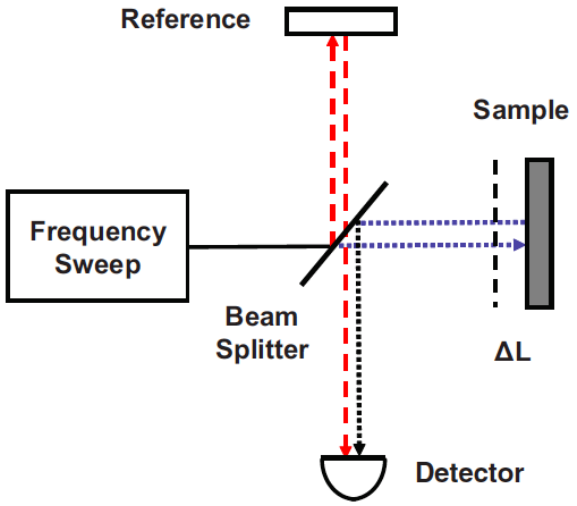

Figure 4.7: Swept Source-Domain OCT System Set-Up [55, p.36]

Advantages and Disadvantages

First, the sensitivity of the frequency domain systems can be obtained as, see Equation 4.9:

$$SNR_{SD-OCT} = 10\ log\ (\frac{Signal}{Noise}) = 10\ log\ (4\ P_{sig}\ T\ \frac{\varepsilon}{\hbar v}) \tag{4.9}$$

By comparing this to the sensitivity of the TD-OCT, the frequency domain OCT systems are more sensitive and are able to collect signals from all depths during the acquisition time [56]. Thereby the first advantage of the frequency domain techniques is that it essentially measures all the echoes of light simultaneously instead of sequentially as done in the time domain. Thereby enabling higher speed and sensitivity [55], [56].

Disadvantages of the system include that the instrumentation for acquiring the spectral interferogram always has limited spectral resolution. For SD-OCT the limitation is caused by the resolution of the spectrometer while for SSD-OCT, the resolution is limited by the lineshape of the swept laser. The cost of the light source for SSD-OCT is higher.

Note that both time domain and frequency domain OCT systems are limited by shot noise and the shot noise variance in a detector can be given by, see Equation 4.10:

$$\sigma_{sh}^2 = 2eIB \tag{4.10}$$

where e is the electron charge, I is the mean photodetector current and B is the detection bandwidth [55]. Based on further analysis, the sensitivities of the systems can be given as, see Table 4.1, where it is normalized to the sample arm instantaneous power S_{TDOCT} and detection bandwidth B_{TDOCT} used in TD-OCT. The ρ is the responsitivity of the detector and e is the electric charge.

	TD-OCT	**SD-OCT**	**SSD-OCT**
SNR	$\frac{\rho S_{TDOCT} R_S}{2eB_{TDOCT}}$	$\frac{\rho S_{TDOCT} R_S}{2eB_{TDOCT}} \frac{M}{2}$	$\frac{\rho S_{TDOCT} R_S}{2eB_{TDOCT}} \frac{M}{2}$

Table 4.1: SNR Comparison by Normalization to TD-OCT

From this it is shown that the improvement of the SNR in the frequency domain is better by a factor M. However, at the same time the SNR improvement is decreased by a factor two due to redundant data.

Now more specific disadvantages on SD-OCT included the limitation of the detection efficiency and resolution in the state-of-the-art spectrometers. However, the advantages allow for higher imaging speed, high SNR and good resolution in retinal imaging. Towards the SSD-OCT, the system uses a single-element photodetectors which eliminates the need for spectrometer and a line scan camera. Other advantages include a reduced excess noise which is because at each wavenumber k, the output of the swept source is a narrowband laser with much smaller noise than that of the broadband source [55, p. 10].

4.2.4 Full-Field OCT (FF-OCT)

From the point-by-point scanning in the time-domain and spectrometric measurements in the frequency-domain the Full-Field OCT (FF-OCT) is proposed. FF-OCT produces images orthogonal to the optical axis without a scanning beam where the entire field of the image is illuminated. FF-OCT is able to take two-dimensional images directly using image sensors with the use of a simple white light source, such as a tungsten-halogen lamp. However, in order to retrieve the depth of the object to be imaged, it needs to be moved in an axial direction. By reconstructing the images taken step-by-step a three-dimensional image is recorded. FF-OCT is capable of offering lateral and axial resolution of around 1 μm [55].

The set-up arrangement of the technique can be seen in Figure 4.8. From the Halogen Köhler illuminator a homogeneous illumination to the field is applied. The beam splitter (BS) splits the source towards the object/sample and a reference mirror aimed through a microscope objective (MO). Interference only occurs if the optical paths are the same. This is adjusted with motorized axial translation. Finally, the interferometric images are acquired by a camera where by using a phase shifting method phase is changed between each image acquisition. This is done with a piezoelectric translation stage (PZT). The final image is then a combination of the interferometric images acquired.

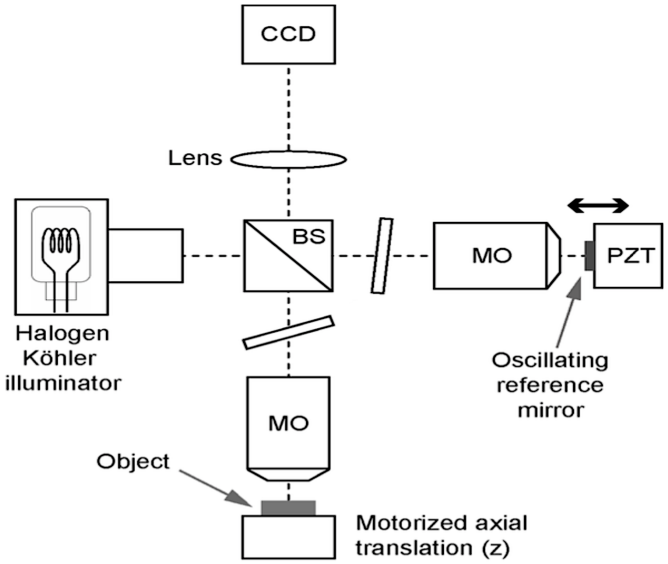

Figure 4.8: Set-Up of a Full-Field OCT [57]

Advantages and Disadvantages

Overall the major advantages of using the FF-OCT technique is the ability to apply parallel detection over all of the pixels and thereby having the capability of data acquisition at video rate. Other advantages include the possibility of using a simple low spatial coherence light source, such as the tungsten-halogen lamp, which also has low temporal coherence providing high axial resolution. Further it works without light beam scanning and reference optical delay scanning.

The performance of the technique depends a lot on the detection sensitivity and thereby the full well capacity. By using the example above with the CCD image sensor this can be seen. When the illumination flux is so that CCD pixel wells are close to the saturation value denoted as ξ_{sat}. With derivation and the assumption that the minimum detectable reflectivity corresponds to an SNR of 1, the smallest reflectivity (R_{min}) is, see Equation 4.11 [55]:

$$R_{min} = \left(\frac{\pi}{8\sqrt{2}\,\Gamma}\right)^2 \frac{(R_{ref} + R_{inc})^2}{N\xi_{sat}R_{ref}} \tag{4.11}$$

where R_{ref} and R_{inc} is the reflectivity from the reference arm and the reflectivity from unwanted reflections, respectively. The other factors are related to the number of times the flux is integrated, see further in [55]. Thereby, the relation of the full well capacity to the detectable reflectivity and detection sensitivity has been shown. Multiple methods exist in order to increase pixel wells but will not be discussed for the time being.

Another advantage of the FF-OCT is that the detection sensitivity does not depend on the source bandwidth in the same way as the TD-OCT does due to the phase stepping technique. However, disadvantages include that motion during image acquisition can induce changes in the optical phase, causing blur or worsened contrast. This happens because of the time it takes to collect the whole image. However, some image distortion caused by motion can be corrected via signal processing algorithms [55].

This method has shown high performance *ex vivo*. Nevertheless, due to the object motion *in vivo* is more challenging.

4.2.5 Comparison between the Techniques

To summarize, TD-OCT collects axial data point-by-point with the use of scanning arms. FD-OCT overcame the scanning arms by collecting spectral data and with Fourier transformation changing it to axial data. Finally, FF-OCT collect *en face* (B-scan images) with a phase shift method applied with oscillation of the reference mirror. The data collected can be reconstructed into three-dimensional images. At the same time the TD-OCT detects the light intensity in time while the FD-OCT detects the light intensity for each optical frequency. Finally, the FF-OCT detects the light in space. Comparison of different OCT techniques and systems have been summarized in Table 4.2.

Table 4.2: Comparison between OCT Techniques

Type	**TD-OCT**	**L-OCT**	**SD-OCT**	**SSD-OCT**	**FF-OCT**
System	Complex	Simple	Complex	Simple	Simple
Light Source	Broadband	Broadband	Broadband	Narrowband	Broadband
Speed	Slow	Fast	Fast	Fast	Very Fast
Axial Resolution	Average	Average	High	High	Very High
Cost	Low	Low	High	High	Low

4.3 OCT System Examples

Previously, different OCT techniques were explained with the methods they use to retrieve the data from an interferometer system, such as in the time or the frequency domain. As mentioned before both fibre optic photodetector sensors and image sensors (CCD and CMOS) can be used for retrieval of data. In order to form some base on the performance of OCT systems which apply detection with fibre optic sensors or with free space CCD sensors, two literature's are presented.

4.3.1 Fibre Optic OCT System

An OCT system with fibre optics works similar to the interferometry concept previously explained. One of the arms is focused onto the reference mirror and the second one is focused onto the sample. From the SLD diode, as an example, the light is conducted to a fibre coupler. The fibre coupler distributes the light to two outputs which is dependent on the wavelength and the polarization of the light. The SLD diode is used in order to retrieve higher resolution because of the low coherence. The system is presented in Figure 4.9 and is based on the TD-OCT technique.

An important function of the reference mirror (scanning mirror) in this set-up is to vary the length of its reference arm in order to retrieve data on the reflectance from the sample. Then with the combination of the reflectance from both the sample and the arm, an one dimensional reflectance scan of the sample, called A-scan can be retrieved. In this set-up the galvanometer is used to vary the length of the arm of the reference mirror as it is capable of acting as an actuator.

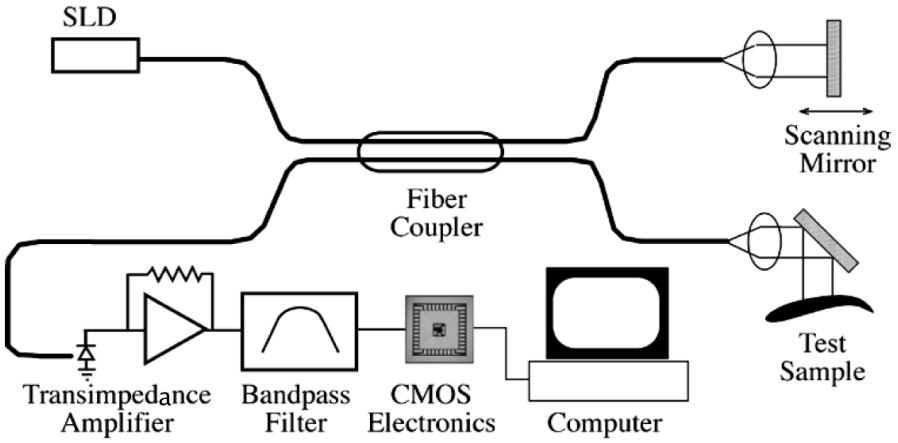

Figure 4.9: Example of an OCT Fibre Optic System [58]

The system has added image processing electronics [58]. With the moving mirror a Doppler oscillation interferes with the signal because of the coherence effects and depends on the velocity of the mirror (v) and the wavelength of operation (λ) [58], see Equation 4.12:

$$f_D = 2\,\frac{v}{\lambda} \tag{4.12}$$

The signal is fed into the signal processing circuit after being sensed by the photodetector and transimpedance amplifier. There, the Doppler frequency is removed and the signal is shifted to lower bandwidth. The resulting signal contains the A-scan information of the depth of the subject. The advantages of this structure is low cost, small size and chip integration by using the CMOS circuitry for the detection. Also the CMOS signal processing circuitry were added to improve the fibre optic system [50].

Another example of a fibre optic system has been presented here [59] which achieved the lateral resolution of 12 μm and axial resolution of 10 μm with the use of an SLD source.

4.3.2 CCD OCT System

In Figure 4.10 a CCD image sensor-based FF-OCT system is presented. With the use of a CCD camera parallel detection can be applied. The LED source is polarized and by a beam splitter separated into two orthogonal waves. One of them is focused onto a mirror and the other one onto a sample. By using a polarizing beam splitter the measurements provide values of amplitudes of orthogonal components by using a photoelastic modulator and an analyzer. Photoelastic modulator is used to modulate the polarization of the light. By introducing periodic phase shift, with the addition of the analyzer the interferential part of the data is only modulated without the incoherent background. The detector used is a CCD image sensor, 256 x 256 pixels, (Leica, Olympus BX60) with the dynamic range of 58 dB [60].

Resolution retrieved by this system is 2 μm and 8 μm for lateral and axial resolution, respectively. Lateral resolution is limited by the optics and the pixels of the detector. In order to improve the axial resolution further source with even shorter coherence length may be applied [61].

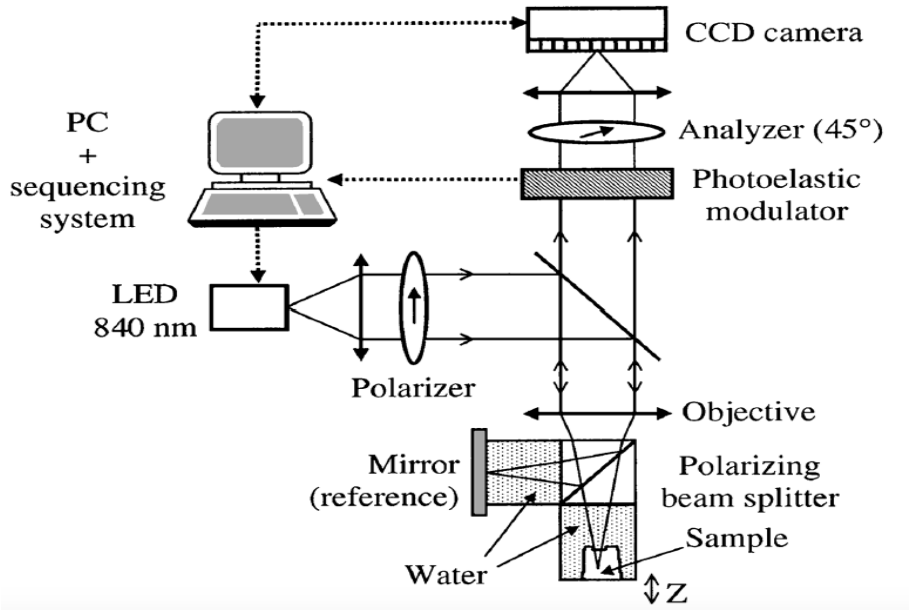

Figure 4.10: Example of an OCT CCD Image Sensor System [61]

4.4 OCT Literature Study

As mentioned before, OCT systems are known for their use with both fibre optic sensors and CCD image sensors. Fibre optic sensors have limitations in acquisition. Therefore new approaches have been developed with the intention of acquiring a high speed device which can be used in *in vivo* imaging. By applying the use of CCD camera the fibre optics are eliminated [61]. However, using CCD in OCT applications has certain disadvantages. Firstly, the integration time is too long compared to the modulation period of the interferometric signal, this is a limiting factor for the scanning speed. Secondly, the dynamic range is limited by the DC light level which is inherent in the signal that reaches the detector. This makes CCD unsuitable for high speed OCT [62].

In this section research papers on Optical Coherence Tomography (OCT) using CMOS image sensors are presented. As CMOS image sensors are able to offer many different options in their architecture and pixel design, their potential has been studied to see if they are able to overcome CCD disadvantages. Below, a couple of published articles on OCT CMOS image sensors are discussed where for each study system explanation, pixel structure concepts and results are listed.

4.4.1 2D Smart Detector Array

The OCT smart detector array presented by Bourquin and Seitz, published in 2000, showed one of the first prospects of CMOS image sensors in OCT [62]. The goal of the study was to improve the frame rate known in fibre optic sensors. Fibre optic sensors have low frame rate due to low scan speed, as only one pixel per unit time can be scanned. In order to improve the frame rate a parallel detection scheme was proposed. CCD image sensors are able to apply parallel detection but are forced to do signal processing off-chip. More disadvantages follow, such as, the modulation frequency has to be known, integration time is high and in order to improve the SNR averaging has to be applied which decreases the speed. In addition, the DC light level limits the dynamic range [63]. By proposing a CMOS smart detector array some

of these disadvantages were challenged. The development towards a fast 3D image acquisition in internal imaging, highly desired in the medical field, was the goal. This study was built on previous development of a former image sensor, also designed by Bourquin [64].

System Description

The system presented in the paper can be seen in Figure 4.11 [62]. This shows the interferometry structure with an SLD source, with 1.95 mW power, central wavelength (λ_c) = 850 nm, FWHM ($\Delta\lambda$) = 20 nm, Beam splitter (BS), Microscope objectives ($L1$, 4.6 mm focal length, $L2$, 7.2 mm focal length), Achromatic lenses ($L3$, $L4$, 80 mm focal length, $L5$, 60 mm focal length), Aperture stop (AS), Sample (S), Reference Mirror (RM), the detector array and read-out circuitry.

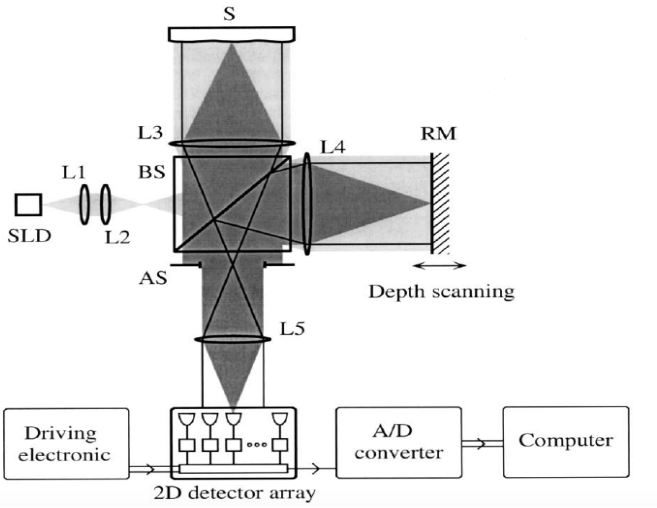

Figure 4.11: The OCT CMOS Smart Detector System Set-Up [62]

The system works as follows. From the SLD a spatial coherent light is directed onto the beam splitter with the use of $L1$ and $L2$. The 50/50 non-polarizing beam splitter directs the light into the RM and onto the sample, S. The RM is moved (with the speed of $v = 1.6\ mm/s$) in order to detect the depth as this is a TD-OCT system. With the use of lenses $L3$ and $L4$, the light power reaching the sample was around 760 μW. Finally, $L5$ was adjusted for magnification factor of 1.3. In order to receive an interference at the detector the difference in path length between the RM and the sample have to be within the coherence length of the light source. By uniform depth scanning of the RM, the shift in the frequency resulted in the Doppler frequency of $f_D = 2v/\lambda = 3.7$ kHz. By using the AS, the fringe contrast could be adjusted.

Pixel Structure

Inside the 2D detector array, 58 x 58 pixels, each pixel includes a photodiode, an amplifier with a feedback to control the current source, a rectifier and a low pass filter, see Figure 4.12.

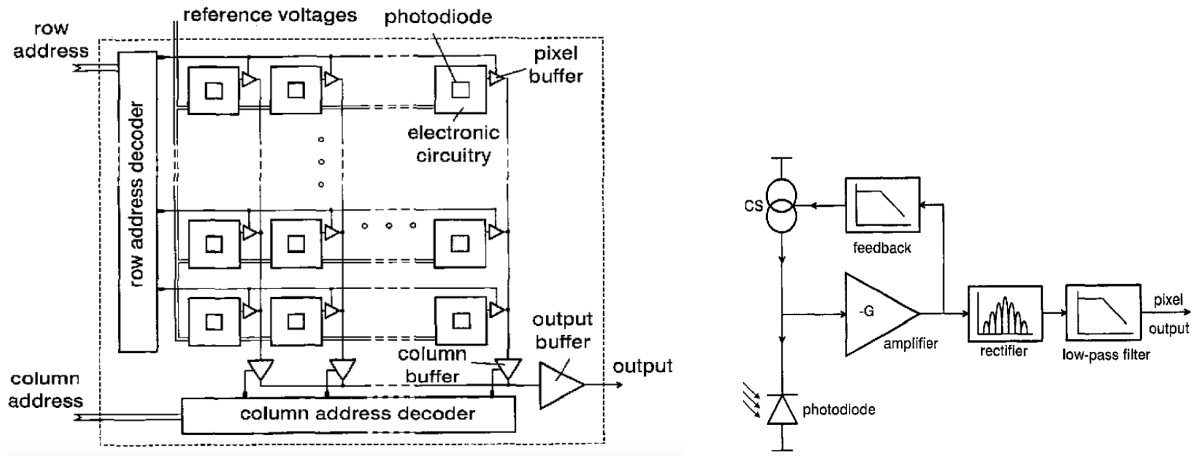

(a) Detector Array

(b) Block Diagram of the Pixel

Figure 4.12: Photodetector and Pixel Structure [63]

To start with the detector array, Figure 4.12 [a], it includes the pixels, with pitch of 110 μm, reference voltages, buffers and row and column address blocks. With the use of row and column address decoders, the pixel modulation amplitude is directly readout. The data from the array is then digitized with a 12 bit ADC. The reference voltages are used to reset the pixel.

The pixel can be seen in Figure 4.12 [b], with a 35 μm x 35 μm photodiode. Inside each pixel the signal from the photodiode is amplified and goes through signal processing steps in order to remove the DC component. This is done by assessing the envelope of the interference signal modulation. The signal demodulation is performed in parallel without signal sampling and read from one pixel at a time. As the signal is detected at the photodiode and converted into current, the voltage controlled current source (CS) is subtracted and the difference is amplified with a transimpedance amplifier, from current to voltage output. The feedback loop, which uses an amplified signal to control the current source, biases the amplifier. The feedback loop controls the frequency range by introducing a low pass filter. If the frequency is below the corner frequency, -3dB, the feedback acts as a short circuit. However, if the frequency is larger than the corner frequency the feedback acts as open and the output is amplified with the gain G. The output is then rectified to a positive value and filtered with a low pass filter where its corner frequency is adjusted to give the integrated signal.

Results

The design of the 2D smart detector included only few pixels and thereby resulted in low resolution. The photodiode in each pixel consumed only 10 % of the total area, thus a large part of the signal is wasted. The resulting frame rate is low or 6 fps and the limiting factor was due to the ADC. The maximum output voltage from the sensor was around 850 mV and the minimum noise 1.2 mV resulted in the dynamic range of 57 dB. The shot noise contribution to the value was calculated by, see Equation 4.13:

$$\sigma_{i,sn} = \sqrt{2eBI} \tag{4.13}$$

where σ is the standard deviation, I is the current through the photodiode and B is the bandwidth. The total noise power and the shot noise measured at 142 pW and 67 pW, respectively.

The results from the system simulation alongside pixel sensor parameters are summarized in Table 4.3.

Table 4.3: Specifications and Results of the 2D Smart Detector Array

Sensor	**CMOS Detector Array**
Resolution	58 x 58 pixels
Pixel Size	110 x 110 μm^2
Photodiode	35 x 35 μm^2
Fill Factor	10 %
Frame rate	6 fps
Dynamic range	57 dB
Min. RMS Noise	1.2 mV
Axial Resolution	16 μm
Lateral Resolution	Unreported

From this first generation of CMOS imager use in OCT, multiple improvements could be added to obtain better specifications and results. The first goal would be to increase the resolution with more pixels. In [62] 2 μm CMOS technology was used, which today is relatively large. This may be decreased to 0.9 μm technology for example. This would allow for more pixels in the same area or additional functions inside each pixel. Another improvement on the detector would be in increasing the fill factor. As for a limitation in area, a microlens array could be attached to focus the light towards the photodiode, as in this design there were none. Another suggestion, for an increase in frame rate, would be to add more readout locations which would increase the readout speed.

Finally, an improvement could be done on the FWC and the shot noise. By increasing the FWC which is the amount of electrons that can be stored in a pixel and minimizing the shot noise further, the SNR and the DR could be increased. The well stores charges which are collected during an integrative process. The size of the capacity depends on photodiode and possibly an additional capacitor. The capacitance of the photodiode depends on the doping which is set by the technology process. This metric is closely related to the dynamic range. Larger well capacity has larger capacitance in the photodiode and smaller voltage change occurs with collection of a new charge. From Equation 2.2 it can be seen that the factors which determine the size of the well is the diode capacitance, the electron charge, the initial and maximum voltage.

4.4.2 CMOS-DSP Camera

A study published in 2006 showed an example of an OCT system where its detector is a commercial CMOS-DSP camera (iMVS-155, AKAtech SA, Switzerland [65]). The advantage of this commercial sensor is the feature of a random pixel access. This possibility allows for an increase of readout speed by choosing a Region Of Interest (ROI). However, the random access comes at a tradeoff between speed, image resolution and size. For video imaging, such as in industrial applications, random access is a more advantageous option as the camera has the possibility of optimizing the frame rate. This OCT system was used for researching rough metallic surfaces.

System Description

In Figure 4.13, the CMOS image sensor OCT system is presented. With the SLD light source the wave is pointed through a convex lens (L1) onto a beam splitter (BS) which then travels

to a reference mirror on one hand and to the sample (SMP) on the other hand. The camera is focused on the sample with the camera objective (CO). In this system a polarizer (POL) and a rough reference surface is added to maximize SNR for higher visibility and higher AC/DC ratio of the light intensity components. Also by off-centering the camera, the parasitic DC light from the beam splitter, can be reduced [61].

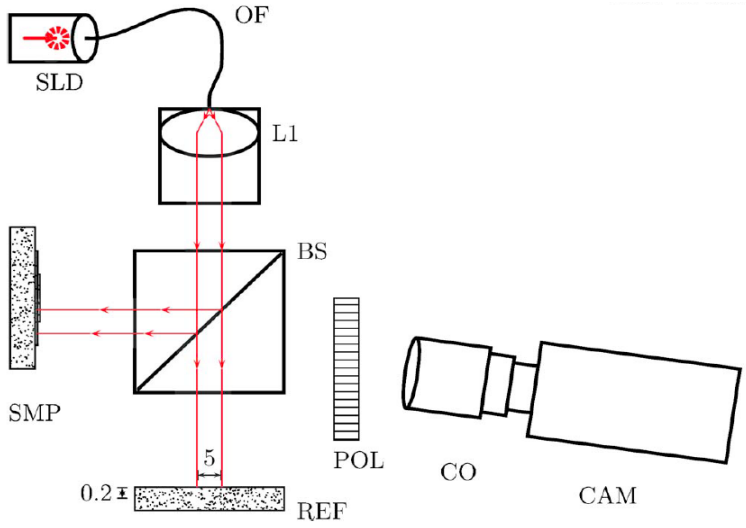

Figure 4.13: OCT CMOS-DSP Image Sensor System [66]

The camera uses a 1024 x 1024 pixels CMOS sensor, fabricated with 2 μm CMOS process, which has a logarithmic voltage response to light intensity as follows, see Equation 4.14:

$$V = m \cdot log_{10} \frac{I}{I_0} \tag{4.14}$$

where I is the light intensity on the pixel, I_0 the initial light intensity and m is a constant.

The camera has a random addressable CMOS image sensor where ROI imaging is enabled. For a fully random readout, an asynchronous circuit for both driving and reading the sensor is applied. Asynchronous circuit operates without clock signals and changes only once the inputs have been received. Thereby their behavior is close to instantaneous which results in the advantage of faster frame rates. However, the disadvantages are due to the way of propagation, which could cause a delay, as well as possible race conditions, which could cause an incorrect state. By using random addressable pixels, data can be accessed and read at any moment in time. Nevertheless, the price to pay for a high frame rate is either with the image resolution or the image size [67].

Pixel Structure

The proposed pixel structure produces a continuous signal proportional to the light intensity. The sensor response is logarithmic due to the photocurrent flow through the logarithmic resistive load. The resistive load is implemented as a diode connected transistor, see Figure 4.14.

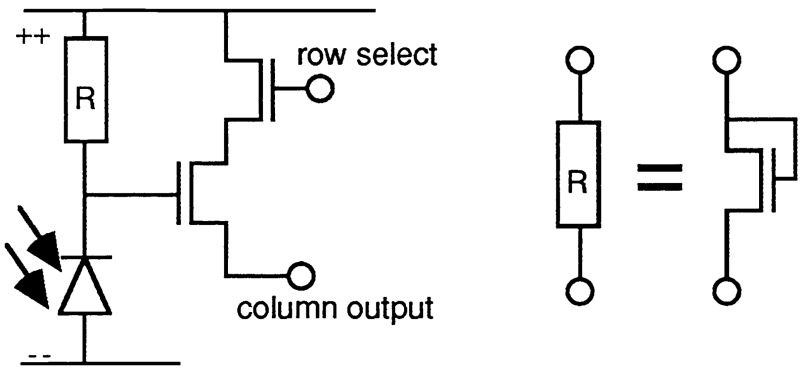

Figure 4.14: Implementation of the Pixel [67]

From the photodiode, light is converted into a photocurrent which flows through the load transistor, R. With a photocurrent ranging from femto to nano Ampere the transistor operates in the weak inversion, see further in Chapter 7. The voltage over the load is then buffered with a source follower. Row select determines if the pixel is read. The circuit load and capacitance define the pixel response time, τ, which depends on the light intensity. The relation between the two, retrieved from a data sheet of the DSP camera (iMVS-155), can be seen in Figure 4.15.

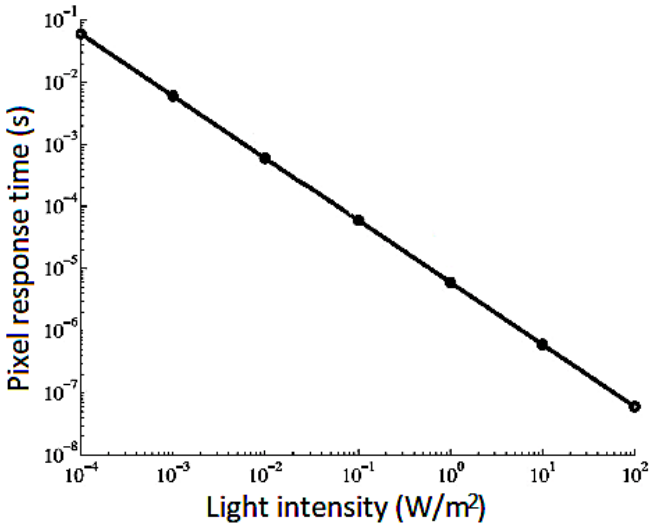

Figure 4.15: Pixel Response Time versus Light Intensity [66]

As the light intensity increases, the lower the response time is. Nevertheless, under very low illumination, this response time has to be kept in mind. In case the frequency of the optical carrier is greater than the cutoff frequency of the pixel at certain intensity the signal gets attenuated and the SNR reduced [66]. A tradeoff between light intensity, scan speed and SNR will be up for debate.

The advantage of a logarithmic pixel is the possibility to sense light intensity over a wide range and for the CMOS-DSP camera upto 120 dB. However, due to its light intensity response defining SNR becomes difficult. In order to measure such quality, Equation 4.15 has been derived:

$$\frac{S}{N} = \frac{\Phi_{signal} \cdot \frac{\delta V_{signal}}{\delta \Phi_{signal}}}{V_{noise}} \tag{4.15}$$

where Φ_{signal} is the illumination level, V_{signal} is the output signal and V_{noise} is the noise level [68].

Results

For the results of this study a particular ROI was chosen of 64 x 30 pixels. By the choice of fewer pixels to read out, the readout is faster or the frame rate but at the same time the resolution is low. Thereby the tradeoff lies in that the frame rate was optimized on the cost of the resolution. In this application the frame rate was of interest and the resolution not a vital parameter. The main reason for presenting this study in this thesis was to show a method of optimizing the frame rate of an OCT system as well as the use of commercialized devices. The results from the system simulation alongside the pixel sensor parameters are summarized in Table 4.4.

Table 4.4: Specifications and Results of the CMOS-DSP Camera for the ROI

Sensor	**CMOS Detector Array**
Resolution	1024 x 1024 pixels
Resolution of ROI	64 x 30 pixels
Pixel size	8 x 8 μm^2
Fill Factor	70 %
Frame rate for ROI	235 fps
Dynamic Range	Unreported
Axial Resolution	22 μm
Lateral Resolution	14 μm

The advantage of this study is the use of this off-the-shelf CMOS-DSP camera which reduced the cost of an OCT system. The random addressable pixel allows for a higher frame rate. However, even though the electronic scanning with the use of a reference arm is eliminated, the disadvantage is that the SNR does not change with increasing source power due to the logarithmic signal response, see Figure 4.16.

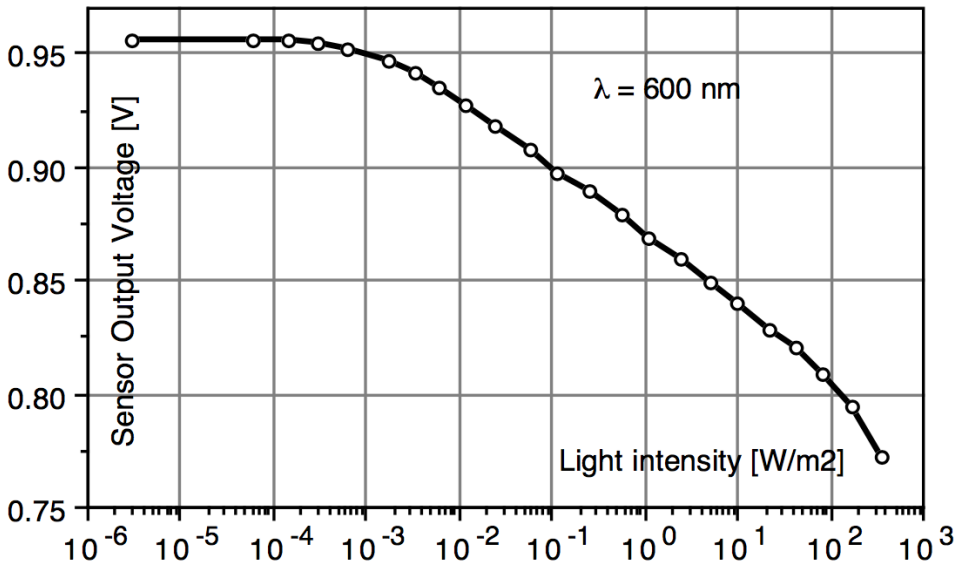

Figure 4.16: Logarithmic Light-to-Voltage Response of the Pixel [67]

4.4.3 Global Shutter CMOS Image Sensor

CMOSIS, which is an image sensor company in Belgium, published their 700 fps 2 Mega Pixel global shutter image sensor with 2 Me- full well charge in 2015 as part of a European Union funded project called CAReIOCA [57]. The goal of this project was to eliminate time consuming procedures when diagnosing tissues such as for cancerous cells [69]. By using global shutter readout, the sampling is done on all pixels at the same time, which is required for a fast OCT. The sensor is designed for an FF-OCT system where the important specifications of high frame rate and resolution had to be reached. Other specifications included dark FPN and dark read noise, which were not as critical. The advantage of using such a high full well, 2 Me-, is the possibility of viewing a small signal in a bright background whereas the shot noise limits the performance. By such full well capacity, shot noise performance is good which allows for sensing of weak variations in the contrast.

System Description

The system was based on the FF-OCT technique and was explained in Section 4.2.4. In short the system takes the difference between two images, from the mirror and a subject, and the differential image is detected by the image sensor.

The sensor has 1440 x 1440 pixels with 12 μm pixel pitch. The architecture was designed in 0.18 μm with a supply voltage of 5 V and 1.8 V. The architecture of the image sensor can be seen in Figure 4.17 where the main blocks are shown.

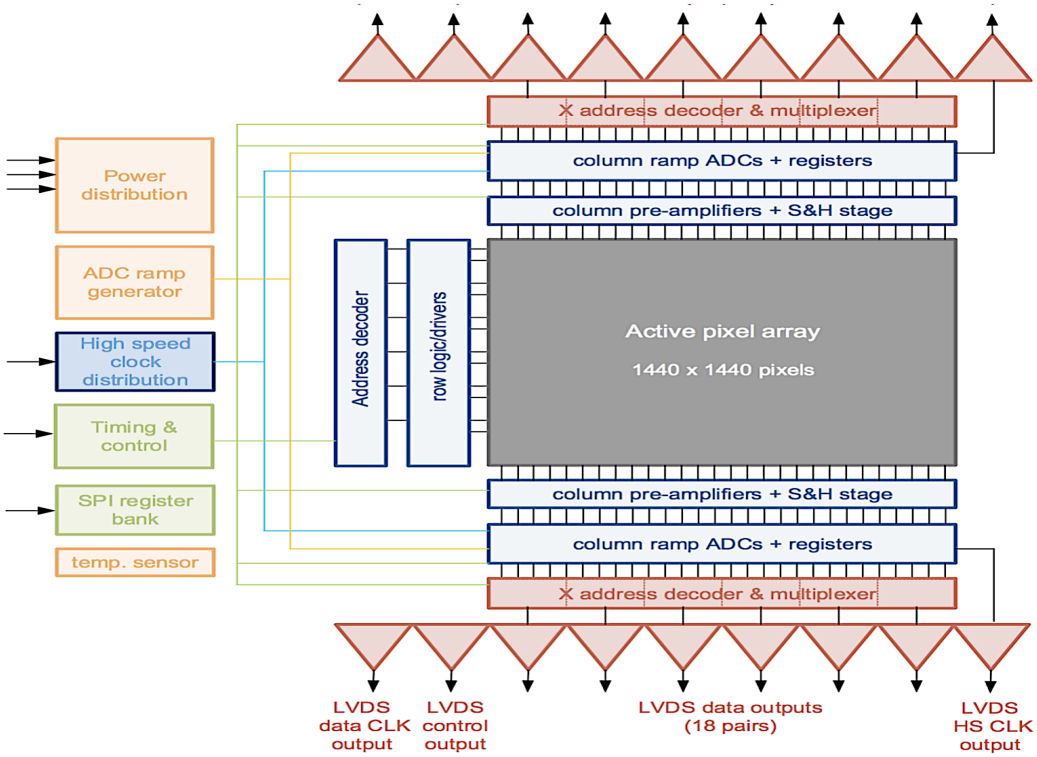

Figure 4.17: Image Sensor Architecture [57]

Due to the requirement of high frame rate, the sensor has to be read out from both sides of the pixel array, where two rows can be read out on each side. Therefore the column amplifiers and ADC are designed on half of the pixel pitch. The sensor includes 36 pairs of Low-Voltage Differential Signaling (LVDS) outputs.

Pixel Structure

The pixel has to combine the global shutter and a large full well capacity with a limited pixel area. In Figure 4.18 the pixel schematic is shown with 6 μm x 6 μm photodiode of 19 fF capacitance. For the large well capacity a parallel connected NMOS capacitor of 87 fF is added. Other properties were added to the circuit such as thicker gate oxide in order to increase the signal swing. The pinned photodiode was eliminated as a large full well capacity would be difficult to reach. Finally, with a second sampling stage CDS could have been added. However, it would have limited the full well capacity as well.

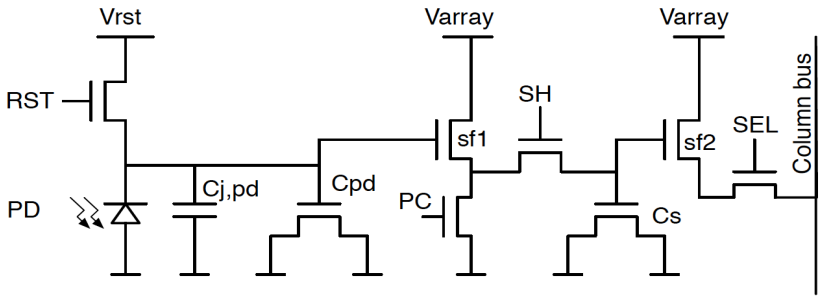

Figure 4.18: CMOSIS System Pixel Sensor [57]

The pixel works as follows. After a reset (RST), the source follower ($sf1$) amplifies the light signal charges that are stored in the large full signal well. The PC switch is a current source load for the source follower and is used to charge a sample capacitor (C_s) with the switch (SH). Finally the second source follower ($sf2$) buffers the signal onto the column bus whereas the switch (SEL) selects the pixel for readout.

Results

Below in Table 4.5 specifications reached with the global shutter image sensor is listed.

Table 4.5: Specifications and Results of the Global Shutter CMOS Image Sensor

Sensor	**CMOS Detector Array**
Resolution	1440 x 1440 pixels
Pixel size	12 x 12 μm^2
Full well charge	2 Me-
Fill Factor	25 %
Frame rate	730 fps
Dynamic range	66 dB
Dark current	3799e-/s
Axial Resolution	1 μm
Lateral Resolution	1.5 μm

By comparison with a conventional image sensor of 90 $ke-$ full well capacity, the CMOSIS global shutter sensor showed significantly more contrast and detail, see Figure 4.19.

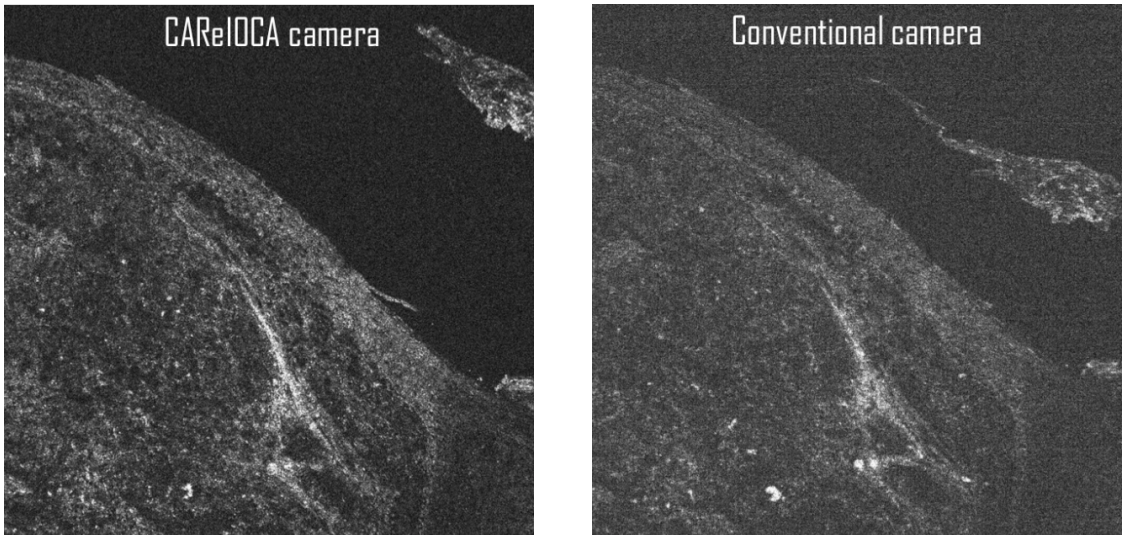

(a) CMOSIS Image Sensor (b) Conventional

Figure 4.19: OCT Image Comparison [57]

While the low coherence light offers high axial resolution and the technique overcomes using light beam scanning and optical reference scanning, the disadvantage about FF-OCT is the difference in acquisition time which is much longer than in scanning OCT. Thereby, object motion during the acquisitions time could cause signal blur, lower contrast and undesirable signals [70].

4.5 CMOS Image Sensors Design Methodology in OCT

Previously, multiple studies which presented the use of CMOS image sensors in OCT have been introduced and studied. Beforehand different OCT techniques and their signal retrieval optimizations were presented. In this section the CMOS sensors and their system results are summarized and compared.

4.5.1 OCT CMOS Image Sensor Comparison

Previously three different literature studies, which applied a CMOS image sensor as a detector to their system, were presented. The first study presents the research on applying a CMOS image sensor to an OCT system instead of a CCD or a fibre optic sensor [62]. The second study shows a way of improving the frame rate using a CMOS sensor in an OCT system [66]. Finally, the third study presents a state-of-the-art image sensor optimized for an FF-OCT system [57]. In Table 4.6 a comparison of the image sensor results and properties are shown.

Table 4.6: Comparison of the Specifications and Results from the Image Sensors

Sensor	**2D Smart Array**	**CMOS-DSP**	**Global Shutter CMOS**
Publication	2001 [62]	2006 [66]	2015 [57]
Type	TD-OCT	FF-OCT	FF-OCT
Resolution (Pixels)	58 x 58	1024 x 1024	1400 x 1400
Pixel size	110 x 110 μm^2	8 x 8 μm^2	12 x 12 μm^2
Frame rate	6 fps	235 fps	730 fps
Dynamic range	58 dB	Unreported	66 dB
Axial Resolution	16 μm	22 μm	1 μm
Lateral Resolution	Unreported	14 μm	1.5 μm

4.5.2 Design Methodology

From an image sensor design point of view, the essential parts which has to be included in the structure of an OCT image sensor are a large full pixel well, high pixel resolution and an as large photodiode area as possible. The design, at the same time, depends on the predefined specifications, such as the cost and area.

From the comparison it can be seen that the FF-OCT technique systems had most to gain with the addition of CMOS sensors. The study with the 2D smart array detector applied the time-domain technique and with the addition of a CMOS detector a full field view is retrieved which was beneficial for the speed and resolution. However, the sensor itself included few pixels and due to the scanning of the arm, the frame rate was low.

The CMOS-DSP sensor was developed with higher frame rate due to the random addressable pixels. By specifying a region of interest, a different approach to OCT was presented.

Finally, the global shutter CMOS detector showed very high performance. Some factors that were a disadvantage for the previous sensors were improved, such as the resolution, frame rate and the dynamic range. From the study of the techniques it became clear that a full well size played a large role in the detection sensitivity. However, for further improvement the main possibility would be to increase the full well capacity even further with a different architecture, optimizing the photodiode fill factor and even increasing speed more.

5 Conclusion

Through this first part of the thesis, a feasibility study on the potential of CMOS image sensors in OCT has been constructed. From the explanation of the light source, subject and the detector, the tradeoff between the optimal region of the light source and subject tissue alongside the optimal quantum efficiency of the silicon image sensor were discussed. Factors that play a role in an informal decision on a light source and a detector have to be based on the type of the subject tissue and the properties of the sensor, which then again could be limited by the cost.

Furthermore, different OCT principles were discussed with the focus on the improvement of the speed with working in the frequency domain. By comparison, the FF-OCT had an advantage in performance with the possibility of taking a direct image without a complex system. Finally, a literature study presented three studies where the focus has been on CMOS image sensor detectors in OCT. The first paper being published in 2000, had some promising results. Even though further work on the sensor included improvements on both the resolution, fill factor, frame rate and dynamic range, the use and feasibility of CMOS image sensors in OCT was shown. The next paper, from 2006, showed the use of a commercial CMOS-DSP camera. With its use of an ROI with random addressable pixel technique the frame rate was highly increased. In 2015, as a part of an European Union sponsored project, CAReIOCA, CMOSIS released a sensor for OCT which showed state-of-the-art results concerning speed, resolution and dynamic range.

The contribution of this thesis to the field of engineering and optical tomography is the summary of the topic and literature study to prove the feasibility of CMOS image sensors in Optical Coherence Tomography. This thesis tries to go into most aspects of Optical Tomography with the focus on the detectors. The goal of the thesis is to inform the reader on the current status of the published position of CMOS image sensors in the field of Optical Coherence Tomography with the focus on improvements. This feasibility study showed that in OCT an image sensor with a large FWC accomplished higher detail than previously published conventional sensors. In conclusion, the use of CMOS sensors in OCT increases flexibility of the device, reduces the cost and could possibly even further improve the image quality. However, whether a new sensor, further optimized than the Global Shutter sensor from CMOSIS, will return a significant value in research, is unknown.

Part II

Neural Network Learning Algorithms

6 Artificial Neural Networks

Artificial neural networks have been a research topic since the 1940s [71]. However, only fairly recently have researchers discovered a great potential for artificial neural networks due to advancements in computing power. Advancements in GPUs (Graphics Processing Units) enabled faster training of large scale networks, the most computation intensive task, using algorithms such as the backpropagation algorithm. The state-of-the-art devices offer a great amount of performance, but at the cost of power consumption. A single device can use up to several hundreds of Watts, which obviously does not fit every application's power envelope.

In order to address this problem, research is done in specialized, less power hungry solutions. Both Application-Specific Integrated Circuits (ASICs) and Field-Programmable Gate Arrays (FPGAs) are used. Fully customized ASICs can be implemented either in the digital or analog circuitry. While depending on application, digital circuitry can offer shorter time-to-market development due to the possibility of using existing logic elements. The sizing of the circuit depends on the precision needed for the application. Analog circuitry, on the other hand, can offer very low power consumption, small area and precision at the price of increased circuit design complexity compared to digital circuits.

This chapter focuses on artificial neural networks in general. Bear in mind that only fundamental background information is provided, since an in-depth look at neural networks is outside the scope of this work. Section 6.1 firstly explains the general concept and the structure behind neural networks with an introduction to the developments of the memristor. Thereafter it goes into learning algorithms, their execution and performance. In order to show the use of neural networks medical applications, which benefit highly from neural networks, are presented and their prospects are discussed in Section 6.3. Finally, in Section 6.4 the description of the project and how the second part of the thesis aligns up is presented.

6.1 Neural Networks

Artificial neural networks are based on a concept derived from the biological behaviour of our brain. The brain uses millions of cells in parallel for learning purposes. Algorithms have been developed which capture the brain's learning functionality and enable our devices to operate in a similar fashion. These learning methods use a known data set to learn from, after which the artificial neural network can be used by itself to classify unexpected inputs. Therefore it is important to have a large, diverse and complete training set. Artificial neural networks have gained a lot of momentum over the last years. The ability to teach machine skills similarly to that of the human brain proves to be useful in an increasing number of applications ranging from image recognition to diagnosing patients. Therefore, artificial neural networks are not limited only to human-like skills such as image or speech recognition, but can also learn to diagnose diseases, by studying an immense amount of data.

Basically, artificial neural networks can be divided into two types, either as a feed-forward network (single or multi-layer perceptrons) or as a recurrent network. Feed-forward networks have an input layer, a hidden layer and an output layer. The computation is done layer by layer from the input to the output [72]. For recurrent networks, signals have the ability to travel in loops back and forward within the network.

In relation to the concepts of the human nervous system, the components of the neural network bear the same name of the neuron and a synapse, see Figure 6.1 [a]. Like in the human brain, the neuron processes and transmits information through a synapse to the next neuron. The synapse is a complex junction where an individual neuron can link to thousands of other neurons, which is used to transmit the signal to other neurons [73]. An artificial neuron is a processing unit which adds its weighted inputs together and with an activation function (non-linear transfer function) generates an output [74], see Figure 6.1 [b]. The simplest form of an activation function is the Heaviside step function but problems can be solved by other more complex and accurate functions such as the sigmoidal function which can be defined as $S(x) = \frac{1}{1+e^{-x}}$.

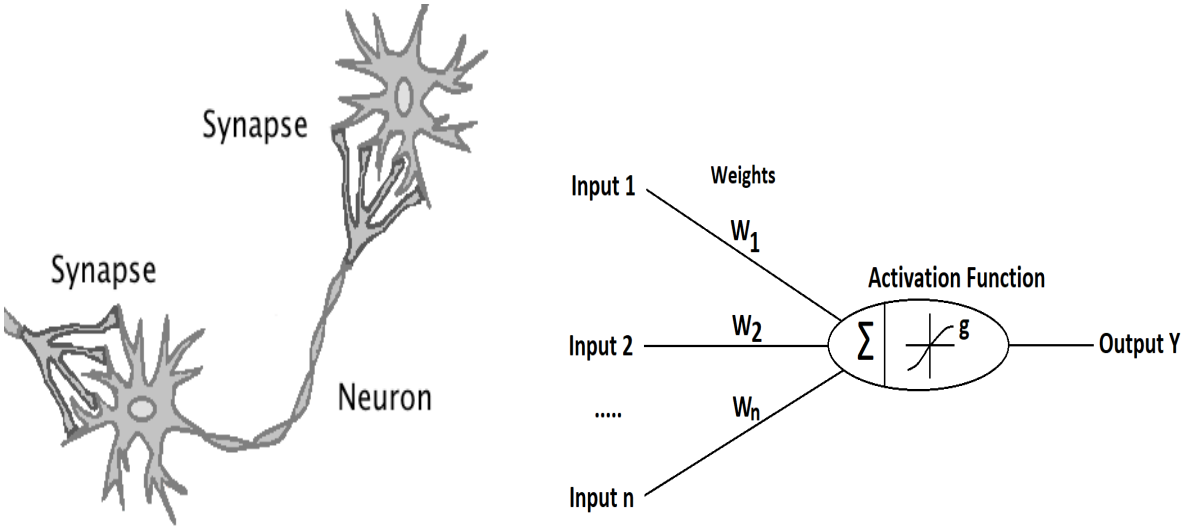

(a) Synapses and Neuron in the Human Brain

(b) Synapse and Neuron in a Neural Network

Figure 6.1: Comparison between Artificial and Biological Neurons [75]

An important, but compute intensive, feature of neural networks is its learning ability. With learning algorithms the accuracy of a neural network can be improved. The learning algorithms involve training models which can solve difficult problems when the conventional computer algorithms are not sufficient. Training networks can be described in two steps, first the learning stage and secondly the recall stage [72]. The learning stage is about adjustments of weights and the recall stage is when the network settles and goes into equilibrium with weights closest to the optimal values the algorithm was able to reach.

6.1.1 Memristor

Synapses increase quadratically in complexity when more neurons are added to the network, because each new neuron has to connect to every other neuron. Therefore, an efficient implementation of multiple neurons can be challenging. However, a simple yet efficient structure called a memristor has been shown to have potential as a synapse. The theoretical structure was first published in the 1970s by Leon Chua [76], where its placement belonged alongside the

three fundamental passive elements, the resistor, capacitor and inductor. The basic function of the memristor was to base its resistance on the previous signal flowing through the device. With this, the device could act as a non-volatile memory, memorizing the previous function. Nevertheless, no physical model was implemented for years to come. It was not until recently, with the recent advancements in computing, that development was driven forward. Multiple types of memristors have now been published such as a Titanium dioxide memristor [77], [78], Polymeric memristor [79], [80], Layered memristor [81] and Self Directed Channel (SDC) memristor [82].

The last mentioned memristor, SDC, is the most recent one and has opened the door for commercial memristors [83]. Dr. Campbell developed and introduced the SDC memristor in 2017. For interested readers the published structure of the memristor, top overview and cross-section, is presented in Figure 6.2 and discussed briefly below.

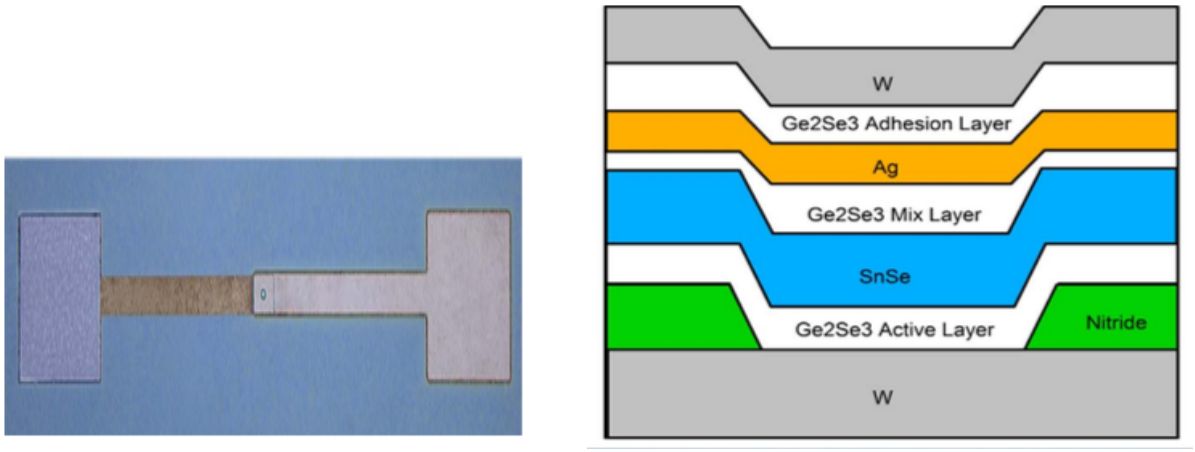

(a) SDC Memristor Top Overview

(b) SDC Memristor Cross-Section

Figure 6.2: SDC Memristor Structure [82]

The two terminal memristor works as follows. On each terminal there are electrodes, marked as W, where the voltage over the device changes with the previous signal. The Ge_2Se_3 active layer is where the switching occurs due to $Ge - Ge$ homopolar bonds. The Ge_2Se_3 adhesion layer, Ag layer and Ge_2Se_3 mix layer form the Ag source layer. These two layers, the Ge_2Se_3 active layer and the Ag source layer, are not in contact which allows for higher processing and operating temperatures as Ag is not able to migrate into the Ge_2Se_3 active layer. The $SnSe$ layer assists a selective incorporation of Ag ions into the Ge_2Se_3 active layer [82]. The device does not require a complex fabrication process thereby allowing for faster and more reliable production. This device gives the ability of a fast response and high endurance.

6.2 Learning Algorithms

Learning algorithms involve training methods and how to execute them efficiently, depends on the application. Learning can be done on-chip, if the same system will execute the model with new input data as well, or off-chip when learning is done on a separate system than the system executing the trained model. A hybrid approach is also possible, as mentioned earlier.

Simple, small networks are best approached by CPUs and larger networks by GPUs if power consumption is not of interest. However, other applications would benefit from custom solu-

tions, either using ASICs or FPGAs.

The learning algorithm architectures are varied and developed to train the network optimally. Many algorithms have been published and one of the most popular learning algorithm is the backpropagation algorithm. This algorithm was first proposed by Werbos in the 1970s but was further developed by Rumelhart and Le Cun in the 1980s [84]. This algorithm is CPU and GPU friendly. However, the Random Weight Change (RWC) algorithm is more suited for custom hardware solutions.

6.2.1 Execution of Training Algorithms

Traditionally, neural networks are trained on CPUs and more recently on GPUs. These implementations have had great success in the development of new algorithms as well as with debugging small networks [84]. While the use of GPUs decreased the execution time significantly, power consumption is in the order of several hundreds of Watts. Recently, FPGAs and ASICs are being adopted which enables customized solutions with a lower power consumption. Also the execution time can be decreased for large networks [74]. While FPGAs offer reconfigurability, their power consumption does not fit all applications (for example within/on a human body). ASICs offer implementation of fully customized circuitry, either in the analog or digital domain.

However, for some cases a mixture of on- and off-chip learning can be used. Such a system was described in [85]. There the backpropagation algorithm was executed on a host computer and from there weights were calculated. These weights were then uploaded to the hardware were another algorithm was implemented on chip for finer-grain training.

Concerning hardware development, both the neuron and synapse have certain features and challenges. A neuron performs addition of weighted inputs and with an activation transfer function generates a non-linear output. Efficient implementation of the input addition and the activation transfer function depends on the system and application. The synapse, which controls the communications between the neurons, can quickly become complex and vast due to the wiring. Synaptic weights have to be precise for proper convergence of the algorithms. These as well have to be update-able. Challenges thereby include minimizing wiring and required precision.

ASICs can be implemented either in the digital or analog domain. In the analog domain the signals can be presented either as a current or a voltage difference. In the digital domain, the design is more straightforward and can rely on existing logic elements. Synapses can be created with memory cells or latches where the algorithm relies critically on the precision of the data type (integer, double precision, floating point etc) used and the required number of bits. Neurons can be implemented with adders and multipliers [72].

Even though the analog circuitry is highly complex compared to the digital circuitry, the analog domain is able to offer more power and area efficient circuits [72]. When implementing the weight for the synapse, memory elements both in the digital and analog domain can be used. Nevertheless, in the case of digital elements, a latency is observed in the computation time. For analog systems, capacitors or resistors can be used as storage. However, due to the manufacturing, analog accuracy is limited and must be designed with a certain tolerance.

6.2.2 Backpropagation Algorithm

The backpropagation algorithm is an efficient learning algorithm. By computing an error of a network at the output, the error is fed back into the hidden layer and used to adjust the weights of the neuron. The network uses this error to adjust the weights in order to approach the current output towards a desired output [74]. The algorithm can be described as follows, the error, E, is generated by subtracting the output value, y, from the target value, t. The backpropagation algorithm performs gradient descent for minimizing E^2, where E is as shown with Equation 6.1:

$$E = \frac{1}{2} \sum_{j \in outputs} (t_j - y_j)^2 \tag{6.1}$$

The weight update, w, for the system, from w^n to w^{n+1} is, see Equation 6.2:

$$w^{n+1} = w^n + \Delta w^{n+1} \tag{6.2}$$

where Δw^{n+1} is, see Equation 6.3:

$$\Delta w_{i,j} = -\eta \frac{\partial E}{\partial w_{i,j}} = -\eta \delta y \tag{6.3}$$

Here, η is the learning rate and δ the sigmoidal function. The activation function can be presented as, see Equation 6.4:

$$\delta_j = y_j \ (1 - y_j) \sum_{k \in outputs} w \delta_j \tag{6.4}$$

Figure 6.3 summarizes these steps for a multi-layered network where the weight is updated from the output back to the input.

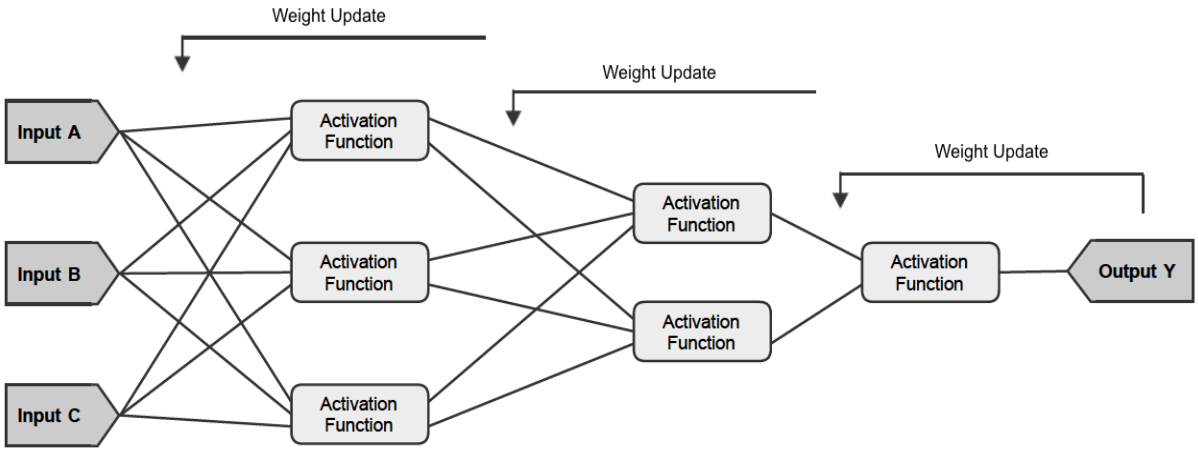

Figure 6.3: Backpropagation Implementation

From various inputs, a summator is previous to each activation function. The activation function then generates a non-linear output. From the final output (*Output Y*), the weights are updated towards the input depending on the error. The disadvantage of the backpropagation algorithm is that the hardware implementation is very complex [85]. The algorithm relies on differential equations, which are expensive in dedicated hardware.

6.2.3 RWC Algorithm

An example of a more hardware friendly algorithm, due to simple circuit implementation, is called a Random Weight Change (RWC) algorithm. This will be discussed in an example in Chapter 7. RWC can be implemented in a relatively simple circuitry without derivative calculations of the activation function [85], [86]. In Figure 6.4, the hardware architecture is shown.

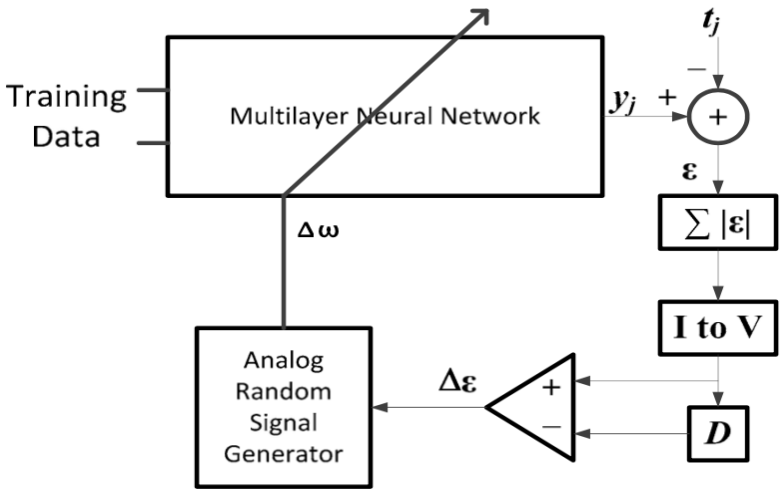

Figure 6.4: The RWC Learning Algorithm [85]

To describe this process, initially the neuron is programmed with starting weights, w, inside the multi-layer neural network. The analog weight updating vector (Δw) is generated and updated via training. This is done by an analog random signal generator which is programmed to the network. A training data vector is applied to the input for the training. At the output of the neural network, the difference between the output (y_j) and the target value (t_j) is taken. From this difference, an error vector (ε) is retrieved and with an absolute value circuit, absolute values are generated. An analog absolute value circuit will be discussed in detail in Chapter 8. Lastly, the signal is converted into voltage. In order to realize whether to update the weights or not, values generated previously are compared to the most recent values by a comparator. This is done by storing the previous value on a capacitor, D. The output from the comparator, $\Delta\varepsilon$, defines the update for the next cycle [85].

For a comparison of the algorithms, Figure 6.5 shows how the backpropagation and RWC algorithm close in towards a solution. Backpropagation approximates a solution with a gradient descent while RWC does not descent with the steepest slope but slowly decreases to reach the final solution [86].

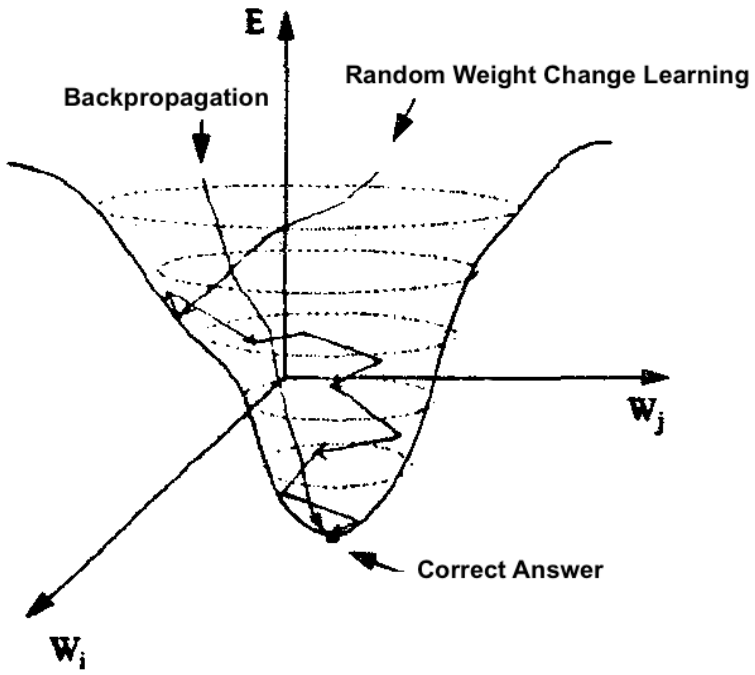

Figure 6.5: Comparison between Backpropagation and RWC Algorithm [86]

As explained in the beginning learning systems can be combined into a hybrid system. This can be done with the backpropagation algorithm and the RWC algorithm. This often turns out to be the best case due to algorithm iterations. Applying only hardware algorithm to the network would take too long due to its random seeking behavior. For a software-only version, the learning weights are non-compatible due to non-ideality of the hardware. By combining the two, the weights are optimized using a software, updated to the circuit, which then adapts them to its hardware. This shortens the iteration time and optimizes the weights.

6.2.4 Performance

Neural networks have been adapted to a wide range of applications where they outperform the standard (original) implementation or have similar performance. Applications such as computer vision, recognition methods and function optimization, all benefit from neural networks. In order to weigh and estimate the performance from a certain neural network, parameters which have a high importance are firstly the size of the network and secondly the computing power. The capacity of a system can be estimated from the number of weights in the system and as such the final implementation complexity and training difficulty can be assessed more precisely [84]. Performance is measured in connections per second (*cps*) which directly implies the amount of data being processed in the network per second. However, the performance of the learning algorithm is measured by connection updates per second (*cups*). As an example, the performance required for complex vision problems and sophisticated speech recognition models are in the order of Giga *cps*. While the commercial computer is only able to handle simple recognition this has motivated the development of special co-processors [72], [84].

In summary, when implementing specialized hardware for neural networks certain challenges arise. For the synapse, the number of synapses scale quadratically with the number of neurons, which causes an immediate increase in area. Weights have to be defined with high precision and have to be update-able. For the neuron, summation of weighted input and non-linear cal-

culations must be performed [72].

6.3 Published Applications of Neural Networks

Neural Networks have proved to be highly beneficial for medical purposes, in applications such as cochlear implants, visual stimulation and even vagus nerve stimulation. All these applications benefit from low power consumption as well as small area. Below, couple of applications are briefly presented with their features and developments in order to gain some insight into the current importance of neural networks.

6.3.1 Cochlear Implants

The way external sound is transformed into information understandable to the brain involves a complex processing. External sound waves are led through a passage to an eardrum which vibrates under their influence. By three bones, malleus, incus and stapes, the sound vibrations are interpreted and carried to the cochlea. The fluidic cochlea creates waves which cause movement of cochlear hair cells. This movement then converts into an electrical signal, a nervous impulse, which conducts through the auditory nerve to the brain. The structure of an ear can be seen in Figure 6.6 [a].

Cochlear implants are able to replace certain functions of the ear where there is damage. The standard device includes a microphone, speech processor, transmitter, receiver and an electrode array, as shown in Figure 6.6 [b]. The processor digitizes the external sound with the use of a microphone. The transmitter transmits the signal to an internal receiver where the information is converted into electrical impulses along the electrode array which stimulate the auditory nerve.

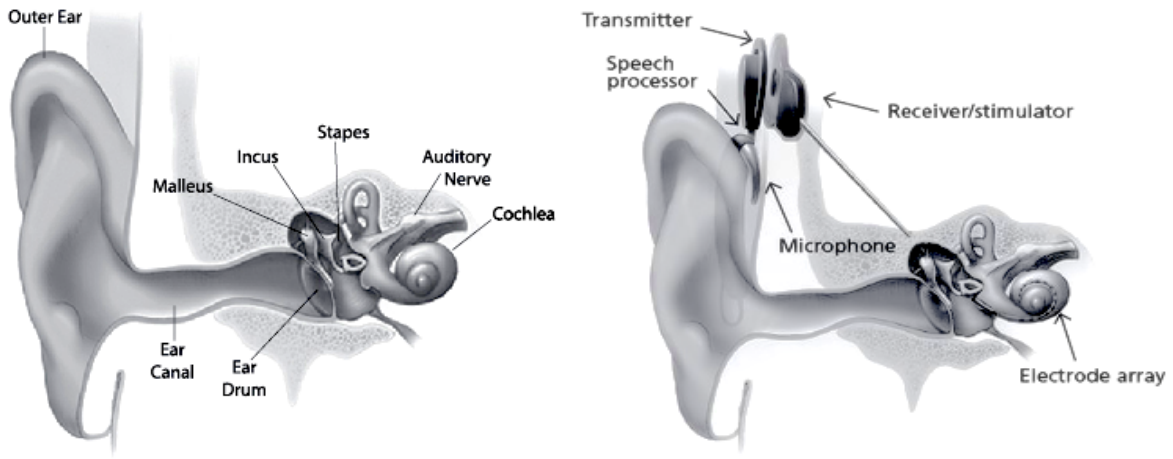

(a) Structure of the Ear

(b) Cochlear Implant merged with the Ear

Figure 6.6: Structural Representation of an Ear with and without a Cochlear Implant [87], [88]

State-of-the-art cochlear implants are able to provide near to normal speech understanding in quiet conditions, nevertheless, the quality quickly fades away in the presence of environmental sounds [89]. This problem has been addressed by multiple algorithms such as trying to attenuate the noise component of the noisy background or by spatially separating the target signal and the interfering noise. However, the requirements for these methods are not always fulfilled. Single-microphone speech enhancement algorithms show that the improvement on the SNR,

leads to improved speech intelligibility but the errors might lead to a distortion. Furthermore, machine learning has been used to estimate the gain function which has shown large intelligence improvement. By using neural networks, improvement has been made on noise in speech [89]. Future development of neural networks in speech recognition is expected to have even higher accuracy and performance to unforeseen conditions. For interested readers, an example of a feed-forward neuron model implant can be seen in Figure 6.7. By adding a feed-forward neural network to the cochlear implant, the system has the possibility of accepting multiple sounds in a multi-channel system.

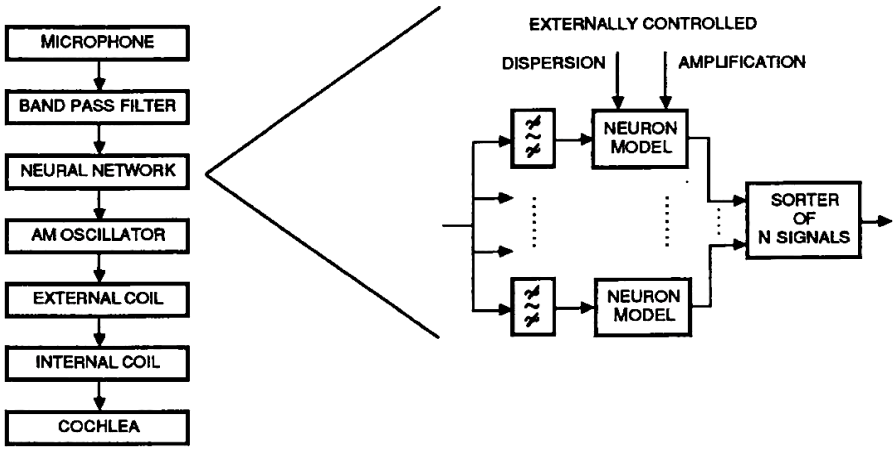

Figure 6.7: Feed-forward Neuron Model [90]

Future developments include the combination of low power chips and neural network. This offers the possibility of implants which are fully implantable. This is done by eliminating the external part of the standard implant as proposed in [91].

6.3.2 Visual Applications

Visual impairment is limiting for people's daily tasks. Certain technologies have the ability of improving their life by computer vision based assistance. Both color recognition and object recognition can be emphasized [92], [93]. By enhancing vision, shapes of objects and color can be further viewed. A software neural network is used in order to train the algorithm to optimize the system closest to reality. For both blinds and visually impaired individuals, there is a big room for development and improvements.

Neural networks have shown their prospects in creating visual connections for those in need of a real time sight. A company called Eyra, has already announced their future product, Horus, which uses artificial intelligence to enable sight for blind and visually impaired people. The product launch is expected during 2017/2018 [94]. Other products, hopefully with release dates in the near future, will greatly benefit from neural networks and include implanted chips for brain injury [95] and vague nerve stimulation [96].

In summary, whether it is for the system to learn to analyze different sounds or optical signals, applying and improving learning algorithms and neural networks is highly advantageous.

7 Architecture

The main goal of the project was to design a neural network with associated learning capabilities fulfilling the requirements of limited area, low power consumption and low noise. With the inspiration from image sensor methodology the design was approached from an image sensor pixel array design. The initial challenges to the system included ways to sense the signal, its processing and data handling. Further along challenges arose for competitive solutions towards the specifications.

In this chapter the project is approached from a high level towards the design of single components in the network of the neuron architecture. Section 7.1 starts by explaining weak inversion in order to give an understanding of the behavior behind the circuit developed. Weak inversion is an operating region of a MOSFET transistor which is known for offering the possibility of extreme low power consumption. Section 7.2 discusses the structures developed at Caeleste and its features are explained from a broad perspective. Section 7.3 presents the system architecture with a learning algorithm in order to show a useful application of the developed absolute value filter.

7.1 Weak Inversion

In addition to the background knowledge presented in Chapter 2, operation regions of the MOSFET transistor are presented, with the focus on weak inversion. As this behavior was ignored for years due to a very low current level, its use rose to the surface during the 1970s, when the electronic watch requested limited power consumption [97]. The weak inversion or subthreshold behavior was discovered in relation to how the drain current had an exponential dependency on the gate voltage, as the leakage current kept flowing in an OFF mode.

A MOSFET transistor has either a n- or p-channel and as mentioned before, the carriers are either electrons (n) or holes (p). In Figure 7.1 [a] an n-channel MOSFET (NMOS) transistor can be seen.

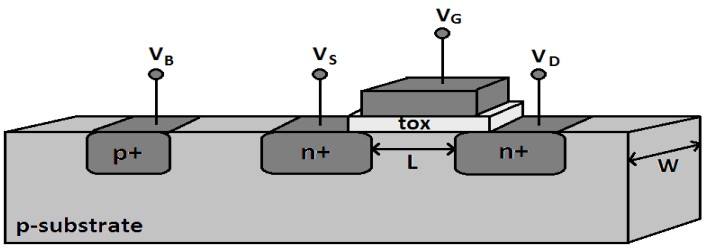

Figure 7.1: NMOS Transistor Structure

The NMOS transistor shows two n-type ($n+$) regions, the drain voltage, V_D and the source voltage, V_S. The low resistivity gate layer, which can be polysilicon, alumnium or tungsten metal, is the gate voltage, V_G. All these voltages are defined with respect to the local substrate, the base voltage, V_B. The silicon dioxide layer, SiO_2, is the gate oxide with a thickness of t_{ox}. The silicon dioxide is commonly used due to its stability and quality as an insulator. The channel between source and drain is defined by the gate width, W, and the gate length, L. The PMOS is different in a way that the doping is reversed and is built into an n-well substrate.

The MOSFET transistor has three operation regions, the subthreshold region, the resistive (triode/linear) region and the saturation region where its definition is dependent on the gate voltage and the threshold voltage, V_T, of the transistor. When a gate voltage is applied, a depletion region forms. Depending on whether the electrons or holes are the majority carriers, the behavior can be translated to either one by changing its polarity. In short, for NMOS, when the gate voltage is below the threshold voltage ($V_{GS} < V_T$) the transistor acts in the subthreshold region. When it is above ($V_{GS} > V_T$, $V_{DS} \leq V_{GS} - V_T$) it acts in the triode region. For the small signal model this behavior is linear. For ($V_{GS} > V_T$, $V_{DS} > V_{GS} - V_T$) the transistor is in saturation. The same goes for a PMOS when the signs are reversed. The transistor behavior in different operation regions can be seen in Figure 7.2 which presents the transfer characteristics of the drain current, I_D, as a function of the drain to source voltage, V_{DS}.

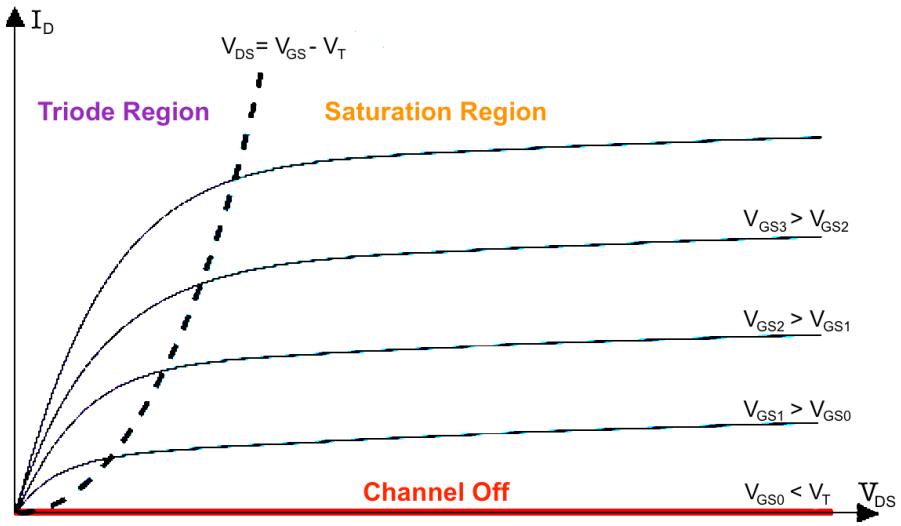

Figure 7.2: I_D versus V_{DS} Characteristics of an NMOS [98]

The behavior of the transistor can also be described by the drain current as a function of the gate source voltage or how the V_{GS} influences the size of the drain current, see Figure 7.3 [a], whereas under the threshold voltage, V_T, the channel is off. However, when a drain current is measured at log scale the drain current is made more visible under the threshold voltage and is not fully off, this behavior is called weak inversion or the subthreshold region, see Figure 7.3 [b]. As the gate-source voltage is high enough but still under the threshold voltage it can create a depletion region large enough to conduct current. Minority carriers were before looked at as an undesirable leakage current by limiting the performance of the transistors. Nevertheless, for low power applications this is highly beneficial [99].

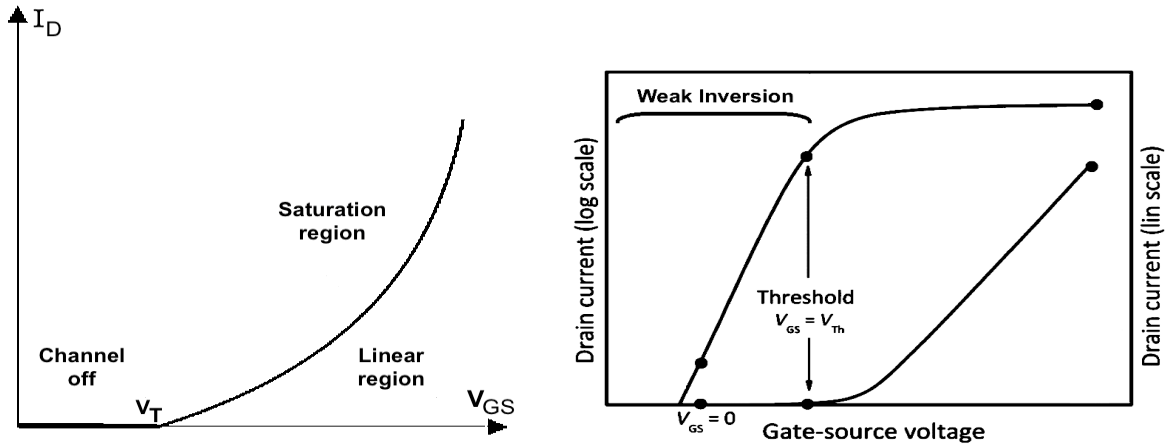

(a) I_D versus V_{DS} Characteristics of an NMOS

(b) I_D versus V_{GS} Characteristics of an NMOS

Figure 7.3: Transistor Behavior in Different Operating Regions [100]

The gate oxide thickness, t_{ox}, defines the capacitance per unit area, see Equation 7.1:

$$C_{ox} = \frac{\epsilon_{ox}}{t_{ox}} \tag{7.1}$$

where ϵ_{ox} is the permittivity of the oxide which is normally $3.9\epsilon_o$. The permittivity of free space is $\epsilon_o = 8.85 \cdot 10^{-14}$ Fcm^{-1}. An important factor which describes the behavior of the structure is the thermodynamic voltage, see Equation 7.2:

$$V_t = \frac{kT}{q} \tag{7.2}$$

where k is the Boltzmann constant, q elementary charge and T the absolute temperature. This describes how the electron energy is influenced by the temperature. For an intrinsic semiconductor in the dynamic equilibrium, the concentrations of electrons and holes are equivalent, $n_e = p_h = n_i$. However, in doped semiconductors mobile carriers in equilibrium obey the law of mass action, which predicts their behavior in dynamic equilibrium [101], see Equation 7.3:

$$n_e \cdot p_h = n_i^2 \tag{7.3}$$

where n_e represents the electrons, p_h the holes and n_i is the intrinsic carrier concentration in silicon as a function of temperature ($n_i = 1.45 \cdot 10^{10}$ cm^{-3} at room temperature, $T = 300$ K). In transistors this concentration can be controlled by doping. Boron is commonly used as a doping, N_A, for PMOS transistors where holes, p_h, are the majority carriers. In contrast, in NMOS Phosphorus is used as a doping, N_D, where the majority carriers are electrons, n_e. Typical doping levels can be approximated for both, by $N_A, N_D \approx 10^{15} - 10^{16}$ cm^{-3}. For these carriers their concentrations can be approximated by, for holes and electrons, respectively, in a PMOS transistor as, see Equation 7.4:

$$p_{pmos} \cong N_A \qquad\qquad n_{pmos} \cong \frac{n_i^2}{N_A} \tag{7.4}$$

The same applies for the NMOS transistor, N_D. In order to understand these effects on the behavior of the transistor, the threshold voltage function is derived. When a positive voltage is applied to the gate of an NMOS transistor the holes are repelled from the surface and a

depletion layer forms. This increases the surface potential, ψ_s, and in relation to the depletion layer the negative charge density, Q_b, can be derived as, see Equation 7.5, [97]:

$$Q_b = -\Gamma_b C_{ox} \sqrt{\psi_s} \tag{7.5}$$

where C_{ox} is the oxide capacitance and Γ_b, the substrate modulation factor, see Equation 7.6:

$$\Gamma_b = \frac{\sqrt{2qN_b\epsilon_{si}}}{C_{ox}} \tag{7.6}$$

where N_b is the doping concentration of the substrate and ϵ_{si} is the permittivity of silicon. Even though Q_b presents only a fixed charge then as electrons are attracted to the positive surface potential, mobile charges form on the surface, Q_i. The small inversion layer created by this charge has a low voltage drop. The total charge density underneath the silicon surface, Q_{Si}, can be given with Gauss law as, see Equation 7.7:

$$Q_{Si} = Q_b + Q_i = -C_{ox}(V_G - V_{FB} - \psi_s) \tag{7.7}$$

where V_G is the gate voltage and V_{FB} is the flat band voltage which is the voltage when no charge is around. By further derivation of Equation 7.5 and 7.7, the threshold voltage can be derived as, see Equation 7.8:

$$V_T = V_{FB} + \psi_s + \Gamma_b \sqrt{\psi_s} \tag{7.8}$$

The threshold voltage, V_T, is though rarely calculated by hand as it is highly dependent on the CMOS technology parameters. In order to retrieve the threshold value, simulations with SPICE are able to calculate the values from a device model.

7.1.1 Drain Current in Weak Inversion

The current in a transistor is a combination of both drift and diffusion currents. Drift current is caused by an applied electric field and is defined by the charge carriers mobility and the electrical field [102]. In n-channel MOSFET the drift current is, see Equation 7.9:

$$I_{drift} = q \cdot n_e \cdot \mu_n \cdot E \tag{7.9}$$

where n_e is the number of electrons, μ_n is the mobility of electrons and E is the electrical field. Diffusion current is caused by a change in charge concentration which can be described as an electron flux. From Ficks law the diffusion current can be derived as [102], see Equation 7.10:

$$I_{diff} = q \cdot D_n \cdot \nabla\eta \tag{7.10}$$

where η is the charge concentration and D_n is the diffusion constant. By the Einstein relation, the constant can be represented as follows [103], see Equation 7.11:

$$D_n = \mu_n \cdot V_t = \mu_n \cdot \frac{kT}{q} \tag{7.11}$$

The change in the charge concentration can be approximated as follows [104], [105], see Equation 7.12, 7.13, 7.14:

$$\eta = \frac{dn}{dx} = \frac{n_p(0) - n_p(L)}{L} \tag{7.12}$$

where the charge concentration at the source in p-substrate, $n_p(0)$, is:

8 Non-Linear Absolute Value Filter

Electronic filters have their use in many applications and can be used for signal processing by eliminating unwanted features and enhance the wanted features inside a circuit. The absolute value filter is a signal filter which filters out the real component discarding its sign. As a part of the learning algorithm, an important novel absolute filter design is proposed. The proposed filter is a non-linear filter, where the output is not dependent on the input, operated in weak inversion. In order to analyze the performance of the filter, large and small signal analysis are applied.

In Section 8.1 non-linear filters are presented and discussed. Thereafter, in Section 8.2, a couple of different published absolute value filter circuits are presented. Section 8.3 presents the developmental phase of the absolute value filter structure alongside the current mirror. Finally, in Section 8.4 the filter is analyzed, simulated and discussed.

8.1 Non-Linear Filters

Filters are either linear or non-linear. They are able to amplify or reject signals at certain frequency ranges. A filter is able to process a signal by either altering the amplitude or the phase of the signal. The most common representation of filters are their gain versus frequency and phase versus frequency characteristics descriptions [110]. This frequency domain behavior can be described by a transfer function ($H(s)$) which is the ratio of the Laplace transform of its input and output, see Equation 8.1:

$$H(s) = \frac{V_{out}(s)}{V_{in}(s)} \tag{8.1}$$

Here s is a complex frequency variable. How the filter affects the magnitude and phase can be seen if s is replaced by $j\omega$, where j is $\sqrt{-1}$ and ω is $2\pi f$.

When dealing with non-linear filters there are only limited similarities to linear systems. Frequency domain analysis methods and a solution of state equations in time-domain do rarely apply for non-linear circuits [111]. Problems concerning circuit response and synthesis are common. With non-linear circuits the circuit response acts differently to different inputs and is not dependent on others [112]. Non-linear systems can often be represented by a mathematical expansion such as that described by Taylor and Volterra [113]. However, in this thesis complex analysis is avoided by approximations using the common methods.

8.2 Absolute Value Filter Publications

Multiple absolute filters have been published [114], [115], [116]. Absolute value filters are also known as full-wave rectifier circuits. As mentioned in Chapter 6.2, the RWC learning algorithm was originally implemented with a current mode absolute value circuit. Here below a short description of such a filter is presented. Thereafter another simple absolute value filter, based on Junction Field Effect Transistors (JFETs) is presented and explained. However, most of these circuits involve taking an absolute value of one signal. This means that other processing components need to be added to achieve the desired function for the learning algorithm. As for area being a limiting factor in the proposed network further development on a absolute value filter is presented in Section 8.3.

Current Mode Absolute Value Filter

In Figure 8.1 a translinear absolute value filter in the subthreshold region is presented. This circuit converts bidirectional current, I_{BD}, into two output unidirectional currents, I_1 and I_2. The bias current, I_B, then sets the operating point of the circuit. Translinear circuits are current-mode circuits based on the translinear principle which is outside of the scope of this thesis. However, this filter gives an idea on an implementation of a low transistor count and low power absolute value filter.

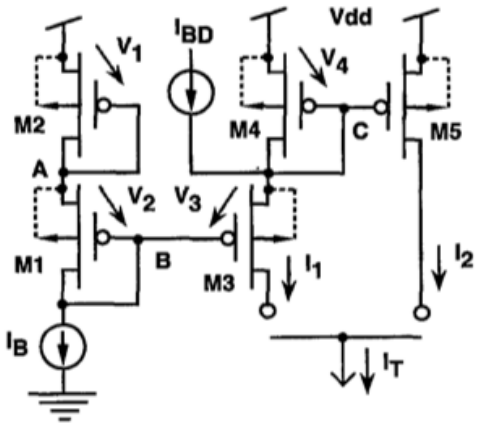

Figure 8.1: Translinear Current Mode Absolute Value Circuit [117]

Depending on whether I_{BD} is higher or lower than zero, the current goes through the transistors, M3 or M4 and M5. Transistor M5 creates a current mirror and deriving the output currents when $I_{BD} \gg I_B$, results in $I_1 \simeq |I_{BD}|$ and $I_2 \simeq 0$ or vice versa. These currents can then be connected together giving the final current of, see Equation 8.2:

$$I_1 + I_2 \simeq |I_{BD}| \tag{8.2}$$

Absolute Value Filter using Two Matched JFETs

In [118] an absolute value filter was designed using Junction Field Effect Transistors (JFETs) for low supply voltage applications. Despite the variety of existing absolute value filters, few have been developed for low power applications. In Figure 8.2 a simple absolute value circuit is presented.

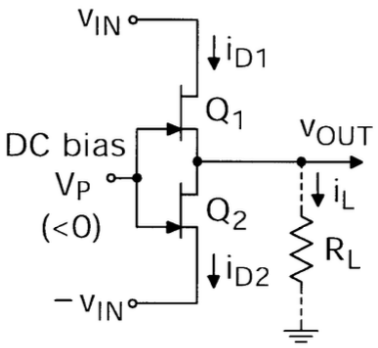

Figure 8.2: Proposed Absolute Value Circuit [118]

The absolute value filter works as follows. Since the NMOS transistors are identical, one transistor works in the saturation region while the other one is operating in the triode region. The DC bias sets the pinch off voltage, V_P, and the load resistance is high enough for the output current to be smaller than the drain currents from the transistors. With derivation of the currents, the expression of the output can be found as, see Equation 8.3:

$$V_{out} \cong \frac{1}{\sqrt{2}}|V_{in}| \tag{8.3}$$

The application does not require a voltage output but can be beneficial as no current to voltage converter needs to be applied in the RWC learning algorithm circuit.

8.3 Architecture

The goal of the implementation of the absolute value filter was to be able to take the absolute value of the difference between two different input signals. This can be the output from the network and the target data fed into the network. Previously, a couple of absolute value filters were mentioned but they only offer one input. Thereby, in order to implement such filters the network would require further circuitry to the component which at the same time would decrease the performance of the desired filter due to the area and power limitation.

The development of the absolute value filter started with a circuit capable of taking the difference between two signals or a differential amplifier. As the 5T differential amplifier, which was discussed for the input stage in Chapter 7, offers a compact structure, good gain due to an active load, a good CMRR, a good PSRR and high input impedance, it was used as a starting point of the development procedure.

With a structure capable of taking the difference, the 5T amplifier, a structure which also takes the absolute value of the difference, had to be modified into the structure. When taking a absolute value of a difference of numbers the outcome is always positive. Thereby one arm has to be larger than the other at all times. This arm aswell has to be prepared for both of the inputs. Such an architecture is described in Figure 8.3.

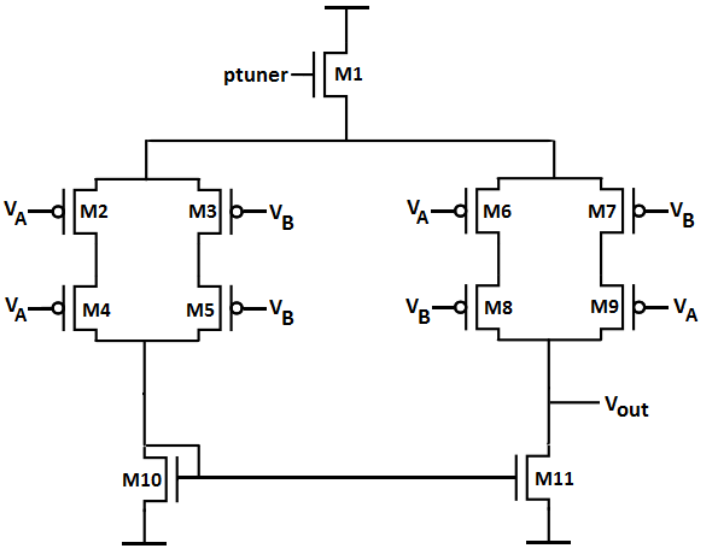

Figure 8.3: PMOS Single Ended Absolute Value Filter Architecture

As there are two inputs, the left arm will always represent a higher or equal value to the right arm. This means that whether V_A or V_B is high or low the right arm will always output the value which will be subtracted from the left arm. Thereby the output will always be positive.

The structure was developed by realizing that whether V_A or V_B had an incoming signal, not both, drain current ran through the left arm but not the right one. On the other hand whether both or none had an incoming signal, the right arm would mirror the left one. Then in order for symmetry of the circuit, double transistors were added on the left side. But symmetry is an advantage as the impedance over both of the arms is the same and the signals are affected in a similar manner through both arms of the circuit. From this, it can be further derived that fewer transistors in this implementation is not feasible.

With further development of the architecture its sensitivity towards variations becomes evident in the performance of the circuit. In the case of variations of the threshold voltage, V_T, of the input PMOS transistors, mismatch would cause a shift in the voltage output. In the architecture, the transistor $M10$ has its gate connected to its drain $V_D = V_G = V_{GS}$. All the transistors are in the subthreshold region where they follow Equation 8.4:

$$V_{GS} \leq V_T \tag{8.4}$$

This means unless V_{out} is smaller or equal to V_T this circuit will not work. Thereby, its sensitivity towards variations cause the output to easily slide to one of the rails. However, by applying a differential output this highly sensitive part of the circuit could be avoided. The differential architecture can be seen in Figure 8.4.

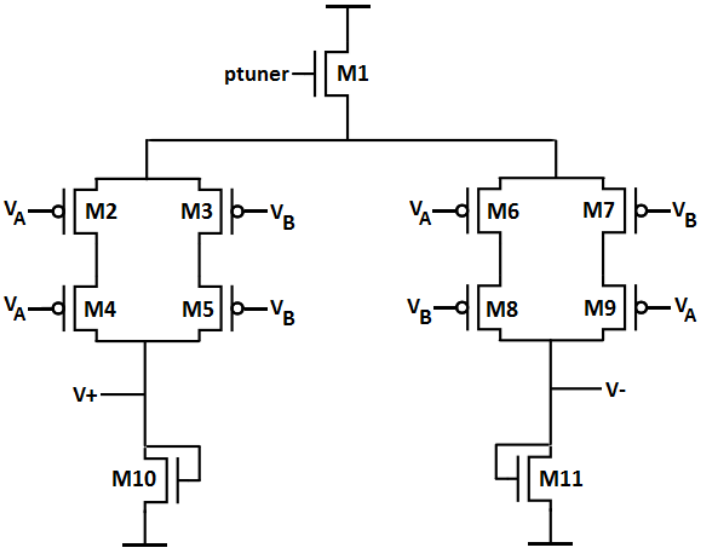

Figure 8.4: Differential Absolute Value Filter Architecture

In addition, a differential NMOS input architecture is compared to the PMOS one, in order to decide which one is more advantageous, see Figure 8.5.

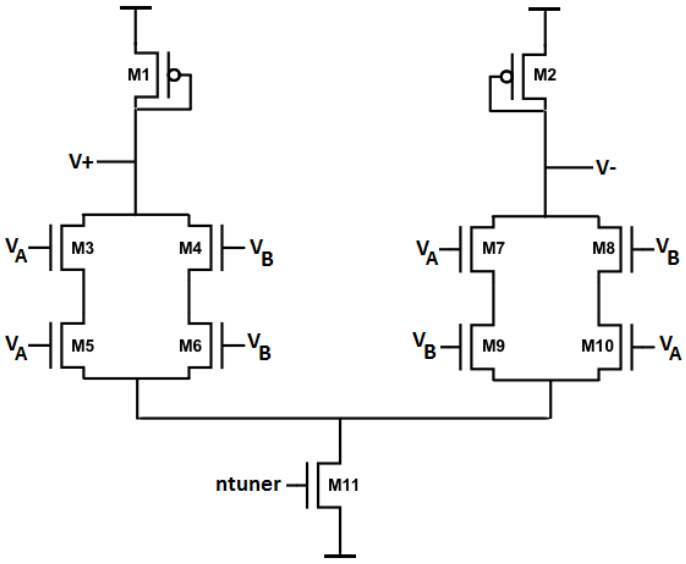

Figure 8.5: NMOS Differential Absolute Value Filter Architecture

The sources of offsets affecting the presented architectures largely originate from:

- Variations of the threshold voltage, V_T, causing mismatch between transistors.
- Variations of the size of the transistors causing a mismatch of the W/L ratio between the transistors.

Variations of the transistor's width, W, and length, L, affects the drive current and the change in threshold voltage can aswell shift the drive current.

Concerning variability, a Monte Carlo analysis was made on the previously mentioned absolute value filter circuits. Monte Carlo simulation analysis is a tool which can be applied to a circuit in order to see how their behavior and performance is under random mismatches in the circuit. The Monte Carlo method uses a statistical analysis which simulates the response of the circuit with transistor parameters which are randomly varied according to a special statistical distribution. With this method a small signal analysis was done to estimate the mean voltage gain and the standard deviation was calculated for each structure, see Table 8.1.

Architecture	**Mean Voltage Gain**	**Standard Deviation**
PMOS Input/Single-ended Output	-63.1 dB	50.0 %
PMOS Input/Differential Output	-27.7 dB	4.5 %
NMOS Input/Differential Output	-13.2 dB	6.8 %

Table 8.1: Absolute Value Filter Architecture Variability Comparison

For these simulations the set sizes of the transistors are kept the same, see Table 8.2.

Transistor	W	L
NMOS	1 μm	1 μm
PMOS	1 μm	1 μm
ntuner	28 μm	3.2 μm
ptuner	28 μm	1.6 μm

Table 8.2: Transistor Sizes of the Architectures

As predicted, the PMOS input transistor architecture with a single-ended output is highly sensitive to mismatch. On the other hand the difference and the preference between the NMOS and the PMOS input transistors with differential outputs are up for discussion. From the variability comparison of the architectures it can be seen that while a PMOS-based input offers a little bit lower resistance to variations, NMOS offers higher gain.

Another pointer to add, as described previously, is that the majority carriers in NMOS are electrons and holes in PMOS. The mobility of electrons (1400 $cm^2/V \cdot s$) is much higher than of holes (450 $cm^2/V \cdot s$) in silicon [119]. For the same speed the NMOS inputs can therefore offer smaller area with smaller capacitors. This can be related to that the size of the capacitors affect the RC time constant (τ) with the following relationship, see Equation 8.5:

$$\tau = \frac{1}{RC} \tag{8.5}$$

Since for our application area and power are of high interest, the NMOS input architecture with a differential output was chosen, see Figure 8.5. The structure is a set of NMOS input transistors and PMOS diode connected resistances. The circuit is biased by an *ntuner* which acts like a current source changing the voltage into current. The *ntuner* controls the current through the circuit. Due to an ultra low power budget of the circuit the current source is kept in the nano Ampere range. The inputs to the circuit are V_A and V_B. The output function is the absolute value of the difference between the two, times the gain that the circuit provides, see Equation 8.6.

$$V_{out} = V_+ - V_- = A \cdot |V_A - V_B| \tag{8.6}$$

where A is the gain of the circuit.

8.3.1 Gain Boost Technique

If the architecture does not provide sufficient gain, a current source can be added into the feedback in order to boost the gain. An example is shown in Figure 8.6.

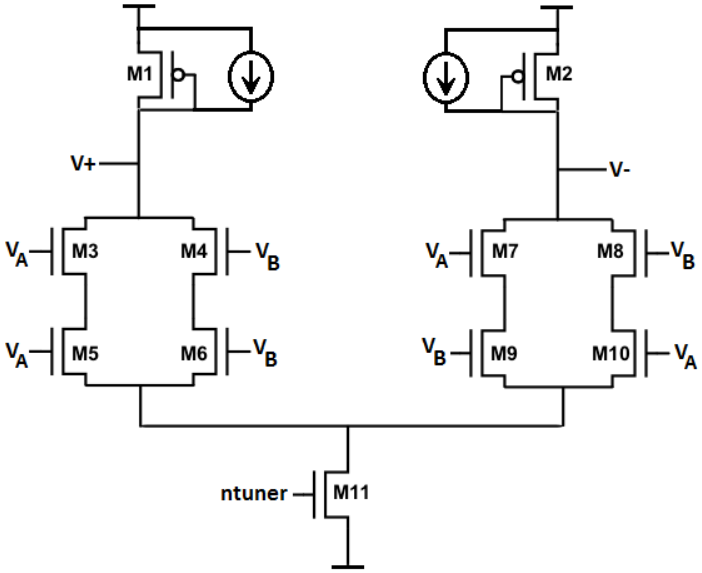

Figure 8.6: NMOS Differential Absolute Value Filter Architecture with Gain Boosting

The added current source distributes the current into two branches, decreasing the current through the diode connected resistor. This results in a decrease in the transconductance, g_m, of the transistor. This can be seen from the following relationship, see Equation 8.7:

$$g_m = \frac{qI_D}{nkT} \tag{8.7}$$

Now as the g_m is decreased, the resistance of diode connected resistor is increased, see Equation 8.8:

$$R = \frac{1}{g_m} \tag{8.8}$$

This proportionally boosts the gain of the circuit causing a higher voltage drop over the load.

8.3.2 Current Mirror Architecture

In order to bias the circuit in the desired operating region a precision biasing circuit needs to be added to the absolute value filter architecture. A common biasing method is by a current mirror. However, this can be and was also used as an active load in the first proposed architecture. A current mirror is able to mirror its current into another device while keeping the output current (I_{out}) constant. A basic current mirror scheme can be seen in Figure 8.7 [a] and [b], with both NMOS and PMOS structure, respectively.

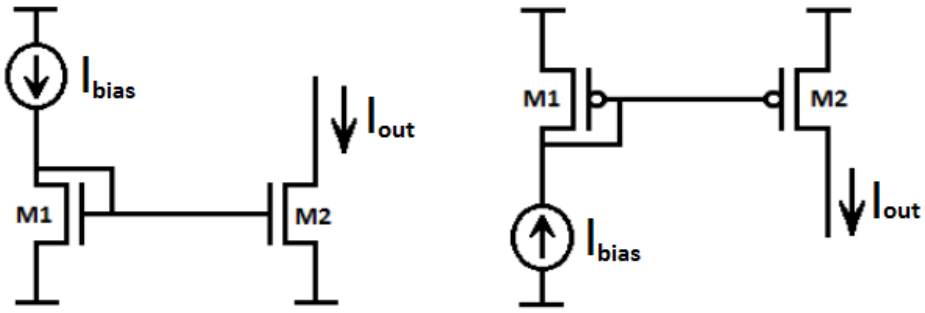

(a) NMOS Current Mirror (b) PMOS Current Mirror

Figure 8.7: Current Mirror Architectures

Both circuits are based on two transistors where the circuits work as follows. A bias current is fed into the transistor, M1, where its gate and source are connected, forcing it into the saturation region. The current is changed into a voltage which is applied at the gate of the second transistor, M2, causing an identical current to flow through the transistor if both the transistors are identical. From a mathematical form, it can better be described as follows. The current through the transistor, M1, without respect to channel-length modulation is, see Equation 8.9:

$$I_{bias} = \frac{1}{2}\mu_n C_{ox}\frac{W_1}{L_1}(V_{GS} - V_{T_1})^2 \tag{8.9}$$

While through the outer transistor, M2, the current is, see Equation 8.10:

$$I_{out} = \frac{1}{2}\mu_n C_{ox}\frac{W_2}{L_2}(V_{GS} - V_{T_2})^2 \tag{8.10}$$

As the gate current is zero and both of the transistors have the same V_{GS}, their relation can be derived as follows, see Equation 8.11:

$$I_{out} = I_{bias} \cdot \frac{W_2/L_2}{W_1/L_1} \tag{8.11}$$

From these results the dependency on identical transistor sizes can be seen. This determines the current mirror vulnerability to mismatch. This behavior can be further explained by the small signal circuit in Figure 8.8.

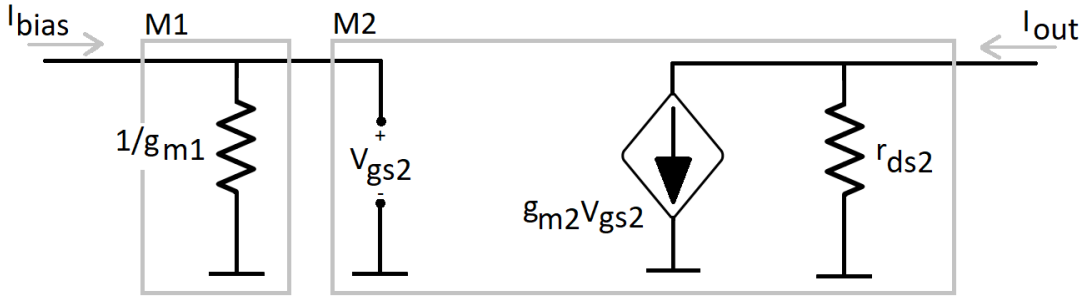

Figure 8.8: Current Mirror Small Signal Model

From this circuit a key parameter, the output resistance, $R_{out} = r_{ds2}$, can be calculated. When the size of the two transistors differ, r_{ds} determines which has a larger current. An ideal current mirror has zero input resistance and a high output resistance. From the small signal model, it can be seen clearly that the current supply is not dependent on the output voltage. If for a desired application, higher output resistance is needed, a cascode transistor with M2 is possible.

8.4 Circuit Analysis and Results

In Chapter 7, the subthreshold region was presented. For circuits which operate in the subthreshold region problems such as lack of controllability, inaccuracy and requirements of numerous voltage and current sources occur [120]. Analysis is highly important to ensure the correct operation of a circuit. Signal analysis such as a large signal analysis, which is used to set up the bias conditions and takes into account the non-linear behavior of the circuit, and a small signal analysis, which assumes a correct bias of the transistors and linear behavior for the small signals, can be applied. The absolute value circuit is highly non-linear, therefore simplifications of the analysis are applied. Due to the non-applicable frequency response, the analysis of the noise is done from different bias points. Also in this thesis the absolute value filter structure gain was not optimized using the gain boost technique and is left for further development if needed.

8.4.1 CMOS Technology

Before continuing the circuit analysis and simulation the CMOS technology of choice is of great importance. The CMOS technology has to be chosen for low power application and has to offer sufficiently small parameters and analog modules, including capacitors and resistors. Different technologies exist but for simplicity, a 180 nm XFAB module (XC018) will be used for both the calculations and the simulations [121]. The technology is of choice as it is compatible with 1.8 V and low power modules.

In Table 8.3 a few parameters needed for the analysis of the absolute value filter are presented. These parameters are retrieved from an XFAB process module.

Table 8.3: 180 nm XFAB Transistor Model Parameters of Interest

	V_T	μ_n	C_{ox}
NMOS	0.56 V	307 cm^2/Vs	8.46 $fF/\mu m^2$
PMOS	-0.7 V	59 cm^2/Vs	8.85 $fF/\mu m^2$

However, further decision of the correct CMOS technology process is to find a process compatible with 1.8 V but also offering high voltage modes. High voltage mode allows for a galvanic isolation and separation between high and low voltage areas on the chip [122]. This would be beneficial in case of different supply voltages towards the network. At the same time, the final decision on a technology process depends on the final neural network structure.

8.4.2 Large Signal Analysis

The first step of the circuit analysis is to secure a correct operation of the circuit. This is done by biasing the circuit. The goal of the circuit is to offer very low power consumption. With a current sweep the final decision was to supply the current mirror of a bias current of 10 nA. The low current biases the circuit into the subthreshold region or weak inversion. The decision was derived by sweeping across a current range. It was concluded that for a lower current the circuit

was fully cutoff and thereby not feasible. Then any higher current showed a worse response which was expected due to the load of the circuit as $1/g_m$.

Figure 8.9 presents points on the circuit used for the large signal or low frequency DC analysis. The points are presented as A, B, same for all NMOS inputs, and C. As the input signals are in the range of couple of *milli Volts* resulting from the environment of the circuit 10 mV is chosen. Due to this low voltage behavior the gate voltage of the NMOS inputs has to be biased in order to detect the signal.

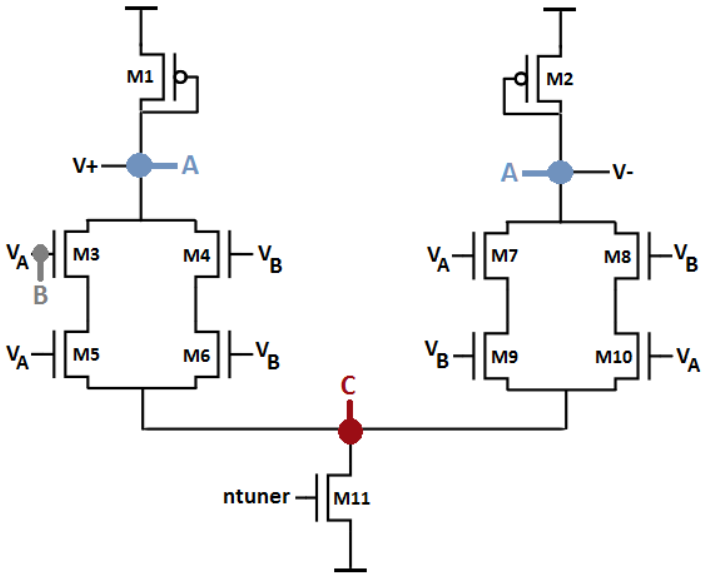

Figure 8.9: NMOS Differential Absolute Value Filter Architecture with DC Points of Interest

The minimum sizes of the transistors in the circuit can be seen in Table 8.4. From the results of the gain in Table 8.1 are done for transistors with four times the sizes shown here below. Thereby the biasing and DC point values do not change as the ratio of W/L is kept the same.

Table 8.4: Transistor Sizes in the Absolute Value Filter

Transistor	**M1 - M10**	**M11**
W/L	0.25μm/0.25μm	7μm/0.8μm

Now, in order to calculate the DC points the following subthreshold drain current equation is presented [123], see Equation 8.12:

$$I_D = I_{D0} \cdot \frac{W}{L} \cdot e^{\frac{V_{GS}}{nV_t}} (1 - e^{\frac{V_{DS}}{V_t}}) \approx I_{D0} \cdot \frac{W}{L} \cdot e^{\frac{V_{GS}}{nV_t}} \tag{8.12}$$

where I_{D0} can be calculated by Equation 7.17. As the current through each of the differential paths is around 5 nA. The gate-source voltage, V_{GS}, which is the voltage drop over the diode connected resistors can be calculated using the derivation, see Equation 8.13:

$$V_{GS} = n \cdot V_t \cdot ln(\frac{I_D}{I_{D0} \cdot \frac{W}{L}}) \tag{8.13}$$

Starting with point A. With $W/L = 0.25\mu\text{m}/0.25\mu\text{m} = 1$, $V_t = \frac{kT}{q} \approx 26$ mV and $n \approx 1.5$ and alongside with the values presented in Section 8.4.1 and Equation 7.17, V_{GS} is calculated as 0.32 V. Thereby, point A can be calculated as follows, see Equation 8.14:

$$V_A = V_{out} = V_{cc} - I_D * R_{out} = V_{cc} - V_{GS} \approx 1.48V \tag{8.14}$$

For a little more accuracy some headroom should be included. Headroom of roughly 100 - 150 mV results in a V_{out} in the range of 1.4 V. By including the headroom and threshold voltage the input bias nodes, point B, were set out to be around 1.1 V.

From Section 8.4.1 and Equation 7.17, V_{GS} is 0.25 V. For point C, can then be estimated as follows, see Equation 8.15:

$$V_C = V_B - I_D * R_{out} = V_B - V_{GS} \approx 0.85V \tag{8.15}$$

Thereby with some headroom, the range for V_C is around 0.7 V. This was confirmed via simulation.

When a low frequency analysis is applied to the circuit, capacitors and inductors inside the circuit are ignored. By simulating the circuit in DC mode, it is possible to see how the circuit depends on other parameters inside the circuit. In Figure 8.10 the DC transfer characteristics can be seen. V_{in} in this case is V_A which is swept from 0 to 1.8 V while V_B is held constant at 1.1 V.

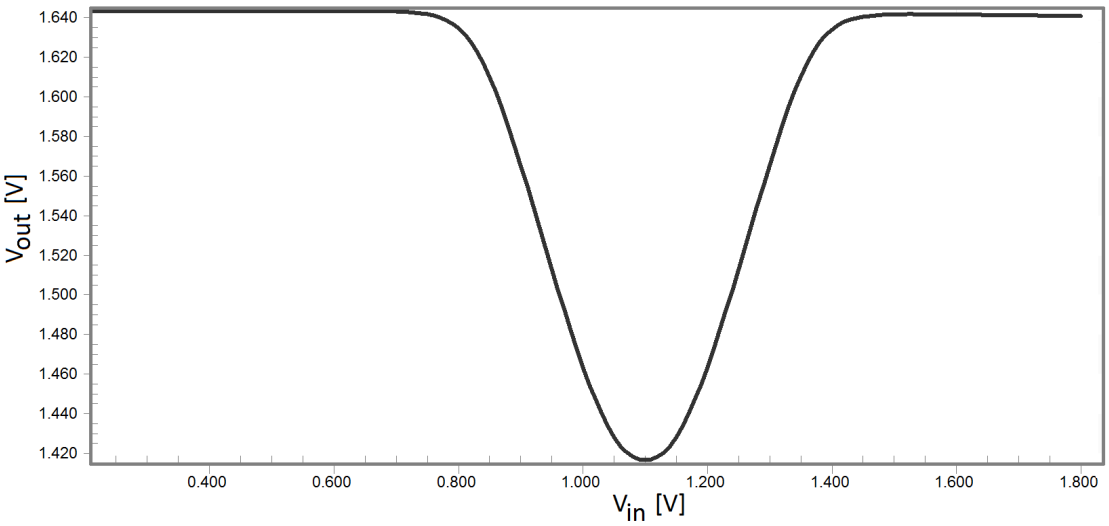

Figure 8.10: Absolute Value Filter DC Transfer Characteristics

From this picture the circuit performance can be estimated. From the range of around 0.8 to 1.4 V the circuit is working.

8.4.3 Small Signal Analysis and Transient Response

Due to the non-linearity of the circuit, the transfer function of the system is highly complex. However, the circuit behavior can be understood from Table 8.5, forcing the response into the digital domain, depending on which rail it is pulled towards.

Table 8.5: Circuit Behavior represented in a Truth Table

V_A	V_B	V_{out}
Low	Low	Low
High	High	Low
Low	High	High
High	Low	High

From this table, the estimated output functions can be derived as follows. For the left arm, see Equation 8.16:

$$V_+ = V_A \cdot g_m + V_B \cdot g_m \tag{8.16}$$

For the right arm, see Equation 8.17:

$$V_- = \overline{V_A} \cdot g_m + \overline{V_B} \cdot g_m \tag{8.17}$$

Finally, its transient response, simulated with square waves, can be seen in Figure 8.11. Again, the input signal is in the order of 10 mV to act as the possible detected input signal.

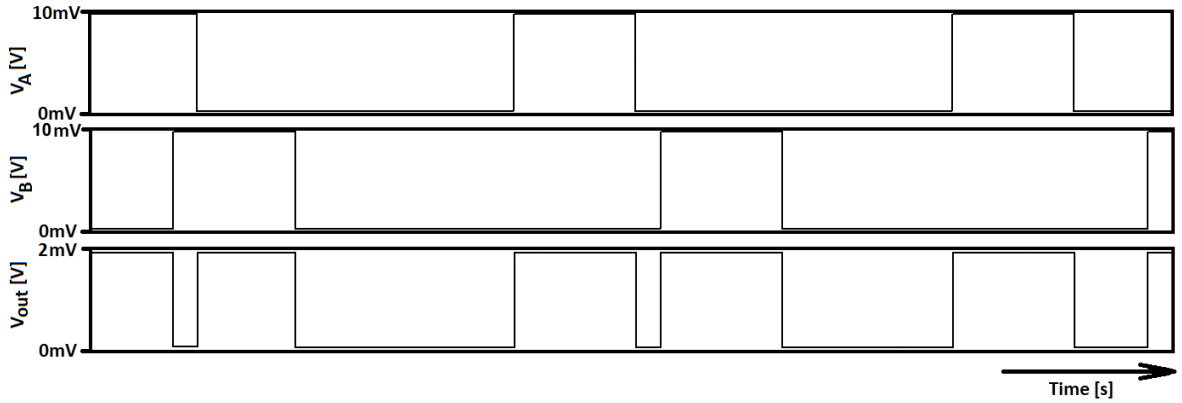

Figure 8.11: Absolute Value Filter Transient Behavior

The circuit is highly attenuated unless when applying the gain boost technique as explained in Section 8.3.1. However, as this structure might only be used for detecting whether an update to a weight is required or no, how much gain is needed is not determined for the time being.

8.4.4 Noise and Power Dissipation

The noise in the subthreshold region consists largely of thermal noise and flicker noise [123]. Thermal noise is randomly excited by charge carriers and can be calculated in the subthreshold region with Equation 8.18:

$$i_n^2 = 2kTng_mB \tag{8.18}$$

where k is the Boltzmann constant, T is the absolute temperature, n is the subthreshold slope, B is the bandwidth and g_m is the transconductance. The transconductance is then determined by the ratio of drain current and the gate-source voltage, i_d/v_{gs}. In weak inversion, it is predicted that the more the current density is reduced, the closer g_m reaches its maximum [123], see Equation 8.19:

$$g_m \propto \frac{I_d}{nV_t} \tag{8.19}$$

Thereby, an increase in current density will lower the thermal noise.

The origin of flicker noise is related to the carrier number fluctuation theory which can be read about in [124]. Equation 8.20 shows the factors influencing the flicker noise power:

$$i_n^2 = \frac{K}{fC_{ox}WL} \tag{8.20}$$

where K is the technology parameter, f is the frequency, C_{ox} is the oxide capacitance, W is the gate width and L is the gate length. Thereby the dependency on certain parameters can be seen. With lower frequency the flicker noise becomes more influential. The parameters, K, f and C_{ox}, are parameters which are more difficult to change. However, sizing W and L of a transistor, clearly improves the flicker noise.

As AC analysis is only valid for LTI (Linear Time-Invariant) systems a way to estimate the noise for this non-linear circuit is by selecting few points on the large signal transition curve or the DC transfer characteristic graph, see Figure 8.10. From there an AC analysis is done with a noise analysis in those points.

In Table 8.6 the noise is simulated from two different bias points, where V_A is firstly 1.05 V and secondly 1.0 V and V_B is constant at 1.1 V for both. This results in four uncorrelated noise sources, from each input to each output. The total input referred noise, v_{ntot}, for the circuit, with four sources, is then calculated by, see Equation 8.21:

$$v_{ntot}^2 = v_{1n}^2 + v_{2n}^2 + v_{3n}^2 + v_{4n}^2 \tag{8.21}$$

Each noise source is referenced from the input to the output it is measured from. Thereby v_{1n}^2 is the noise from V_A to $V+$, v_{2n}^2 is V_A to $V-$, v_{3n}^2 is V_B to $V+$ and v_{4n}^2 is V_B to $V-$. For the simulation the noise was simulated from 100 Hz to 1 MHz and the total input referred noise is presented for each point in Table 8.6.

Table 8.6: Noise Analysis at Different Bias Points

Bias Points	v_{1n}^2	v_{2n}^2	v_{3n}^2	v_{4n}^2	v_{ntot}
$V_A = 1.0$ V, $V_B = 1.1$ V	984 μV	322 μV	625 μV	339 μV	1256 μV
$V_A = 1.05$ V, $V_B = 1.1$ V	614 μV	397 μV	495 μV	446 μV	988 μV

The original sizes of the filter, shown in Table 8.4, were sized up by four for this simulation. But with increasing the sizes of the transistor, the flicker noise can be decreased. However, this is not the case with the thermal noise. The sizing of the transistor does not affect the thermal noise as the ratio of W and L is kept constant in this case. By decreasing the length however, the current density can be increased and the thermal noise decreased. Nevertheless, this might influence the signal power. In Figure 8.12 the effects from the transistor sizing on the noise are shown. For the flicker noise both W and L are sized up by a constant C but for the thermal noise only L is sized by a constant C.

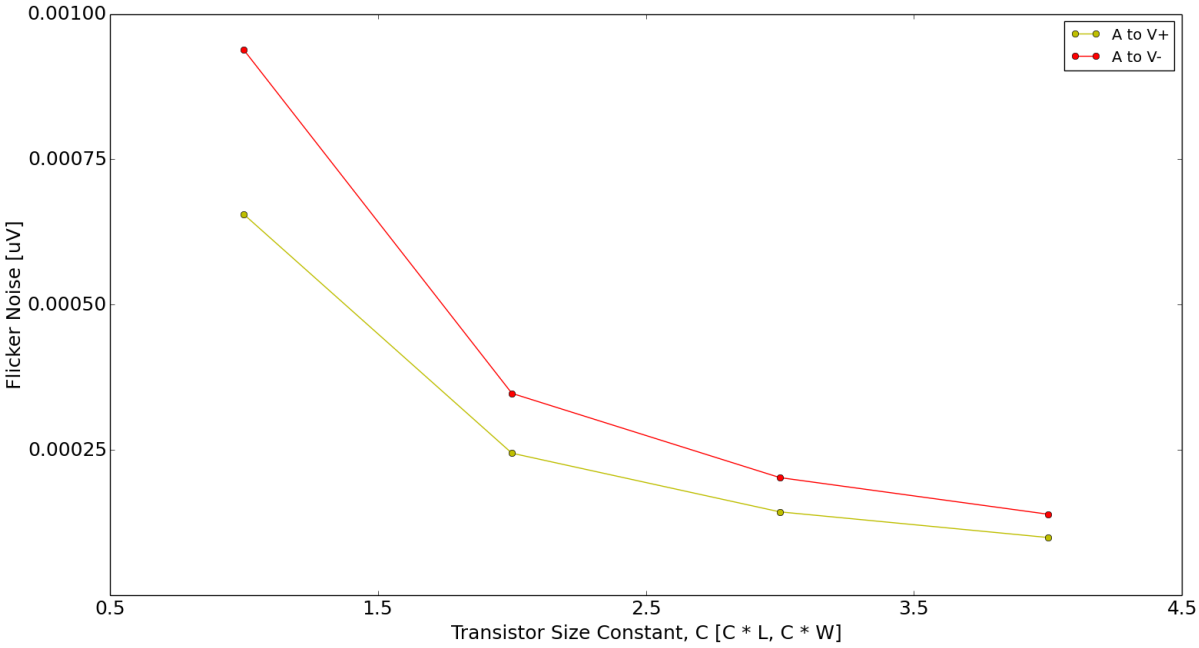

(a) Flicker Noise Dependency on Transistor Sizing

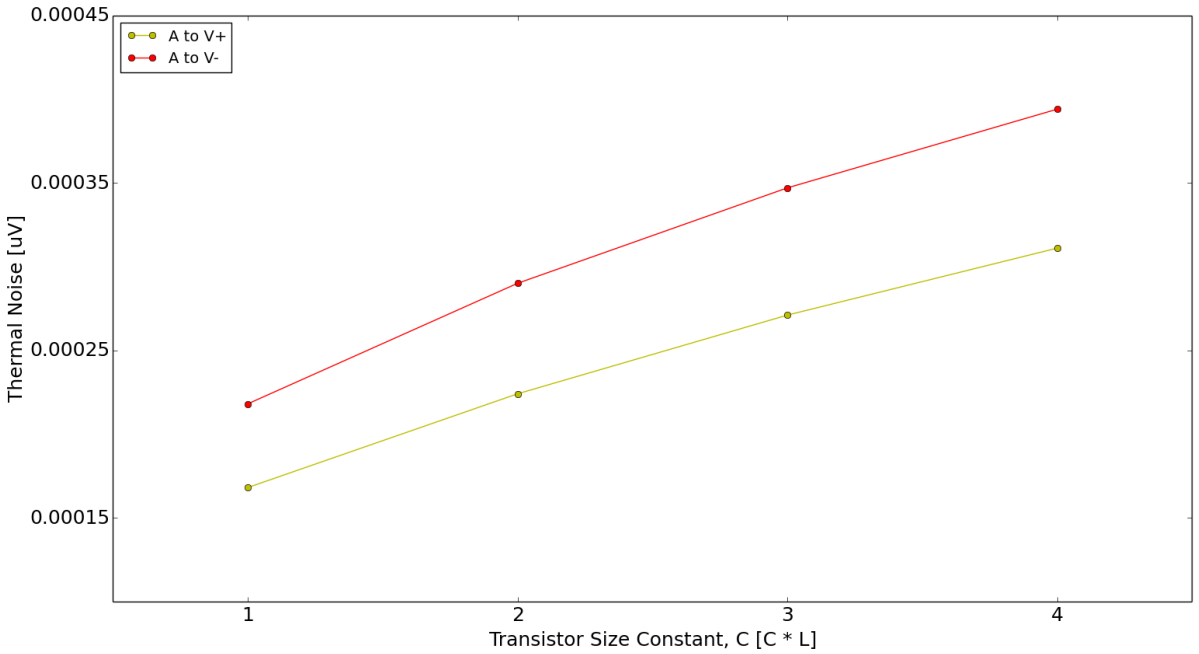

(b) Thermal Noise Dependency on Transistor Sizing

Figure 8.12: Subthreshold Noise Optimizations on Flicker and Thermal Noise

Figure 8.12 [a] shows how the flicker noise decreases when the transistors are sized up. This was expected from Equation 8.20. Figure 8.12 [b] shows how the thermal noise increases as the ratio of W/L becomes smaller. This was a behavior derived from Equations 8.18, 8.19 and 8.12.

Finally, the power can be easily estimated by using Equation 8.22:

$$P = V_{supply} \cdot I = 1.8V \cdot 10nA = 18nW \tag{8.22}$$

The power estimation of the circuit is very low due to the low rail supply and tail current. When simulated, the total power consumption is 87nW. The difference can be traced back to variations in and sizing of the transistors, to the noise and the accuracy of the simulator in weak inversion.

8.4.5 Future Work

Overall improvements on the circuit involve optimizing the gain and realizing an absolute value filter circuit without the attenuation. All this has to be carefully laid out with tradeoff in mind while focusing on low power and small area.

Also, the noise specifications were not fully optimized and therefore remain high. Possible improvement methods were shown as how the transistor size affects noise power. In Figure 8.12 the influence from input A to output $V+$ and $V-$ on the flicker and the thermal noise with transistor sizing was shown. Full optimization of the noise specifications remains for future work. The proposed architecture in this thesis will not necessarily be the definitive architecture for the neural network. The decision depends on if the noise levels are acceptable and comply with the set requirements, alongside other modules within the project. Ultimately, this decision is made by Caeleste further along in the design process, which is outside the scope of this thesis.

Bibliography

[1] CEI-Europe Advanced Learning for Professionals, "CCD vs CMOS Infographic," [Online]. Available: http://www.cei.se/news/9651/CCD-vs-CMOS-Infographic.aspx, 2016, Accessed: April 2017.

[2] S. R. Morrison, "A New Type of Photosensitive Junction Device," *Solid-State Electronics*, vol. 6, pp. 485–494, 1963.

[3] A. H. Titus, M. C. K. Cheung, and V. P. Chodavarapu, "CMOS Photodetectors," in *Photodiodes - World Actvities in 2011*, J.-W. Park, Ed. Rijeka: InTech, 2011, ch. 04.

[4] J. Nakamura, *Image Sensors and Signal Processing for Digital Still Cameras*. Taylor and Francis Group, LLC, 2006, pp. 27-30, 54-87, 147-160.

[5] Optoelectronics: An OSI Systems Company, "Photodiode Characteristics and Applications," [Online]. Available: http://www.osioptoelectronics.com/application-notes/an-photodiode-parameters-characteristics.pdf, 2013, Accessed: April 2017.

[6] E. Fossum and D. Hondongwa, "A Review of the Pinned Photodiode for CCD and CMOS Image Sensors," *IEEE Journal of the Electron Devices Society*, vol. 2, no. 3, pp. 33–43, 2014.

[7] T. York, "Fundamentals of image sensor performance," [Online]. Available: http://www.cse.wustl.edu/~jain/cse567-11/ftp/imgsens/index.html, 2011, Accessed: April 2017.

[8] G. P. Weckler, "Operation of p-n Junction Photodetectors in a Photon Flux Integrating Mode," *IEEE Journal of Solid-State Circuits*, vol. 2, no. 3, pp. 65–73, 1967.

[9] P. J. W. Noble, "Self-Scanned Silicon Image Detector Arrays," *IEEE Transactions on Electron Devices*, vol. 15, no. 4, pp. 202–209, 1968.

[10] N. Teranishi, "The Pinned Photodiode," [Online]. Available: https://indico.cern.ch/event/522485/contributions/2174996/attachments/1282603/1906227/2016_5FEE_teranishi_ver5.pdf, 2016, Accessed: April 2017, University of Hyogo Shizuoka.

[11] K. A. Campbell, "Charge transfer inefficiency in pinned photodiode cmos image sensors: Simple montecarlo modeling and experimental measurement based on a pulsed storage-gate method." *Solid-State Electronics*, vol. 125, pp. 227–233, November 2016.

[12] S. K. Mendis, S. E. Kemeny, R. C. Gee, B. Pain, C. O. Staller, Q. Kim, and E. R. Fossum, "CMOS Active Pixel Image Sensors for Highly Integrated Imaging Systems," *IEEE Journal of Solid-State Circuits*, vol. 32, no. 2, pp. 187–197, 1997.

[13] FLIR Integrated Imaging Solutions, "Key differences between rolling shutter and frame (global) shutter," [Online]. Available: https://www.ptgrey.com/KB/10028, 2015, Accessed: May 2017.

[14] Swept Image, Inc, "Rolling down the cost of 3d confocal microscopy," http://www.ptgrey.com/case-study/id/10878, Accessed: October 2017.

[15] T. Fellers and M. Davidson, "Concepts in digital imaging technology: Digital camera readout and frame rates," [Online]. Available: http://hamamatsu.magnet.fsu.edu/articles/readoutandframerates.html, Accessed: April 2017.

[16] R. F. Cannata, R. J. Hansen, A. N. Costello, and W. J. Parrish, "Very Wide Dynamic Range SWIR Sensors for Very Low Background Applications," pp. 756–765, 1999.

[17] A. E. Gamal, "High Dynamic Range Image Sensors," [Online]. Available: http://cafe.stanford.edu/~abbas/group/papers_and_pub/isscc02_tutorial.pdf, 2002, Accessed: April 2017, Stanford University.

[18] A. Wilson, "CMOS Imagers look to increase dynamic range," [Online]. Available: http://www.vision-systems.com/articles/print/volume-19/issue-9/features/cmos-imagers-look-to-increase-dynamic-range.html, 2014, Accessed: May 2017.

[19] Z. Chi, Y. Suying, and X. Jiangtao, "Noise in a CMOS digital pixel sensor," *Journal of Semiconductors*, vol. 32, no. 11, p. 115005, November 2011.

[20] N. Weste and D. Harris, *CMOS VLSI Design: A Circuits and Systems Perspective*. Pearson Education, Inc, 2011, pp. 241-277.

[21] D. Huang, E. A. Swanson, C. P. Lin, J. S. Schuman, W. G. Stinson, W. Chang, M. R. Hee, T. Flotte, K. Gregory, C. A. Puliafito, and J. G. Fujimoto, "Optical coherence tomography," *Science*, vol. 5035, no. 254, p. 1178–1181, 1991.

[22] J.Zhang, Y.Chen, and L.Luo, "Improved nonlocal means for low-dose x-ray ct image," in *3rd International Conference on Information Science and Control Engineering*, 2016, pp. 410–413.

[23] L. V. Wang and H. Wu, *Biomedical Optics: Principles and Imaging*. John Wiley & Sons, Inc, 2007, pp. 1-2.

[24] Y. Tan and H. Jiang, "Diffuse optical tomography guided quantitative fluorescence molecular tomography," *Applied Optics*, vol. 47, no. 12, pp. 2011–2016, 2008.

[25] N. R. Center, "Computed tomography," https://www.nde-ed.org/EducationResources/CommunityCollege/Radiography/AdvancedTechniques/computedtomography.htm, Accessed: May 2017.

[26] J. Kim, "Biomedical imaging applications of parallel optical coherence tomography and adaptive optics," Ph.D. dissertation, The University of Texas, 2004, pp. 11-12.

[27] P. Education, "Spectral irradiance," http://www.pveducation.org/pvcdrom/properties-of-sunlight/spectral-irradiance, Accessed: May 2017.

[28] N. K. Keppy and M. Allen, *Understanding Spectral Bandwidth and Resolution in the Regulated Laboratory*, Thermo Fisher Scientific Inc., 2008, pp. 1-3.

[29] H. Jelinková, *Lasers for Medical Applications: Diagnostics, Therapy and Surgery*. Woodhead Publishing, 2013, pp. 4-9.

[30] E. M. C. Hillman, "Experimental and theoretical investigations of near infrared tomographic imaging methods and clinical applications," Ph.D. dissertation, University College London, 2002, pp. 11-33.

[31] J. T. Hashmi, Y.-Y. Huang, S. K. Sharma, D. B. Kurup, L. D. Taboada, J. D. Carroll, and M. R. Hamblin, "Effect of pulsing in low-level light therapy," *Lasers Surg Med*, vol. 42, no. 6, p. 450–466, August 2010.

[32] B. Horecker, "The absorption spectra of hemoglobin and its derivatives in the visible and the near infra-red regions," *J. Biol. Chem*, pp. 173–183, 1943.

[33] H. Jiang, *Diffuse Optical Tomography: Principles and applications*. CRC Press, 2010, pp. 219-304.

[34] E. Figueiras, A. M. Soto, D. Jesus, M. Lehti, J. Koivisto, J. E. Parraga, J. Silva-Correia, J. M. Oliveira, R. L. Reis, M. Kellomäki, and J. Hyttinen, "Optical projection tomography as a tool for 3d imaging of hydrogels," *Biomed Opt Express*, vol. 5, no. 10, p. 3443–3449, Oct 2014.

[35] W. Zou and X. Pan, "Compressed-sensing-based fluorescence molecular tomographic image reconstruction with grouped sources," *Biomed Eng Online*, vol. 13, no. 119, pp. 1–15, Aug 2014.

[36] V. Ntziachristos, "Fluorescence molecular imaging," *Annu Rev Biomed Eng.*, vol. 8, pp. 1–33, 2006.

[37] B. Judkewitz, "Light and tissue 1," http://www.its.caltech.edu/~bi177/private/L6_handout.pdf, Accessed: May 2017.

[38] S. L. Jacques, "Optical properties of biological tissues: a review," *Phys. Med. Biol.*, vol. 58, pp. R37–R61, 2013.

[39] V. Ntziachristos, "Going deeper than microscopy: the optical imaging frontier in biology," *Nature Methods*, vol. 7, p. 603–614, July 2010.

[40] L. Hode, "Penetration of light into living tissue," www.laser.nu/lllt/pdf/Penetration.pdf, Accessed: May 2017.

[41] A. J. P. Theuwissen and P. Seitz, *Single-Photon Imaging*. Springer, pp. 334-335.

[42] T. Xie, D. Mukai, S. Guo, M. Brenner, and Z. Chen, "Fiber-optic-bundle-based optical coherence tomography," *Opt. Lett.*, vol. 30, no. 14, pp. 1803–1805, Jul 2005.

[43] "Clinical applications of fiber-optic probes in optical coherence tomography," *Optical Fiber Technology*, vol. 16, no. 6, pp. 467 – 475, 2010, Special Fiber Structures and their Applications.

[44] Teledyne DALSA, "CCD vs. CMOS Which is Better? It's Complicated." [Online]. Available: http://www.teledynedalsa.com/imaging/knowledge-center/appnotes/ccd-vs-cmos/, Accessed: April 2017.

[45] T. Poschinger, "Non-contact optical fluoresence tomography for small animal imaging: System development and multispectral applications," Ph.D. dissertation, Medizinischen Fakultat der Friedrich-Alexander-Universitat, 2010, pp. 34.

[46] L. Hervé, A. D. Silva, J. Boutet, A. Frassati, J.-M. Dinten, P. Peltié, and P. Rizo, "Non contact fluorescence optical tomography by means of numerical and analytical approaches," *Nuclear Instruments and Methods in Physics Research Section A: Accelerators, Spectrometers, Detectors and Associated Equipment*, vol. 571, no. 1, pp. 203 – 206, 2007, proceedings of the 1st International Conference on Molecular Imaging Technology.

[47] J. A. Guggenheim, H. R. A. Basevi, J. Frampton, I. B. Styles, and H. Dehghani, "Multi-modal molecular diffuse optical tomography system for small animal imaging," *Meas Sci Technol.*, vol. 24, no. 10, pp. 1–48, 2013.

[48] C. Honsberg and S. Bowden, "Electroluminescence," http://www.pveducation.org/pvcdrom/characterisation/electroluminescence, Accessed: May 2017.

[49] M. Ali and R. Parlapalli, *Algorithms for Optical Coherence Tomography on TMS320C64x+*, Texas instruments, 2010, pp. 1-16.

[50] W. Xu, D. L. Mathine, and J. K. Barton, "Analog cmos design for optical coherence tomography signal detection and processing," *IEEE Transactions on Biomedical Engineering*, vol. 55, no. 2, pp. 485–489, February 2008.

[51] S. Anlage, "The Michelson Interferometer," http://www.physics.umd.edu/courses/Phys375/AnlageFall06/Lab4Michelson.pdf, 2006, Accessed: June 2017.

[52] M. Ali and R. Parlapalli, *Signal Processing Overview of Optical Coherence Tomography Systems for Medical Imaging*, Texas instruments, 2010, pp. 1-22.

[53] E. N. Glytsis, "Spatial and temporal coherence," http://users.ntua.gr/eglytsis/OptEng/Coherence_p.pdf, 2017, Accessed: June 2017, school of Electrical and Computer Engineering National Technical University of Athens.

[54] RF Cafe, "Temporal and spatial coherence," http://www.rfcafe.com/references/electronics-world/images/lasers-electronics-world-august-1965-2.jpg, Accessed: October 2017.

[55] W. Drexler and J. G. Fujimoto, *Optical Coherence Tomography Technology and Applications*. Springer-Verlag Berlin Heidelberg, 2008, pp. 23, 31-35, 40-50, 61-71, 151-152, 430-450, 565-588.

[56] Z. Yaqoob, J. Wu, and C. Yang, "Spectral domain optical coherence tomography: a better oct imaging strategy," *BioTechniques*, vol. 39, pp. S6–S13, December 2005.

[57] G. Meynants, X. Wu, S. V. hoogenbemt, T. D. Ridder, P. D. Wit, K. Ruythooren, and K. V. Esbroeck, "700 frames/s 2 mpixel global shutter image sensor with 2 me- full well charge and 12 m pixel pitch," in *2015 International Image Sensor Workshop*, pp. 1–4.

[58] R. Kariya, D. L. Mathine, and J. K. Barton, "Analog cmos circuit design and characterization for optical coherence tomography signal processing," *IEEE Transactions on Biomedical Engineering*, vol. 51, no. 12, pp. 2160–2163, 2004.

[59] T. Xie, D. Mukai, S. Guo, M. Brenner, and Z. Chen, "Fiber-optic-bundle-based optical coherence tomography," *Optics Letters*, vol. 30, no. 14, pp. 1803–1805, 2005.

[60] L. Microsystems, "Leica DFC425 / DFC425 C," https://www.leica-microsystems.com/fileadmin/downloads/Leica%20DFC425/Brochures/Leica_DFC425_DFC425C_Brochure_EN.pdf, Accessed: July 2017.

[61] E. Beaurepaire, A. C. Boccara, M. Lebec, L. Blanchot, and H. Saint-Jalmes, "Full-field optical coherence microscopy," *Optics Letters*, vol. 23, no. 4, pp. 244–246, 1998.

[62] S. Bourquin and P. Seitz, "Optical coherence topography based on a two-dimensional smart detector array," *Optics Letters*, vol. 26, no. 8, pp. 512–514, 2001.

[63] P. S. S. Bourquin and R. Salathé, "Two-dimensional smart detector array for interferometric applications," *Electronics Letters*, vol. 37, no. 15, pp. 975–976, 2001.

[64] V. M. S. Bourquin and P. Seitz, "Video-rate optical low-coherence reflectometry based on a linear smart detector array," *Optics Letters*, vol. 25, no. 2, pp. 102–104, 2000.

[65] AKATech S.A., "Intelligent machine vision system," http://optimacorp.co.jp/AKATech/iMVS1XX.htm, Accessed: July 2017, accessed: May 2017.

[66] P. Egan, F. Lakestani, M. P. Whelan, and M. J. Connelly, "Full-field optical coherence tomography with a complimentary metal-oxide semiconductor digital signal processor camera," *Optical Engineering*, vol. 45, no. 1, pp. 1–6, January 2006.

[67] B. Dierickx, D. Scheffer, G. Meynants, W. Ogiers, and J. Vlummens, "Random addressable active pixel image sensors," in *Advanced Focal Plane Arrays and Electronic Cameras*, ser. Proc. SPIE, vol. 2950, December 1996, pp. 2–7.

[68] N. Ricquier and B. Dierickx, "Pixel structure with logarithmic response for intelligent and flexible imager architectures," *Microelectronic Engineering*, vol. 19, pp. 631–634, 1992.

[69] Adimec, "CAReIOCA project results in several new products including CMOSIS CSI2100, Adimec Q-2A750, and LLTech FFOCT microscope and endoscope," http://info.adimec.com/, 2015, Accessed: August 2017.

[70] A. Dubois and A. C. Boccara, "Full-field optical coherence tomography," in *Biological and Medical Physics, Biomedical Engineering Optical Coherence Tomography Technology and Applications*. Springer, 2008, pp. 565–591.

[71] D. Siganos, "Why neural networks?" https://www.doc.ic.ac.uk/~nd/surprise_96/journal/vol1/ds12/article1.html, Accessed: September 2017.

[72] M. Forssell, "Hardware implementation of artificial neural networks," *Information Flow in Networks*, vol. 18, no. 859E, pp. 1–4, 2014.

[73] L. Mastin, "Neurons and synapses," http://www.human-memory.net/brain_neurons.html, 2010, Accessed: August 2017.

[74] T. Sangeetha and C. Meenal, "Digital implementation of artificial neural network for function approximation and pressure control applications," *IOSR Journal of Electronics and Communication Engineering*, vol. 5, no. 2278-8735, pp. 34–39, 2013.

[75] V. G. Maltarollo, K. M. Honório, and A. B. F. da Silva, "Applications of artificial neural networks in chemical problems," in *Artificial Neural Networks - Architectures and Applications*, K. Suzuki, Ed. Rijeka: InTech, 2013, ch. 10. [Online]. Available: http://dx.doi.org/10.5772/51275

[76] L. Chua, "Memristor - the missing circuit element," *IEEE Transactions on Circuit Theory*, vol. 18, no. 5, pp. 507–519, 1971.

[77] S. Williams, "How we found the missing memristor the memristor—the functional equivalent of a synapse—could revolutionize circuit design," http://spectrum.ieee.org/semiconductors/processors/how-we-found-the-missing-memristor, 2008, Accessed: August 2017.

[78] J. Fildes, "Getting more from moore's law," http://news.bbc.co.uk/1/hi/technology/7080772.stm, 2007, Accessed: August 2017.

[79] F. Alibart, S. Pleutin, D. Guerin, C. Novembre, S. Lenfant, K. Lmimouni, C. Gamrat, and D. Vuillaume, "An organic nanoparticle transistor behaving as a biological spiking synapse," vol. 20, pp. 330–337, January 2010.

[80] F. Alibart, S. Pleutin, O. Bichler, C. Gamrat, T. Serrano-Gotarredona, B. Linares-Barranco, and D. Vuillaume, "A memristive nanoparticle/organic hybrid synapstor for neuroinspired computing," vol. 22, pp. 609–616, February 2012.

[81] A. A. Bessonov, M. N. Kirikova, D. I. Petukhov, M. Allen, T. Ryhänen, and M. J. A. Bailey, "Layered memristive and memcapacitive switches for printable electronics," *Nature Materials*, vol. 14, p. 199–204, 2015.

[82] K. A. Campbell, "Self-directed channel memristor for high temperature operation," *Microelectronics Journal*, vol. 59, pp. 10–14, 2017.

[83] C. Mellor, "HP 100TB Memristor drives by 2018 – if you're lucky, admits tech titan," http://www.theregister.co.uk/2013/11/01/hp_memristor_2018/, 2013, Accessed: April 2017.

[84] R. Rojas, *Neural Networks: A Systematic Introduction*. Springer, 1996, pp. 451-476.

[85] C. Yang, H. Kim, S. P. Adhikari, and L. O. Chua, "A circuit-based neural network with hybrid learning of backpropagation and random weight change algorithms," *Sensors*, vol. 17, pp. 1–18, 2017.

[86] K. Hirotsu and M. A. Brooke, "An analog neural network chip with random weight change learning algorithm," in *Proceedings of 1993 International Joint Conference on Neural Networks (IJCNN)*, 1993, pp. 3031–3034.

[87] National Institute on deafness and other communication disorders (NIDCD), "How do we hear?" https://www.nidcd.nih.gov/health/how-do-we-hear, 2014, Accessed: August 2017.

[88] ——, "Cochlear implants," https://www.nidcd.nih.gov/health/cochlear-implants, accessed: August 2017.

[89] T. Goehringa, F. Bolner, J. Monaghana, B. van Dijk, A. Zarowski, and S. Bleeck, "Speech enhancement based on neural networks improves speech intelligibility in noise for cochlear implant users," *Hearing Research*, vol. 344, pp. 183–194, 2017.

[90] M. F. Tenorio, "Using neural networks to improve cochlear implant speech perception," *American Institute of Physics*, pp. 783–793, 1988.

[91] L. Hardesty, "Cochlear implants — with no exterior hardware," http://news.mit.edu/2014/cochlear-implants-with-no-exterior-hardware-0209, 2014, Accessed: August 2017.

[92] R. Kumar and S. Meher, "A novel method for visually impaired using object recognition," in *International Conference on Communications and Signal Processing (ICCSP)*, 2015, pp. 0772–0776.

[93] M. R. Everingham, B. T. Thomas, and T. Troscianko, "Head-mounted mobility aid for low vision using scene classification techniques," *The International Journal of Virtual Reality*, vol. 3, no. 4, pp. 1–11, 1999.

[94] Eyra Ltd, "Horus," https://horus.tech/?l=en_us, Accessed: September 2017.

[95] BBC News, "Arm to provide chips for brain injury implants," http://www.bbc.com/news/technology-39934506, May 2017, Accessed: September 2017.

[96] S. K. Moore, "The vagus nerve: A back door for brain hacking," http://spectrum.ieee.org/biomedical/devices/the-vagus-nerve-a-back-door-for-brain-hacking, 2015, Accessed: September 2017.

[97] A. Wang, A. P. Chandrakasan, and B. H. Calhoun, *Sub-Threshold Design for Ultra Low-Power Systems*. Springer, 2006, pp. 7-9.

[98] M. in Comunicacoes, "How an n-channel mosfet works," http://macao.communications.museum/eng/exhibition/secondfloor/MoreInfo/2_10_4_HowFETWorks.html, Accessed: September 2017.

[99] C. Fonstad, "Mosfets in the sub-threshold region (i.e. a bit below v_t)," https://ocw.mit.edu/courses/electrical-engineering-and-computer-science/6-012-microelectronic-devices-and-circuits-fall-2009/lecture-notes/MIT6_012F09_lec12_sub.pdf, 2009.

[100] F. Schwierz, J. Pezoldt, and R. Granzner, "Two-dimensional materials and their prospects in transistor electronics," *Nanoscale*, vol. 7, pp. 8261–8283, 2015.

[101] S. M. Sze, *Semiconductor Devices Physics and Technology*. John Wiley & Sons, Inc, 2002, pp. 187-207.

[102] A. Doolittle, "Diffusion and drift," http://alan.ece.gatech.edu/ECE3080/Lectures/ECE3080-L-7-Drift%20-%20Diffusion%20Chap%203%20Pierret.pdf, Accessed: September 2017.

[103] K. G. Nichols and E. V. Vernon, *Transistor Physics*. Springer, 1966, pp. 121-129.

[104] M. Lundstrom and J. Guo, *Nanoscale Transistors: Device Physics, Modeling and Simulation*. Springer, 2006, pp. 126-130.

[105] P. R. Gray and R. Meyer, *Analysis and Design of Analog Integrated Circuits*, pp. 65-70.

[106] Caeleste, "Internal documentation."

[107] D. Tsai, E. John, T. Chari, R. Yuste, and K. Shepard, "High-channel-count, high-density microelectrode array for closed-loop investigation of neuronal networks," in *Proc. Annu. Int. Conf. IEEE Eng. Med. Biol. Soc.*, 2015, pp. 7510–7513.

[108] P. E. Allen, "Chapter 4 - CMOS Subcircuits," http://www.aicdesign.org/scnotes/2004notes/chap04_2up_6_29_04_.pdf, 2004, Accessed: August 2017.

[109] M. Kawaguchi, T. Jimbo, and N. Ishii, "Analog learning neural network using multiple and sample hold circuit," in *IEEE/ACIS 11th International Conference on Computer and Information Science (ICIS)*, 2012, pp. 243–246.

[110] K. Lacanette, *LM833,LMF100,MF10 Application Note 779: A Basic Introduction to Filters Active Passive and Switched-Capacitor*, National Semiconductor, April 1991, pp. 1-22.

[111] M. Köksal and S. Herdem, "Analysis of nonlinear circuits by using differential taylor transform," *Computers Electrical Engineering*, vol. 28, no. 6, pp. 513–525, 2002.

[112] W. D. White, "Nonlinear filters," *Transactions of the IRE Professional Group on Circuit Theory*, vol. CT-1, no. 4, pp. 2–5, 1954.

[113] J. O. Smith, *Introduction to Digital Filters with Audio Applications*. https://ccrma.stanford.edu/~jos/fp/Analysis_Nonlinear_Filters.html, Accessed: September 2017.

[114] Z. Wang, "Full-Wave Precision Rectification that is Performed in Current Domain and Very Suitable for CMOS Implementation," *IEEE Transactions on Circuits and Systems I: Fundamental Theory and Applications*, vol. 39, no. 6, pp. 456 – 462, 1992.

[115] C. Keate, "High-speed analog multiplier–absolute value detector," May 23 1989, US Patent 4,833,639. [Online]. Available: https://www.google.com/patents/US4833639

[116] B. Abdi, "Voltage to absolute value current converter," Mar. 6 1990, US Patent 4,906,915. [Online]. Available: https://www.google.com/patents/US4906915

[117] A. G. Andreou and K. A. Boahen, "Translinear circuits in subthreshold mos," *Analog Integrated Circuits and Signal Processing*, vol. 9, no. 2, p. 141–166, 1996.

[118] A. A. Ciubotaru, "Absolute-value circuit using junction field-effect transistors," *IEEE Transactions on Circuits and Systems II: Analog and Digital Signal Processing*, vol. 50, no. 8, pp. 481–484, 2003.

[119] Ioffe Institute, "Electrical properties of silicon (si)," http://www.ioffe.ru/SVA/NSM/Semicond/Si/electric.html, Accessed: September 2017.

[120] J. P. Chamorro, C. Lahuec, F. Seguin, and M. Jezequel, "Design Rules for Subthreshold MOS Circuits," 2004, Accessed: September 2017.

[121] X. M. S. F. Experts, "Xc018: 0.18 micron modular rf enabled cmos technology," https://www.xfab.com/fileadmin/X-FAB/Download_Center/Technology/Datasheet/XC018_Datasheet.pdf, 2017, Accessed: November 2017.

[122] XFAB Mixed-Signal Foundry Experts, "SOI Process Technologies," https://www.xfab.com/technology/soi/, Accessed: September 2017.

[123] M. H. Perrott, "Analysis and design of analog integrated circuits lecture 16 subthreshold operation and gm/id design," http://www.cppsim.com/CircuitLectures/Lecture16.pdf, 2012, Accessed: September 2017.

[124] A. Arnaud and C. Galup-Montoro, "Consistent noise models for analysis and design of cmos circuits," *IEEE Transactions on Circuits and Systems I: Regular Papers*, vol. 51, no. 10, pp. 1909–1915, 2004.